



저작자표시-비영리-변경금지 2.0 대한민국

이용자는 아래의 조건을 따르는 경우에 한하여 자유롭게

- 이 저작물을 복제, 배포, 전송, 전시, 공연 및 방송할 수 있습니다.

다음과 같은 조건을 따라야 합니다:



저작자표시. 귀하는 원저작자를 표시하여야 합니다.



비영리. 귀하는 이 저작물을 영리 목적으로 이용할 수 없습니다.



변경금지. 귀하는 이 저작물을 개작, 변형 또는 가공할 수 없습니다.

- 귀하는, 이 저작물의 재이용이나 배포의 경우, 이 저작물에 적용된 이용허락조건을 명확하게 나타내어야 합니다.
- 저작권자로부터 별도의 허가를 받으면 이러한 조건들은 적용되지 않습니다.

저작권법에 따른 이용자의 권리는 위의 내용에 의하여 영향을 받지 않습니다.

이것은 [이용허락규약\(Legal Code\)](#)을 이해하기 쉽게 요약한 것입니다.

[Disclaimer](#)

Doctoral Thesis

Characterizations of the Antarctic Sea Ice Using  
Multiple Satellite Remote Sensing Data

Miae Kim

Department of Urban and Environmental Engineering  
(Environmental Science and Engineering)

Graduate School of UNIST

2018

# Characterizations of the Antarctic Sea Ice Using Multiple Satellite Remote Sensing Data

Miae Kim

Department of Urban and Environmental Engineering  
(Environmental Science and Engineering)

Graduate School of UNIST

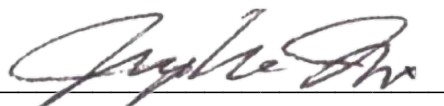
# Characterizations of the Antarctic Sea Ice Using Multiple Satellite Remote Sensing Data

A dissertation  
submitted to the Graduate School of UNIST  
in partial fulfillment of the  
requirements for the degree of  
Doctor of Philosophy

Miae Kim

July/9/2018

Approved by



Advisor

Jungho Im

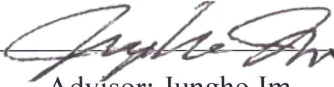
# Characterizations of the Antarctic Sea Ice Using Multiple Satellite Remote Sensing Data

Miae Kim

This certifies that the dissertation of Miae Kim is approved.

July/9/2018

signature

  
Advisor: Jung-ho Im

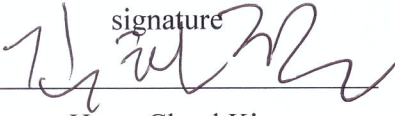
signature

  
Myong-In Lee


signature

  
Kyung Hwa Cho

signature

  
Hyun-Cheol Kim

signature

  
Hyangsun Han

# Abstract

Sea ice closely interacts with the atmosphere and ocean systems. Land fast sea ice (fast ice) is a kind of sea ice attached to the shore, ice shelves, or grounded icebergs. It is widely distributed along the Antarctic coast and acts as an interface between the atmosphere and the ocean, affecting heat balance feedback, thermal insulation effects, and deep water formation depending on the temporal and spatial effects of the environmental conditions. It also plays an important role in the biological aspects of Antarctica. Attached to the Antarctic glacier is strongly associated with calving events of ice shelf as it is physically coupled with glaciers at the terminus. The existing Antarctic fast ice has been mainly focused on the East Antarctic, especially for the research on long-term fast ice. Several case studies for West Antarctic fast ice with satellite images were performed in local areas. Various types of satellite data and detection techniques were utilized to successfully detect fast ice. In addition, long-term fast ice maps specifically focused on the Amundsen sea of West Antarctica were generated to investigate the distribution and variability of fast ice.

This thesis reports the results of fast ice detection algorithms that have been developed using various satellite images that can be used for fast ice detection. Along with the use of multiple satellite data, the proposed fast ice detection algorithms can more effectively detect fast ice, which then allows to obtain more accurate fast ice detection and produce long-term fast ice with high accuracy. Especially, the distribution and variability of time-series fast ice in West Antarctica, which is more concentrated in the Amundsen Sea, were analyzed together with bathymetry data and the distribution of glacier icebergs.

In order to detect fast ice, machine learning techniques were basically used in this thesis. Two classes (i.e. fast ice and non-fast ice) were classified. Using MODIS images, there was a problem that fast ice was not produced in cloud cover areas and the polar night season, which is winter season in Antarctica. MODIS and AMSR-E satellite data were selectively used to solve the cloud contamination problem. Correlation-related variables were finally added based on the fact that fast ice is motionless for a certain period of time, and fast ice detection was performed at 15-day intervals using the improved input variables. Active microwave sensor data, ALOS PALSAR, was also used to detect fast ice and to validate fast ice detection results. Its high-spatial resolution allows to extract fast ice boundary more accurately. Fast ice detections showed good agreement with available ALOS PALSAR SAR images and MODIS reflectance images. Nearly decade-long fast ice extents were produced in the Amundsen Sea of West Antarctica and analyzed in terms of spatiotemporal variations with bathymetry and icebergs calved from ice shelves in study area. In addition, anomalous fast ice breakup events were examined, which suggests the importance of fast ice on the stability of ice shelves.

## Contents

List of Figures .....	viii
List of Tables.....	xi
List of Acronym .....	xii
Chapter 1.....	1
Introduction.....	1
1.1. Importance of the Antarctic sea ice.....	1
1.2. Background and importance of landfast sea ice .....	2
1.3. Satellite remote sensing of fast ice .....	4
1.4. Machine learning techniques for fast ice detection.....	6
1.5. Goals of this dissertation.....	9
Chapter 2.....	10
Landfast sea ice monitoring using multisensory fusion in the Antarctic .....	10
2.1. Abstract .....	10
2.2. Introduction .....	11
2.3. Data.....	12
2.4. Methods.....	14
2.5. Results and discussion .....	17
2.6. Conclusions .....	27
Chapter 3.....	28
Object-based landfast sea ice classification over West Antarctica using synthetic aperture radar of ALOS-1 PALSAR .....	28
3.1. Abstract .....	28
3.2. Introduction .....	29
3.3. Data and Methods .....	30
3.4. Results and Discussion.....	40
3.5. Conclusions .....	50
Chapter 4.....	51
Distribution and variability of landfast sea ice along the Amundsen Sea of West Antarctica.....	51
4.1. Abstract .....	51
4.2. Introduction .....	52

4.3. Study area.....	53
4.4. Data and Methods .....	53
4.5. Results and Discussion.....	58
4.6. Conclusions and Future Work .....	67
Chapter 5.....	68
Overall conclusions and Future research .....	68
References.....	70



## List of Figures

Figure 1. 1. Schematic representation of a hypothetical scenario showing some of the most common sea-ice related features including fast ice, pack ice, multiyear ice floe, first-year ice floe, and so on. Source: Wikipedia.....	2
Figure 1. 2. Schematic representation of key dates in the emperor penguin annual breeding cycle with the timing of fast ice formation and breakup. Source: Massom et al. (2009).....	3
Figure 1. 3. Diagram of PhD dissertation research .....	9
Figure 2. 1. The process flow of the research.....	16
Figure 2. 2. Box plots of the producer’s accuracy and user’s accuracy for quantitative examination of the fast ice mapping results of (a) decision trees and (b) random forest. For full color versions of the figures in this paper, please see the online version.....	19
Figure 2. 3. Comparison of fast ice mapping results by model with the 250-m MODIS images during the periods of relatively stable fast ice around (a) Mertz and (b) Abbot Ice Shelf in the East and West Antarctica, respectively. The lines in (a) and (b) indicate fast ice edges delineated from the MODIS images based on visual interpretation. Decision tree results are shown in (c) and (d), while random forest results are in (e) and (f). MODIS images with the maximum fast ice cover were used as background images in (a) and (b). .....	21
Figure 2. 4. Comparison of fast ice mapping results by model with the 250-m MODIS images during the periods of rapidly changing fast ice around (a) Mertz and (b) Abbot Ice Shelf in the East and West Antarctica, respectively. The lines in (a) and (b) indicate fast ice edges delineated from the MODIS images based on visual interpretation. Decision tree results are shown in (c) and (d), while random forest results are in (e) and (f). MODIS images with the maximum fast ice cover were used as background images in (a) and (b). .....	22
Figure 2. 5. Fast ice maps using random forest in 2003 for (a) composite 5 (81 – 100 Julian days) and (b) composite 13 (241 – 260 Julian days). Magenta areas represent fast ice in the Antarctic, and hatched areas with gray color indicate that MODIS IST was not available for the composite. ...	24
Figure 2. 6. (a) Temporal variation of the availability of MODIS IST data in the East and West Antarctic regions. (b) The ratio of the IST coverage in the West Antarctic (WA) relative to the East Antarctic (EA) in percentage. (c) Box plot of the IST coverage in percentage by composite.....	25
Figure 2. 7. Temporal variation of fast ice areas in the East and West Antarctic. Due to the lack of the input data during the Australian winter season, composites 6 – 12 for each year were not available. ....	26
Figure 2. 8. Temporal variation of fast ice in the Antarctic using a) the simple counting approach and b) the weighted average approach.....	26
Figure 3. 1. Data process flow chart of the proposed approach in this study. ....	31
Figure 3. 2. Map of study area including landfast sea ice regions over West Antarctica with ALOS PALSAR images over the Weddell Sea, Bellingshausen Sea, Amundsen Seas, and Ross Sea sectors. Regions (red letters) in Weddell Sea were used for constructing training and test datasets and the other regions (blue letters) for validation. ....	32

- Figure 3. 3. Example of SAR images in a 5-day time gap used to detect fast ice edge for reference over Amundsen Sea and Bellingshausen Sea sectors. The Antarctic continent and ice shelves are shown in dark gray and white, respectively. The text in italic shows fast ice and pack ice (non-fast ice) regions. .... 38
- Figure 3. 4. Maps of landfast sea ice region at the Getz Ice Shelf over Amundsen Sea with SAR images of two dates (top row) and MODIS images available between 31 October 2010 and 5 November 2010 (middle and bottom rows). .... 39
- Figure 3. 5. Examples of segmentation results at different (a) scale parameters with fixed thresholds for shape of 0.1 and compactness of 0.5, (b) shape parameters with scale of 25 and compactness of 0.5, and (c) compactness parameters with scale of 25 and shape of 0.1 parameter setting. The red solid line indicates reference fast ice edge. The background is a false color composite image of date 1 (green) and date 2 (blue). .... 41
- Figure 3. 6. Input variables extracted based on segmentation result including (a) correlation, (b) slope, (c) intercept, (d) mean of backscatter coefficient (in dB) for combined dates 1 and 2, (e) standard deviation of backscatter coefficient for combined dates 1 and 2. Gray area is the Antarctic land, and red and blue solid lines over sea ice zone indicate the reference fast ice edge. .... 42
- Figure 3. 7. Relative variable importance results indicated by (a) mean decrease accuracy of random forest and (b)  $-\log_{10}(\text{p-value})$  of logistic regression model. .... 44
- Figure 3. 8. Landfast sea ice detection results at the Bellingshausen Sea region of (a) random forest (RF), (b) extremely randomized trees (ERT), and (c) logistic regression (LR) models. Red solid lines indicate the reference fast ice edge, RF and ERT results are shown in pink color and LR result for the probability of fast ice coverage in yellowish-starched color, and gray area is Antarctic land. .... 46
- Figure 3. 9. Landfast sea ice detection results at the Brunt ice shelf at the eastern Weddell Sea site of (a) random forest (RF), (b) extremely randomized trees (ERT), and (c) logistic regression (LR) models. Red solid lines indicate the reference fast ice edge, RF and ERT results are shown in pink color and LR result for the probability of fast ice coverage in yellowish-starched color, and gray area is Antarctic land. .... 46
- Figure 3. 10. Landfast sea ice detection results at the Larsen ice shelf of the Antarctic Peninsula of (a) random forest (RF), (b) extremely randomized trees (ERT), and (c) logistic regression (LR) models. Red solid lines indicate the reference fast ice edge, RF and ERT results are shown in pink color and LR result for the probability of fast ice coverage in yellowish-starched color, and gray area is Antarctic land. .... 47
- Figure 3. 11. Landfast sea ice detection results at the Nickerson ice shelf in the east of the Ross Sea of (a) random forest (RF), (b) extremely randomized trees (ERT), and (c) logistic regression (LR) models. Red solid lines indicate the reference fast ice edge, RF and ERT results are shown in pink color and LR result for the probability of fast ice coverage in yellowish-starched color, and gray area is Antarctic land. .... 48
- Figure 3. 12. Qualitative analysis results. (a) Backscatter image of L-band HH-pol ALOS PALSAR for date 1; (b) backscatter for date 2; (c) comparison between the Antarctic Ice Chart and RF result (pink area). The light blue and red hatched areas are from the Antarctic Ice Chart. SD, F, IC are abbreviations for ice chart codes meaning Stage of Development, Form of ice, and sea Ice Concentration, respectively. The blue solid line is fast ice edge as a reference. (d-f) Results of machine learning models (RF, ERT, LR, respectively) with fast ice edge as a reference (red solid line). .... 49

Figure 4. 1. Process flow diagram..... 53

Figure 4. 2. Process flow diagram..... 56

Figure 4. 3. Relative importance of variables for landfast sea ice mapping model for algorithm 1. ... 59

Figure 4. 4. Relative importance of variables for landfast sea ice mapping model for algorithm 2. ... 59

Figure 4. 5. Overall accuracy for out-of-bag error of random forest model by season and algorithm. 60

Figure 4. 6. Examples of ALOS PALSAR images and corresponding fast ice maps for (a) Land Ice Shelf fast ice site on 31 October 2010 and (b) Sulzberger Ice Shelf fast ice site on 15 May 2008. SAR images for Land Ice Shelf site were acquired on 15 October 2010 and 27 October 2010, and for Sulzberger Ice Shelf site on 10 May 2008 and 21 May 2008. Fast ice maps of the date closest to each date were used. The red solid lines indicate reference fast ice edges delineated based on the SAR images. Light blue area in the bottom figures are the fast ice region detected by random forest model..... 61

Figure 4. 7. Total frequency of fast ice residence for the period of from July 2002 to August 2011... 63

Figure 4. 8. Supplementary data (a) bathymetry from the IBCSO Version 1.0 and (b) ALOS PALSAR SAR image acquired on 05 August 2007 for the dashed box in (a). ..... 63

Figure 4. 9. Mean annual cycle of fast ice extent for the entire study area. .... 65

Figure 4. 10. Fast ice time series for the Land Ice Shelf site including (a) fast ice extent and (b) its anomaly with a linear trend as a solid line. .... 65

Figure 4. 11. Fast ice time series for the Sulzberger Ice Shelf site including (a) fast ice extent and (b) its anomaly with a linear trend as a solid line. .... 65

Figure 4. 12. MODIS images that show fast ice breakup event occurred in the Land Ice Shelf. .... 66

## List of Tables

Table 2. 1. Input variables and reference data information. ....	12
Table 2. 2. Accuracy assessment results for decision trees using the test data-set.....	18
Table 2. 3. Accuracy assessment results for random forest using the test data-set. ....	19
Table 2. 4. Attribute usage of the decision trees model. ....	19
Table 2. 5. Mean decrease accuracy calculated using out-of-bag data when a variable was permuted in random forest. The greater the decrease in accuracy, the more contributing the variable was.....	19
Table 3. 1. The information of ALOS PALSAR image sets. All the image pairs have time interval of 5 days. ....	34
Table 3. 2. Input variable information. ....	36
Table 3. 3. Accuracy assessment result of the random forest model for the test dataset. ....	43
Table 3. 4. Accuracy assessment result of the extremely randomized trees model for the test dataset.	43
Table 3. 5. Accuracy assessment result of the logistic regression model for the test dataset. ....	44
Table 4. 1. Input variables used in this study to detect fast ice. ....	56
Table 4. 2. Number of samples for fast ice and non-fast ice class by season and algorithm. ....	56
Table 4. 3. Information of ALOS PALSAR SAR images used for model validation during study period from July 2002 to September 2011. ....	56
Table 4. 4. Accuracy assessment results of landfast sea ice maps based on SAR images. ....	61

## List of Acronym

<b>ALOS PALSAR</b>	The Advanced Land Observing Satellite Phased Array L-band Synthetic Aperture Radar
<b>AMSR-E</b>	The Advanced Microwave Scanning Radiometer for the Earth observing system
<b>ASF</b>	Alaska Satellite Facility
<b>AVHRR</b>	The Advanced Very High Resolution Radiometer
<b>Bagging</b>	Bootstrap aggregating
<b>CART</b>	Classification and Regression Trees
<b>dGR</b>	Difference between GRs
<b>DT</b>	Decision trees
<b>ENSO</b>	El Nino-Southern Oscillation
<b>ERS</b>	European Remote Sensing
<b>ERT</b>	Extremely randomized trees
<b>Fast ice</b>	Landfast sea ice
<b>GR</b>	Spectral Gradient Ratio
<b>InSAR</b>	Interferometric SAR
<b>IST</b>	Ice surface temperature
<b>LR</b>	Logistic regression
<b>MDA</b>	Mean decrease accuracy
<b>MODIS</b>	The Moderate Resolution Imaging Spectroradiometer
<b>NCI</b>	Neighborhood correlation images
<b>NESZ</b>	The noise-equivalent sigma-zero
<b>Non-fast ice</b>	Non-landfast sea ice
<b>NSIDC</b>	National Snow & Ice Data Center
<b>OA</b>	Overall accuracy
<b>OCI</b>	Object correlation images
<b>OOB</b>	Out-of-bag
<b>PA</b>	Producer's accuracy
<b>RF</b>	Random Forest
<b>PR</b>	Polarization ratio

<b>SAM</b>	Southern Annular Mode
<b>SAR</b>	Synthetic aperture radar
<b>ScanSAR</b>	Scanning Synthetic Aperture Radar
<b>SIC</b>	Sea ice concentration
<b>SOI</b>	Southern Oscillation Index
<b>SSM/I</b>	The Special Sensor Microwave/Imager
<b>SSMIS</b>	The Special Sensor Microwave Imager/Sounder
<b>STD</b>	Standard deviation
<b>TB</b>	Brightness temperatures
<b>TIR</b>	Thermal infrared
<b>UA</b>	User's accuracy

# Chapter 1

## Introduction

### 1.1. Importance of the Antarctic sea ice

Sea ice plays a major role in climate and marine systems, and various satellite observations and numerical models have shown that sea ice greatly affect heat balance feedback, thermal insulation effects, and deep water formation. Changes in sea ice interact with the atmosphere and the ocean. Since sea ice have high albedo, it can change the surface radiation balance by reflecting incoming solar radiation (Marsland et al., 2001). It results in a positive feedback between the atmosphere and the ocean, which ultimately leads to sea ice re-cooling and further accelerating sea ice growth (Yuan et al., 2001; Marsland et al., 2001; Spreen et al., 2008). The Antarctic cryosphere, which includes sea ice and glacier ice types, can also contribute to deep water formation and thus ultimately affect global thermohaline circulation (Zwally et al., 1983; Bintanja et al., 2013; Ohshima et al., 2013). Brine rejection due to sea ice formation produces negative feedback in relation to the ocean. As the density of the surface seawater increases during sea ice formation, the vertical stability of the ocean is lowered, enhancing vertical convection. It makes the temperature of the deep water high and increases the oceanic heat flux, which eventually prevents sea ice growth and lead to feedback on sea ice melt. On the other hand, during the formation of sea ice, the surface layer of seawater has a lower temperature than that of the below, which leads to sea ice growth. If sea ice is fully grown, the salinity of the mixed layer increases and becomes equal to deep water. The high salinity of deep water is the starting point of the deep oceanic circulation of the deep ocean. As a result, the vertical seawater temperature and salinity become nearly uniform, which makes the surface ocean temperature warm. It then results in the occurrence of polynya. At this time if the cold atmosphere cools the surface layer, the vertical stability can be reduced again, and convection can occur by the influence of the atmosphere.

The large interannual variability in sea ice extent have been widely studied as one of the critical phenomena related to climate change (Cavalieri et al., 2003; Giles et al., 2008; Holland et al., 2012). The impact of climate change on the Antarctic sea ice is different from the Arctic. The Antarctic sea ice extent has been statistically on the rise since the last 1985 (Zwally et al., 2002; Cavalieri and Parkinson, 2008; Simmonds, 2015; Parkinson and DiGirolamo, 2016; Comiso et al., 2017). On the contrary to the global climate change scenarios, the Antarctic sea ice expansion has been considered an exceptional phenomenon (Turner et al., 2017; Viñas, 2017). However, Antarctic sea ice cover has dropped to its lowest on record, which means that monitoring of Antarctic sea ice has become more important in the projection of future sea ice due to climate change (Stuecker et al., 2017; Turner et al., 2017).

## 1.2. Background and importance of landfast sea ice

Fast ice is a motionless sea ice that forms along the coastline persisting from few days to multiple years, compared to pack ice that drifts on the sea surface by winds (Figure 1. 1). Fast ice is fastened to an ice wall, ice front, or between grounded icebergs (WMO, 2014). Fast ice is a prevalent feature around the Antarctic coastal regions especially during austral winter. There is no definite standard for the length of time that fast ice must be present (Mahoney et al., 2006). Previous studies performed fast ice study at intervals of 3 to 20 days (Barry et al., 1979; Mahoney et al., 2006; Fraser et al., 2010). For the East Antarctic fast ice, fast ice has been created at intervals of 20 days (Fraser et al., 2010; Fraser et al., 2012), and the total average fast ice extent for a whole study period was obtained (Nihashi et al., 2015). The time period required will depend on the purpose of research and the intra-annual variability of the breakup and advance of fast ice in each study area.

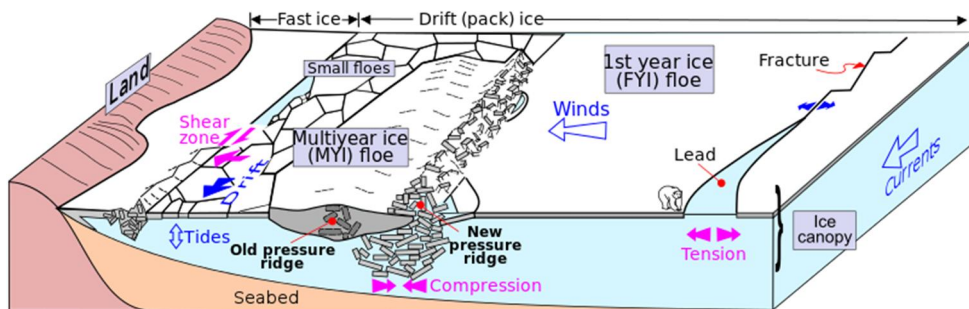


Figure 1. 1. Schematic representation of a hypothetical scenario showing some of the most common sea-ice related features including fast ice, pack ice, multiyear ice floe, first-year ice floe, and so on. Source: Wikipedia.

Fast ice forms in two formation regimes; 1) wind-driven advection of pack ice as dynamic process and 2) direct freezing of seawater as a thermodynamic process (Fraser et al., 2012). The regime 1 occurs at regions characterized by coastal protrusion such as coastal promontory and tabular grounded icebergs, and ice tongues. Fast ice forms at the upstream of the protrusion by the advection of pack ice in the direction of wind blowing. It can extend far offshore up to hundreds of kilometers by assistance from grounded icebergs as anchor points (Massom et al. 2001; Miles et al., 2017). The regime 2 is the mechanism by which fast ice is created thermodynamically between grounded icebergs. The fast ice regions are generated without the dependence on the drift of pack ice, and generally show a short distance from the coast.

Although fast ice extent is a relatively small portion of total sea ice extent, its thickness and volume



can account for much larger part, specifically for East Antarctica up to 40% of total sea ice volume (Giles et al., 2008). The distribution of fast ice is widespread along the shoreline of East Antarctica compared to West Antarctica (Fraser et al., 2012; Nihashi et al., 2015), while the thickness of the West Antarctic sea ice is thicker than that of East Antarctica (Worby et al., 2008). The thickness of fast ice determines the patterns of fast ice breakup and further the ratio of first-year ice to multi-year ice. Furthermore, even if thin sea ice disappears responding to the climate changes, thick sea ice is retained and contributes to the overall sea ice volume.

Fast ice is affected spatially by the atmosphere and the ocean locally, regionally, or remotely from a short period of time to a long term (Yuan et al., 2004; Fraser et al., 2012; Aoki et al., 2017). It is important to investigate the detection and distribution of fast ice by separating from floating pack ice. Fast ice interacts with the atmosphere and the oceans acting as an important interface between the ice sheet, pack ice, and the oceans, and also affects the biological processes (Fraser, 2011). The distribution of fast ice greatly affects the shape and size of polynya. Major polynyas in Antarctica account for about 10% of sea ice formation in the Southern Ocean (Tamura et al., 2008; Nihashi et al., 2015). Brine rejection by the formation of sea ice in the polynya region forms dense seawater and is thus the source of the Antarctic Bottom Water (Massom et al., 2001; Ohshima et al., 2013; Nihashi and Ohshima, 2015). Fast ice attached to ice shelves also physically couples with the shelves to serve as a buttress at the terminus of ice shelf, thus slowing the calving and affecting the stability of ice shelf, which ultimately can affect the Antarctic mass balance (Bintanja et al., 2013). Furthermore, as shown in Figure 1.2, fast ice plays an important role in providing extensive habitats and successful breeding places for Antarctic microorganisms, Emperor penguins, and Weddell seals (Fuiman et al., 2002; Massom et al., 2009). The distribution and seasonality of fast ice can have practical influences on scientific exploration and research such as ship navigation and in-situ sampling strategy (Uto et al., 2006; Ushio, 2006; Parkinson and Cavalieri, 2012; Normile, 2015).

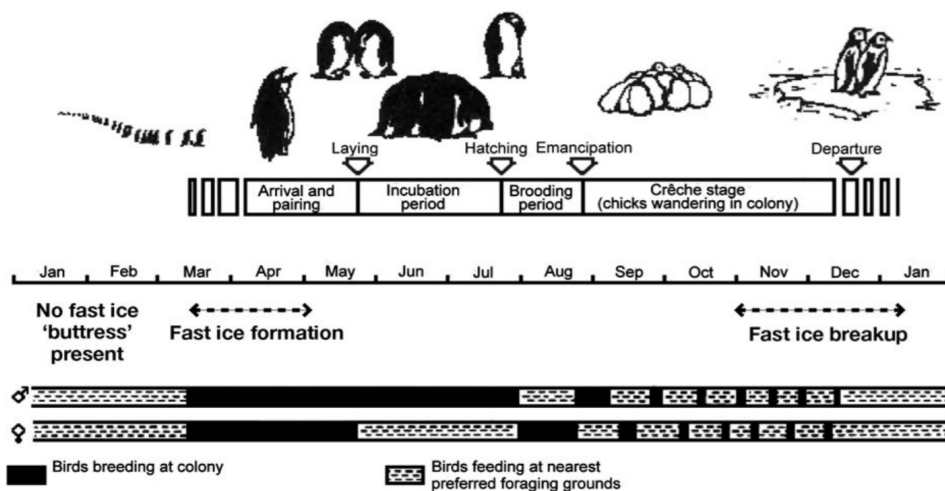


Figure 1. 2. Schematic representation of key dates in the emperor penguin annual breeding cycle with

the timing of fast ice formation and breakup. Source: Massom et al. (2009).

### 1.3. Satellite remote sensing of fast ice

Monitoring of the Antarctic fast ice has been conducted using in situ observations (Murphy et al., 1995; Ushio, 2006; Heil et al., 2011) and satellite remote sensing (Fraser et al., 2012; Giles et al., 2008; Massom et al., 2010; Fraser et al., 2009; Fraser et al., 2010; Fraser, 2011; Mahoney et al., 2007). Spatial distribution and thickness of the fast ice in Prydz Bay, East Antarctica, were investigated by the Antarctic Fast Ice Network project, a representative research program of in situ observations of the Antarctic fast ice promoted by Antarctic Climate & Ecosystems during the period of 1950–2021 (Heil et al., 2011). However, the field measurements have limitations in time and space due to the harsh weather conditions in polar regions. In-situ measurements for fast ice research are generally limited to fixed locations where ice is relatively thick enough for sampling. Satellite remote sensing can be used as an alternative way of monitoring fast ice in the unfavorable conditions, and there is no option but to use it for long-term sea ice research as it covers vast areas with high temporal resolution.

Our knowledge of sea ice has increased considerably since the introduction of polar observing satellites. Satellite sensors such as passive and active microwave, visible, and infrared sensors extract various sea ice surface characteristics and have been used to develop various sea ice models. Sea ice have different physical temperatures and radiometric properties depending on salinity, reflectance, and surface roughness. Satellite-based research on fast ice can be divided into three categories in terms of sensor types by optical, active microwave, and passive microwave sensors. Sea ice has a lower temperature in optical sensor images than the surrounding open water. Optical sensor images are useful for separating fast ice and non-fast ice that include part of the ocean. Optical sensors such as Landsat, MODIS, and AVHRR have low and medium spatial resolution from dozens of meters to a few kilometers, while they observe the same area at least every other day (except the Landsat series). However, optical sensors have limitations including the fact that they cannot observe the surface under cloudy sky or at night. As the cloud cover rate is relatively high (approximately 60-80% cloud cover depending on location and season) over the Antarctic regions (Comiso and Stefen, 2001; Spinhirne et al., 2005; Suen et al., 2014; Scott et al., 2017), optical sensor data might not be an optimum solution to carefully monitor fast ice regions. Considering the effect of cloud contamination, previous studies have detected fast ice using optical sensor data by compositing images with dozens of days (Fraser et al. 2010; Fraser et al., 2012). Fraser et al. (2009) used TIR and visible MODIS data to produce cloud-free composite images for fast ice detection at the Mertz Glacier Tongue, East Antarctica. Cloud-free TIR/visible AVHRR images were used for investigating the distribution and variations of fast ice along the Adélie coast, East Antarctica (Massom et al. 2009).

Microwave sensors including passive and active microwave remote sensing have been widely used to detect and monitor sea ice because they can observe surfaces regardless of atmospheric conditions and presence of sunlight. Passive microwave sensors measure radiation emitted from the surface. Thermal infrared radiation is affected by the physical temperature of an object, while passive microwave radiation is mainly influenced by the emissivity of the radiating object. Emissivity is defined as the rate of radiation emitted from a given object to radiation from a black body at the same physical temperature. When using microwave radiation for sea ice studies, the emissivity in the microwave region for sea ice is affected by the physical composition and characteristics of sea ice such as salinity, surface roughness, water vapor contents, and crystalline structure (Shokr and Shinha, 2015). However, some of these parameters, such as salinity and the geometrical properties of brine pockets, are affected by the physical temperature of the sea ice. Therefore, the sea ice temperature influences the parameters and ultimately affects the emitted radiation. Ice crystals emit higher energy, emissivity of sea ice is higher than that of open water. Therefore, sea ice is physically cooler than ocean but radiometrically warmer.

Passive microwave sensors such as AMSR-E, SSM/I, and SSMIS can be successfully utilized for global-scale research on sea ice. In the previous study that utilized the optical sensor images, passive microwave sensor data were used as supplementary data for parts that are not detected due to cloud cover (Fraser et al., 2010). Another study used only the passive microwave data to develop fast ice detection model (Nihashi et al., 2015). Furthermore, the passive microwave sensors can be successfully used for time series monitoring of sea ice at a global scale because they observe the entire Arctic and Antarctic areas every day. Meanwhile, passive microwave data have coarse spatial resolution (~10-50 km), limiting their applications to narrow fast ice zone near the shoreline.

Active microwave is also known as radar, which is short for radio detection and ranging, and the imaging radar systems transmit pulses with a transmitter and measure backscatter of the signal reflected or scattered from the surface. Radar systems that are widely used in sea ice research include imaging radar, scatterometer, and radar altimetry. Imaging data is generated from observations of the radar system in terms of active microwave. Radar systems measure the backscatter, that is, the scattering of the emitted radar signal back to the sensor. When radar systems scan the surface with a specific swath, the radar pulse is transmitted from one-side-looking antenna. In general, strong backscatter results from a rough surface or a volume with multiple scattering elements. Radar systems have been used for sea ice studies by providing multiple imaging modes with various resolutions and swath widths for example ALOS PALSAR and RadarSat ScanSAR mode. Scatterometer has been mainly used for oceanographic studies by measuring wind velocity and wind direction (for example, WindSat), and has been used in sea ice research as well such as NASA QuikSCAT satellite. Radar altimeters, nadir-looking instruments, have been used to map glacier topography and to determine thickness of sea ice. The ERS satellite -1 and 2, and CryoSat-2 are representative examples.

Active microwave sensor data, such as SAR, can be a powerful instrument for fast ice research because it can observe sea ice in high spatial resolution. SAR has been used for classification of sea ice types because backscattered radar intensity is dependent on surface roughness and sea ice properties (Karvonen, 2004; Zakhvatkina et al., 2013; Liu et al., 2015; Ressel et al., 2015; Wang et al., 2016; Casey et al., 2016). Mahoney et al. (2004) used vector gradient differences generated from three consecutive SAR images to detect fast ice edges. The method was successfully applied in the mid-winter season, but manual examination was needed for the other seasons. Image correlation analysis based on a feature-tracking algorithm was conducted by Giles et al. (2008) for detection of fast ice regions in East Antarctica using RADARSAT ScanSAR images in 1997 and 1999. This technique is more feasible when image pairs with intervals of several weeks are used. Most recently, InSAR approaches have been applied to distinguish fast ice regions (Meyer et al., 2011; Han et al., 2015). However, the scattering properties of sea ice can change over time in SAR data with a long repeat cycle (e.g. 46 days for ALOS PALSAR), which then results in a loss of coherence and incomplete detection of fast ice regions. Despite their advantages, it is difficult to investigate sea ice at a continental or global scale using SAR due to their narrow observation area.

As optical and microwave sensors have distinct strengths and weaknesses, several researchers have tried to fuse the strengths of each sensor for mapping the fast ice over a wide area. Fraser et al. (2009) suggested a method of time series compositing cloud-free imagery from MODIS to detect fast ice in the East Antarctic, in which brightness temperature and concentration of sea ice derived by SSM/I with 25-km spatial resolution were used to define the extent of fast ice. Fraser et al. (2010) improved the accuracy of fast ice detection by replacing the products derived by SSM/I with those by AMSR-E, of which the spatial resolution is 6.25 km. Ushio (2006) analyzed the distribution and variations of fast ice in Lützow-Holm Bay, East Antarctica, with a time series of TIR images from AVHRR data and in situ measurements. The distribution of pack ice was determined with sea ice concentration data from SSM/I images.

#### **1.4. Machine learning techniques for fast ice detection**

Machine learning techniques have been applied to various remote sensing applications to solve both classification and regression problems including land cover classification, change detection, and biophysical parameter estimation (Maxwell et al., 2014; Ghimire et al., 2012; Li et al., 2013; Kim et al., 2014; Long et al., 2013; Rhee et al., 2014). In this study, machine learning techniques are used as a modeling method for fast ice detection by combining with input variables from multiple satellite data. A wide range of machine learning methods are used in this dissertation such as DT, RF, ERT, and LR.

DT uses recursive binary splits to extract patterns or rules in a data-set. As it produces rule-based results (if-then rules), users can interpret the results in a more straightforward and easier way than other methods such as artificial neural networks. RF is a collection (i.e., ensemble) of DT using a Bagging method. It constructs independent trees with random sampling and combines final results from the trees using an ensemble method such as voting or weighted voting for classification. RF creates a collection of trees based on CART, which is a rule based DT (Breiman, 2001). Each tree is grown using two randomizations in selecting training samples and split variables to overcome the limitations of CART, including dependency on a single tree and sensitivity to training samples. A subset of the training samples (typically 67% of the samples) is randomly selected, and the remaining samples (out-of-bag data) are used to internally validate the model. The second randomness is that in each node of a tree, a subset of input variables (typically  $\sqrt{n}$  with  $n$  as the number of input variables) is randomly selected. The grown trees are then combined using either a simple majority voting or a weighted majority voting strategy.

See5.0, a commercial program developed by RuleQuest Research, Inc. (Quinlan, 2013), was used to implement DT. RF was implemented in R software with an add-on package of RF (Liaw and Wiener, 2002). In this study, options used for constructing a RF model in R were set as default for the number of trees (500) and variables sampled at each node (generally  $\sqrt{n}$  where  $n$  is the number of input variables) and the minimum size of terminal nodes. It also provides relative variable importance as MDA. MDA is calculated using OOB data, which is left out of training data in each tree. Misclassification rates are calculated using OOB data and a variable-permuted OOB data using a given tree, which is repeated for all trees. MDA means the average increase in the misclassification rate. A higher MDA indicates more important variable in classifying fast and non-fast class.

ERT is a relatively new tree-based ensemble classifier method compared to RF (Geurts et al., 2006). It extends RF by introducing a different randomization to splitting at nodes. While RF finds the best node splitting points among the input variables selected at each node when constructing trees, ERT performs node splitting fully at random and uses the same variable set with no bagging for each tree, further reducing the variance between trees and minimizing the bias. ERT was implemented using the add-on package of “ExtraTrees” in R with default parameters.

LR is a regression model applicable to categorical variables to estimate the probability of an event occurrence. Similar to a linear regression model, it models the relationship between independent variables and dependent variables with a specific function. LR is used for classification as output ranging from 0 to 1 that is divided by a fixed threshold by using a logistic (sigmoid) function (4).

$$\text{Prob}(Y|X_1, X_2, \dots, X_n) = \frac{1}{1 + \exp[\sum_{i=1}^n w_i X_i]} \quad (4)$$

where  $\text{Prob}(Y|X_1, X_2, \dots, X_n)$  is the probability of the dependent variable  $Y$  given  $(X_1, X_2, \dots, X_n)$ ,  $n$  is the number of independent variables,  $X_i$  is an  $i^{\text{th}}$  independent variable, and  $w_i$  is the coefficient for variable  $X_i$ . The logistic function estimates the probability of an event (i.e. fast ice or non-fast ice). In this study, LR was implemented in R using “glm” add-on package.

Both machine learning models provide relative variable importance that can be used to examine the contribution of each input variable for fast ice mapping. See 5.0 provides attribute usage information that shows how frequently a variable is used at each split. RF provides MDA in classification when a variable is permuted, which means that the greater the decrease in accuracy, the more important the variable is.

Model performance was evaluated using accuracy metrics that can be obtained from confusion matrices based on the test dataset. Accuracy metrics include PA and UA, OA, and kappa coefficients. Those are calculated by using formulas below. It is based on the classification between fast ice and non-fast classes.

$$\text{Producer's accuracy} = \frac{\text{the number of correctly classified pixels}}{\text{the number of reference pixels for a class}} \times 100 \quad (\text{Eq. 1})$$

$$\text{User's accuracy} = \frac{\text{the number of correctly classified pixels as a class}}{\text{a total number of pixels classified as a class}} \times 100 \quad (\text{Eq. 2})$$

$$\text{Overall accuracy} = \frac{\text{a total number of correctly classified pixels for both classes}}{\text{a total number of reference pixels for both classes}} \times 100 \quad (\text{Eq. 3})$$



## 1.5. Goals of this dissertation

The goals of this dissertation are classified into three folds and illustrated in Figure 1. 3.

1. To map fast ice regions in the entire Antarctic coastal zone by combining multisensory data including optical and passive microwave sensor data with machine learning techniques during the period from 2003-2008 to achieve an automated fast ice classification that resolve the limitation of manually classifying fast ice of previous studies.
2. To detect fast ice regions over the West Antarctic by combining image segmentation, object correlation image method, and machine learning techniques with composite SAR images with a short time gap (i.e. 5 days), which can detect sea ice regardless of weather conditions, to analyze fast changing fast ice regions.
3. To analyze long-term fast ice distribution and variability in the Amundsen Sea of West Antarctica by combining optical and passive microwave sensor data with a machine learning method, and then to investigate on an anomalous fast ice breakup event.

Through these three goals, the ultimate achievements of this dissertation are to produce time series of fast ice extent in a short time interval and to investigate the distribution and variability of fast ice in the West Antarctic coastal regions in a global warming climate. This research will much improve the understanding of fast ice in Antarctica especially for West Antarctica and the response of fast ice to climate changes.

### PhD Dissertation Research

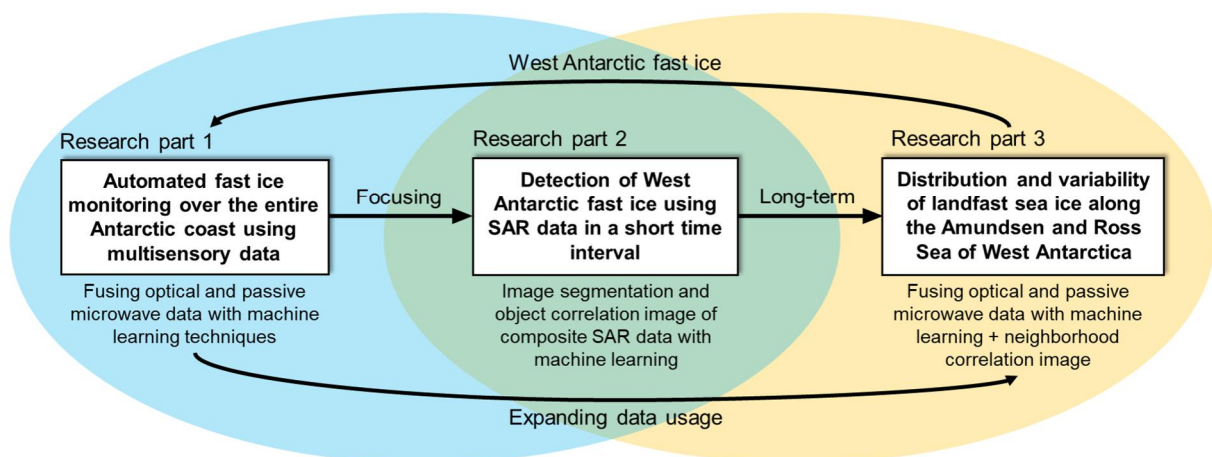


Figure 1. 3. Diagram of PhD dissertation research

## Chapter 2

### Landfast sea ice monitoring using multisensory fusion in the Antarctic

#### 2.1. Abstract

Fast ice means sea ice that is attached to the shoreline with little or no motion in contrast to pack ice which drifts on the sea. As fast ice plays an important role in the environmental and biological systems of the Antarctic, it is crucial to accurately monitor the spatiotemporal distribution of fast ice. Previous studies on fast ice using satellite remote sensing were mostly focused on the Arctic and near-Arctic areas, whereas few studies were conducted over the Antarctic, especially the West Antarctic region. This research mapped fast ice using multisensor data from 2003 to 2008 based on machine learning approaches – DT and RF. A total of seven satellite-derived products, including AMSR-E brightness temperatures and sea ice concentration, MODIS IST and SSM/I ice velocity, were used as input variables for identifying fast ice. RF resulted in better performance than that of DT for fast ice classification. Visual comparison of the fast ice classification results with 250-m MODIS images for selected areas also revealed that RF outperformed DT. Ice velocity and IST were identified as the most contributing variables to classify fast ice. Spatiotemporal variations of fast ice in the East and West Antarctic were also examined using the time series of the fast ice maps produced by RF. The residence time of fast ice was much shorter in the West Antarctic than in the East.



## 2.2. Introduction

Much of the original Introduction and literature review of this chapter has been moved to Chapter 1 to avoid repetition.

While some studies were conducted to map and explore fast ice in the East Antarctic, few were performed over West Antarctica. Thus, this research aims at mapping and monitoring fast ice over the entire Antarctic area using time series satellite data. The objectives of this study are to (1) develop an automated model based on machine learning approaches for mapping fast ice through the synergistic use of time series optical and passive microwave data-sets for the entire Antarctic area, (2) explore accuracy patterns of the time series mapping results, (3) examine important variables for fast ice identification by model and how they affect the fast ice mapping results, (4) compare fast ice mapping results with the manually extracted fast ice edges from 250-m MODIS images for specific regions of interest, and (5) analyze the spatiotemporal variations of the Antarctic fast ice.

## 2.3. Data

### 2.3.1. Fast ice reference data

Fast ice maps of the East Antarctica from 2003 to 2008 produced by Fraser et al. (2010) were used as a reference data-set (Table 2. 1). The reference maps were generated from 20-day composites of MODIS imagery in which cloud-covered areas were removed using the MOD35 cloud mask products (Fraser et al., 2009; Fraser et al., 2010). Fast ice adjacent to the entire East Antarctic coastline was extracted using the MODIS composite images based on manual digitization with the help of AMSR-E sea ice concentration data (Fraser et al., 2010). The detailed procedures for deriving the reference data are described in Fraser et al. (2009) and Fraser et al. (2010).

Table 2. 1. Input variables and reference data information.

Satellite sensors	Variables	Spatial resolution (km)	Temporal interval	Units
AMSR-E	18GHz H/V	12	Daily	Kelvin (K)
	23GHz H/V			
	36GHz H/V			
	89GHz H/V			
	SIC			
MODIS	IST	4	Daily	Kelvin (K)
SSM/I	Ice velocity	25	Daily	cm/sec
Fraser reference data by Fraser et al. (2010)		1	20 days	

### 2.3.2. Passive microwave data

Brightness temperature and sea ice concentration data from AMSR-E were used in this study (Table 2. 1) (Cavalieri et al., 2014). Since fast ice has radiative properties distinctive from pack ice due to emissivity difference, the brightness temperature measured by passive microwave sensors such as SSM/I and AMSR-E can be used as powerful tools to identify sea ice types. SSM/I measures vertically and horizontally polarized brightness temperature at 19.35, 37.0, and 85.5 GHz and vertically polarized

brightness temperature only at 22.235 GHz. AMSR-E is composed of six frequencies: 6.925, 10.65, 18.7, 23.8, 36.5, and 89.0 GHz (Spreen et al., 2008; Comiso et al., 2003). All frequencies of the AMSR-E instrument measure both vertically and horizontally polarized brightness temperature, which enables a more detailed analysis of the physical properties of sea ice than the SSM/I-derived brightness temperature. The brightness temperature data measured at the 18.7, 23.8, 36.5, and 89.0 GHz channels of AMSR-E from 2003 to 2008 were used. Those channels are very effective for differentiating the radiative properties depending on sea ice types because of the dependency of polarization and spectral properties of the channels on emissivity differences (Cavalieri, 1996).

The passive microwave sensors have provided sea ice concentration every day within a few tens of kilometers. As fast ice forms over a wide area attached to the coastlines, sea ice concentration of the fast ice is about 100%. Over pack ice areas, passive microwave sensors observe brightness temperature from both ice and open water, which results in low sea ice concentration. AMSR-E daily sea ice concentration over the Antarctic from 2003 to 2008 was used. The grid spacing of AMSR-E sea ice concentration is 12.5 km which is finer than that of SSM/I sea ice concentration of 25 km. Sea ice velocity derived by SSM/I was also used to classify the ice types (Table 2. 1) (Fowler et al., 2013). The motion of fast ice is very small because it is fixed at the coastline or shallow seabed, while pack ice may move considerably in a short time period as the ice drifts freely by ocean current and wind.

### **2.3.3. Optical sensor data**

Fast ice and pack ice have different physical properties such as snow depth on ice surface, ice thickness, and surface wetness, which determine the IST (Hall et al., 2004). This means that the surface temperature of sea ice can be used as a variable to classify sea ice into fast ice and pack ice. The daily IST with 4-km spatial resolution measured by MODIS (MOD29E1D product) from 2003 to 2008 was used in this study (Table 2. 1) (Hall et al., 2006). Although MODIS IST is also provided with 1-km resolution, the aggregated 4-km IST data were used considering the spatial resolution of the other input variables, data processing time, and computational demand as the study area covers the entire Antarctic. Daily sea ice reflectance from the MOD29E1D product between 2003 and 2008 was used to define the extent of sea ice and to mask the open water area.

## 2.4. Methods

The original Methods for machine learning techniques of this chapter has been moved to Chapter 1 to avoid repetition.

Figure 2. 1 summarizes the process flow of the fast ice monitoring conducted in this study. A total of 11 input variables were used, including sea ice concentration and eight dual polarization frequency channels from AMSR-E, IST from MODIS, and ice velocity from SSM/I. Since the reference fast ice data were produced from the 20-day MODIS composite images (Fraser et al., 2010), the daily input variables were aggregated into the same 20-day composites using the statistical mean function. During the composite process of the MODIS IST data (MOD29E1D product), the sea ice by reflectance (i.e., sea ice vs. non-sea ice) variable contained in the MODIS IST product was also used to mask out non-sea ice pixels. Variables from the passive microwave sensors were all available for the whole Antarctic region over the study period (i.e., 2003–2008), whereas the IST data were not always available for some areas due to cloud cover during the composite period. Thus, the images <20 could be used in compositing IST data. The input variables used in this study have different spatial resolutions. All input variables and the fast ice reference data were resampled with 4-km resolution using bilinear spatial interpolation.

The sea ice type (i.e., fast ice vs. pack ice) was set to a dependent variable for binary classification. Since the fast ice reference data were only available for the East Antarctic, samples to train and validate machine learning-based classification models were extracted only from that region. Within the sea ice extent determined by AMSR-E sea ice concentration data, the area excluding the reference fast ice was considered as pack ice. One million samples (i.e., pixels, approximately 5.2% of the sea ice reference pixels) were selected from the sea ice reference data through stratified sampling as the ratio of 1:4 between fast ice and pack ice for the East Antarctic. Eighty percent of the samples by class were randomly extracted to train the machine learning-based models to classify the sea ice. The remaining 200,000 samples were used as the test data-set to validate the developed models.

Two rule-based machine learning approaches – DT and RF– were used to map fast ice in the Antarctic region. As both machine learning models provide relative variable importance, we examined the contribution of each input variable for fast ice mapping. The performance of DT and RF models were assessed based on the test data.

As the fast ice reference data were available only for the East Antarctic, additional visual assessment using relatively high-spatial-resolution MODIS images was conducted. The NSIDC-provided 250-m MODIS Antarctic ice shelf images were used to delineate the fast ice edges based on visual interpretation. Fast ice mapping results of the models were compared with the MODIS-derived

fast ice images over selected areas of interest in the Mertz and Abbot Ice Shelf regions in the East and West Antarctic, respectively. While the Mertz region documented relatively slow changing of fast ice distribution, the Abbot region showed rapid change based on the multiyear sea ice information (Massom et al., 2010; Worby et al., 2008).

The spatiotemporal patterns in the fast ice distribution were examined with the 6-year time series of the fast ice extent produced. Two frequency metrics of fast ice occurrence were calculated: the number of switches between occurrence and disappearance of fast ice (1) by pixel and (2) by applying weighted average depending on the number of composites during fast ice residence (Equation (3)).

$$\frac{\sum NC \times n}{\sum n} \quad (\text{Eq. 3})$$

where NC is the number of composites during fast ice residence, and n is the number of each NC found throughout the study period.

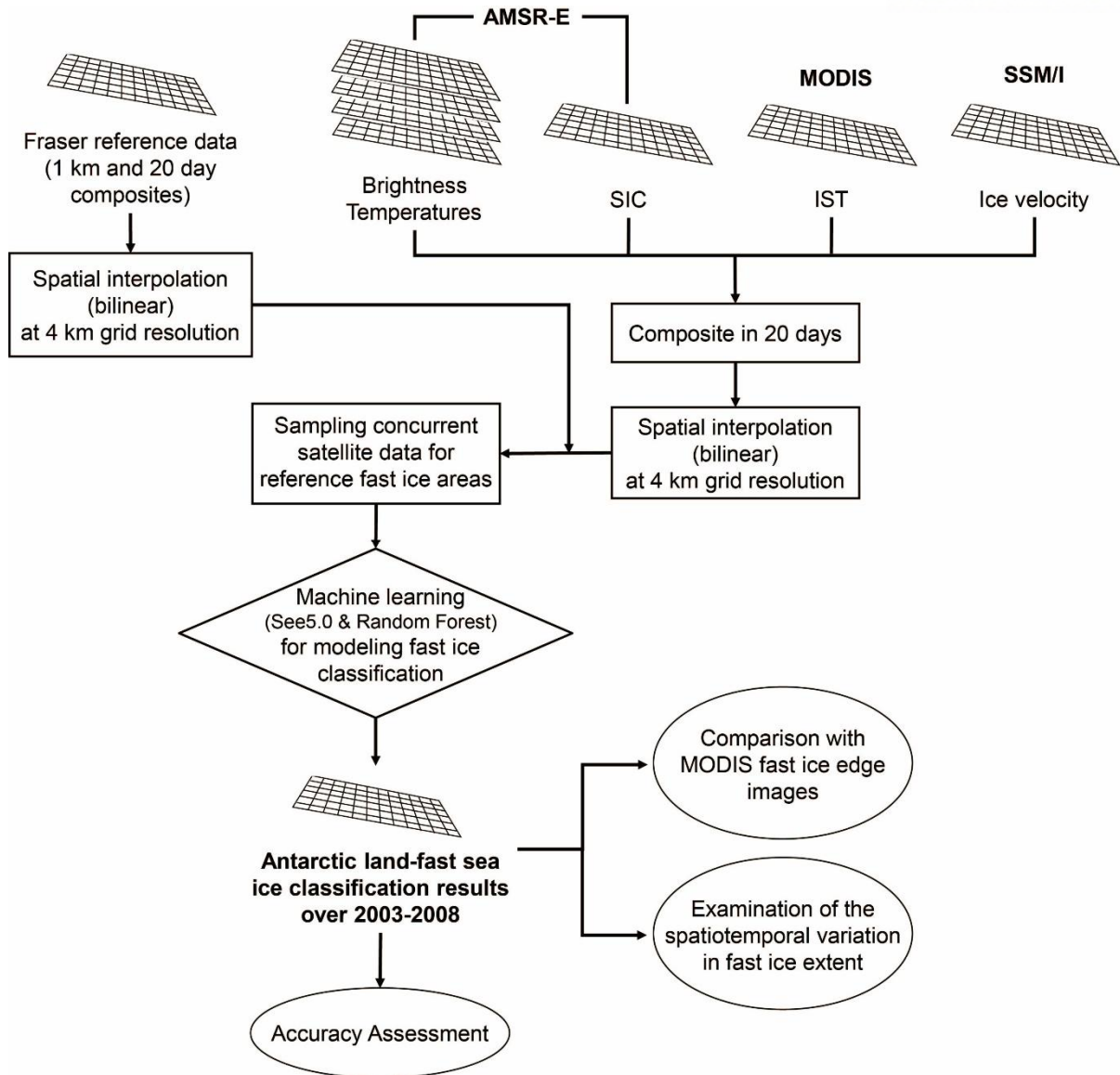


Figure 2. 1. The process flow of the research.

## 2.5. Results and discussion

### 2.5.1. Fast ice mapping model performance

The Antarctic fast ice mapping models developed by DT and RF were validated using the 200,000 test data-set. The DT and RF models produced similar overall accuracies of 93.09% and 94.77%, respectively (Table 2. 2-3). The RF model resulted in slightly higher performance of sea ice mapping, especially fast ice, than the DT model. The UA and PA of pack ice were higher than those of fast ice for both models. This is because the sample size of pack ice was much larger than that of fast ice, and the pack ice samples located far from the coast were easily distinguished from fast ice samples due to a relatively lower sea ice concentration. While the OA was similar between the two models, the Kappa coefficient of agreement resulted in a greater difference, ~6%, which showed the superiority of RF to DT.

The box plots of the PA and UA by model calculated using the reference fast ice data-set in the East Antarctic for the entire period (Fraser et al., 2009; Fraser et al., 2010) are shown in Figure 2. 2. In Austral winter (composites from 6 to 12), the UA and PA of fast ice were significantly low or uncalculated because MODIS IST was not available during the season. Both models produced similar PA and UA of fast ice through all composites. RF produced a bit higher accuracy than DT for identifying fast ice. For the first five composites, the PA was higher than the UA for both models, whereas the other composites showed a reversed trend. Both models produced very low PA near the winter season (i.e., composites 7 and 11) due to the limited availability of the MODIS IST data.

The relative importance of variables to fast ice mapping for both models is presented in Table 2. 4-5. Ice velocity and IST were the most contributing variables for fast ice classification regardless of the model used. The velocity of fast ice fixed to the shoreline or an ice shelf is close to 0 m/s (Mahoney et al., 2007; Mahoney et al., 2006), whereas pack ice can be easily moved by ocean currents and winds, and thus, it shows larger velocity than fast ice (Heil and Allison, 1999). It reveals that ice velocity can be used as a major variable for distinguishing fast ice from pack ice.

MODIS IST was identified as the second contributing variable for the fast ice mapping. The IST difference between fast ice and pack ice could be due to the subpixel effects in that fast ice typically has higher ice concentration while pack ice, especially far from the coast, has lower concentration affected by open water at  $4 \times 4$  km resolution (Hall et al., 2001). Open water has a higher surface temperature than sea ice (Hall et al., 2004). Fast ice typically forms at large size, while pack ice is distributed in patches, which results in a relatively higher IST for pack ice. However, the unexpected high IST values over fast ice regions are occasionally found where fast ice is formed for a small area, often occurring in Austral summer (Fraser et al., 2010). IST could also be different between the two

types of sea ice due to different physical characteristics. The surface temperature of sea ice depends on the physical properties of sea ice such as emissivity, thickness, and salinity (Hall et al., 2004; Maslanik and Key, 1993). Thick sea ice typically has a lower surface temperature than that of thin ice due to its lower emissivity in the infrared bands (Hall et al., 2004). Fast ice can thicken up to a few meters during the ice growing season (Heil et al., 1996), and thus, it would have a lower surface temperature than the drifting pack ice, which is typically less than 1 m thick (Worby et al., 2008).

While the ice velocity and IST were dominantly important compared to the other variables in the RF model, SIC showed a very high importance rating in the DT model following ice velocity and IST as SIC varies by sea ice type (Comiso et al., 2003). AMSR-E brightness temperatures at 36-GHz, vertically polarized channels and 18-GHz, both vertically and horizontally polarized channels also showed high importance ratings in the DT model, which implies that the brightness temperatures varied depending on sea ice types and ice thickness (Comiso et al., 1997). The three channels have been used to distinguish sea ice types (Comiso et al., 1997). For thick sea ice such as fast ice or multiyear ice, the brightness temperatures are very low ~190 K at 18-GHz H and 36-GHz V channels and 220 K at the 18-GHz V channel, while thin first-year ice such as pack ice and drift ice radiates much higher brightness temperatures at the three channels (~240 K at the 18 GHz H and 36 GHz V; and ~250 K at 18 GHz V) than thick sea ice (Comiso et al., 1997). In addition, as 89-GHz channels are less affected by snow or ice layers on sea ice than 36- and 18-GHz channels under clear sky conditions, 89-GHz channels can be used to differentiate the types of sea ice on which snow or ice accumulates (Markus and Cavalieri, 2000).

The contribution of the brightness temperatures measured at the other AMSR-E channels to the sea ice classification was relatively low, especially at 36 GHz H, showing the lowest importance for both models. This is because the 36-GHz H channel is sensitive to changes in atmospheric water vapor content instead of sea ice properties (Maslanik, 1992).

Table 2. 2. Accuracy assessment results for decision trees using the test data-set.

Classified as \ Reference	Reference			User's accuracy
	Fast ice	Pack ice	Sum	
Fast ice	32,274	6099	38,373	84.11%
Pack ice	7726	153,901	161,627	92.22%
Sum	40,000	160,000	200,000	
Producer's accuracy	80.69%	96.19%		
Overall accuracy			93.09%	



Kappa coefficient

78.06%

Table 2. 3. Accuracy assessment results for random forest using the test data-set.

Classified as \ Reference	Reference			User's accuracy
	Fast ice	Pack ice	Sum	
Fast ice	36,319	6773	43,092	84.28%
Pack ice	3681	153,227	156,908	97.65%
Sum	40,000	160,000	200,000	
Producer's accuracy	90.80%	95.77%		
Overall accuracy			94.77%	
Kappa coefficient			84.13%	

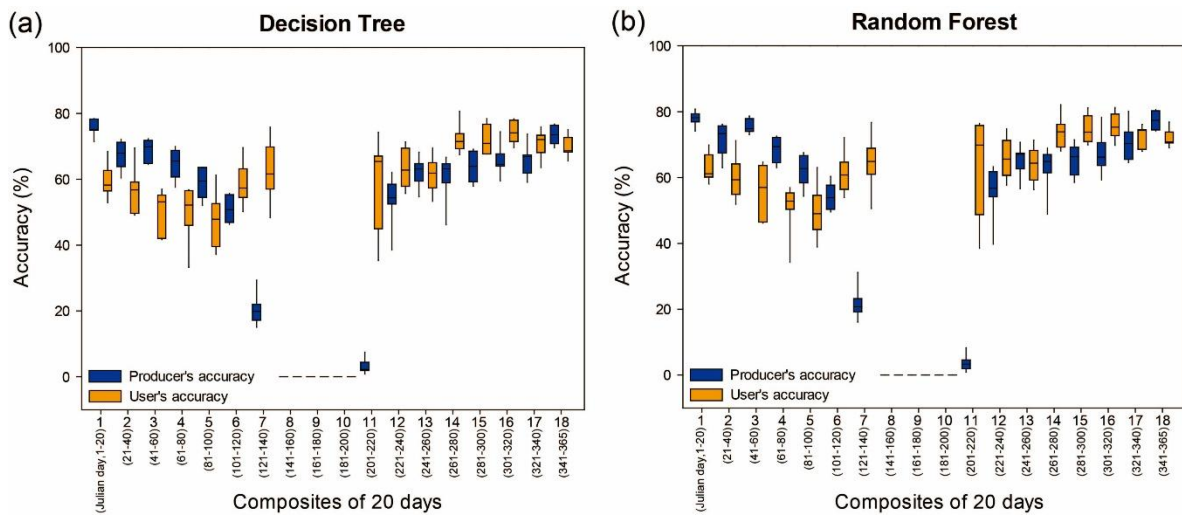


Figure 2. 2. Box plots of the producer's accuracy and user's accuracy for quantitative examination of the fast ice mapping results of (a) decision trees and (b) random forest. For full color versions of the figures in this paper, please see the online version.

Table 2. 4. Attribute usage of the decision trees model.

VEL	IST	SIC	18H	36V	18V	89V	89H	23V	23H	36H
100%	96%	92%	90%	87%	86%	80%	73%	62%	28%	7%

Table 2. 5. Mean decrease accuracy calculated using out-of-bag data when a variable was permuted in random forest. The greater the decrease in accuracy, the more contributing the variable was.

VEL	IST	23V	18H	89H	36V	23H	89V	18V	SIC	36H
607.3	354.8	160.8	160.5	147.0	136.8	111.6	111.4	105.7	103.3	99.53
4	9	2	0	4	4	1	0	2	5	

### 2.5.2. Comparison with MODIS images

Fast ice mapping results from the DT and RF models were compared with the fast ice area extracted from MODIS images with 250-m spatial resolution (band 2) over the Mertz Ice Shelf region in the East Antarctic and Abbot Ice Shelf in the West Antarctic with different periods considering the variability of fast ice (Figure 2. 3-4). When the fast ice near Mertz Ice Shelf was relatively stable during 13 days of the MODIS images (Figure 2. 3a), the RF model detected fast ice better than DT compared with the actual fast ice areas (Figure 2. 3c and 3e). This might be because the RF model used the ice velocity and IST much more significantly than DT to classify ice types compared to the other variables, such as the brightness temperatures at 18 GHz H and V and 36 GHz V. For example, wide ice floes located to the right of the fast ice appeared to be dropped out of the fast ice, and thus, they had reflectivity and morphology similar to the fast ice. Therefore, the microwave radiation properties, i.e., the brightness temperature, of the ice floes were similar to those of the fast ice (not shown). It resulted in misclassification between the fast ice and ice floes when the DT model with high importance of the brightness temperatures at 18 GHz H and V and at 36 GHz V was used. Since the ice floes and fast ice had different ice velocity and IST values, RF was able to identify the fast ice in the region relatively better than DT.

For the relatively stable fast ice during 8 days in Abbot Glacier in the West Antarctica (Figure 2. 3b), both the DT (Figure 2. 3d) and RF (Figure 2. 3f) models mapped much smaller fast ice areas than the actual fast ice areas. The low spatial resolution of the passive microwave-derived variables (12–25 km) could be a major reason as the fast ice was very narrowly attached to the shoreline. In addition, MODIS IST with relatively higher spatial resolution was not always available for the period of the corresponding composite due to heavy clouds (i.e., ~25% available on average), which resulted in very limited examination of the temporal variation of the fast ice areas.

Previous studies reported that the 20-day compositing period well represented the variation, growth, and breakup of fast ice, and thus, it is enough to map fast ice areas in the polar region (Fraser et al., 2010; Mahoney et al., 2006). However, substantial changes in the fast ice areas in 20 days were often observed in both the East and West Antarctic from the MODIS images (Figure 2. 4). This implies that the 20-day composite interval might not be sufficient to represent the variation of fast ice, especially where it rapidly changes over a short period of time. For such areas, fast ice should be monitored with

compositing period less than 20 days. For the rapidly changing period around Mertz (Figure 2. 4a) and Abbot Ice Shelf (Figure 2. 4b), the performance of the RF (Figure 2. 4e and 4f) model was slightly better than DT (Figure 2. 4c and 4d) through the visual validation of the fast ice mapping results with the high-resolution MODIS images. This also corresponds to the accuracy assessment results of the classification models (Table 2. 2-3).

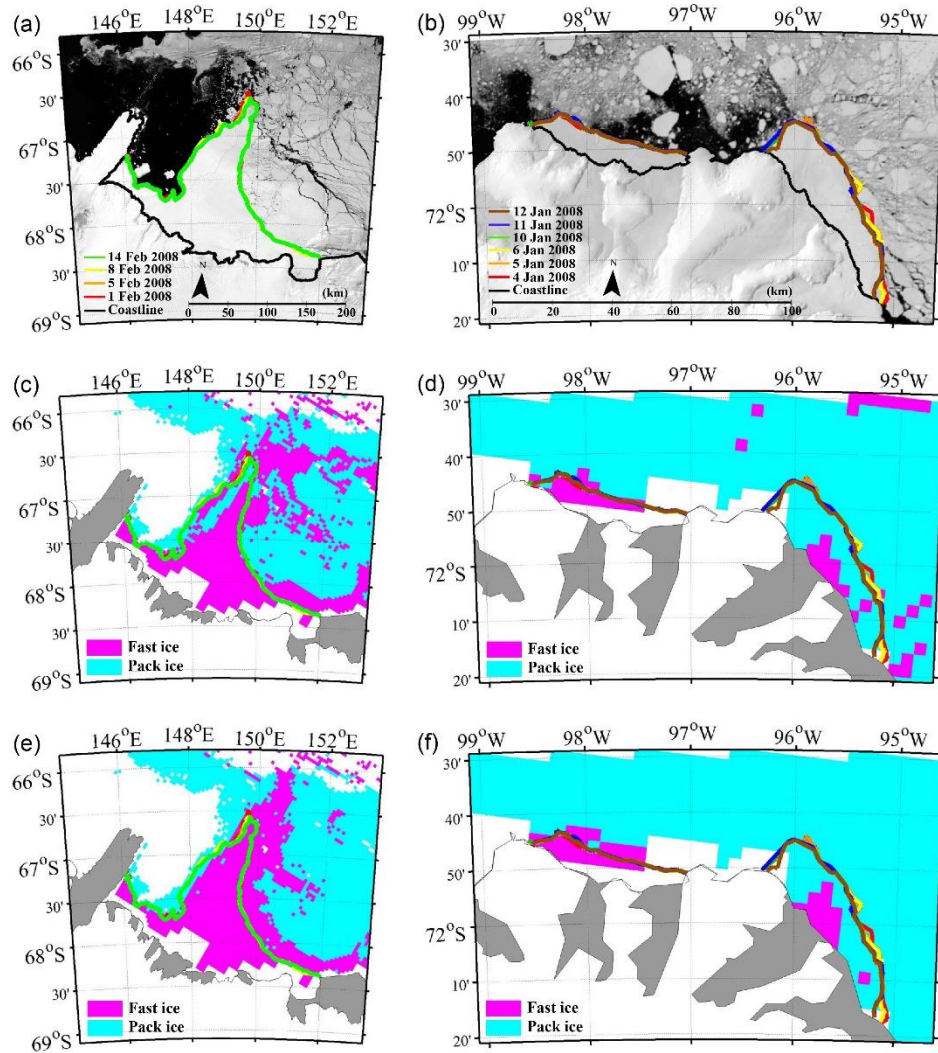


Figure 2. 3. Comparison of fast ice mapping results by model with the 250-m MODIS images during the periods of relatively stable fast ice around (a) Mertz and (b) Abbot Ice Shelf in the East and West Antarctica, respectively. The lines in (a) and (b) indicate fast ice edges delineated from the MODIS images based on visual interpretation. Decision tree results are shown in (c) and (d), while random forest results are in (e) and (f). MODIS images with the maximum fast ice cover were used as background images in (a) and (b).

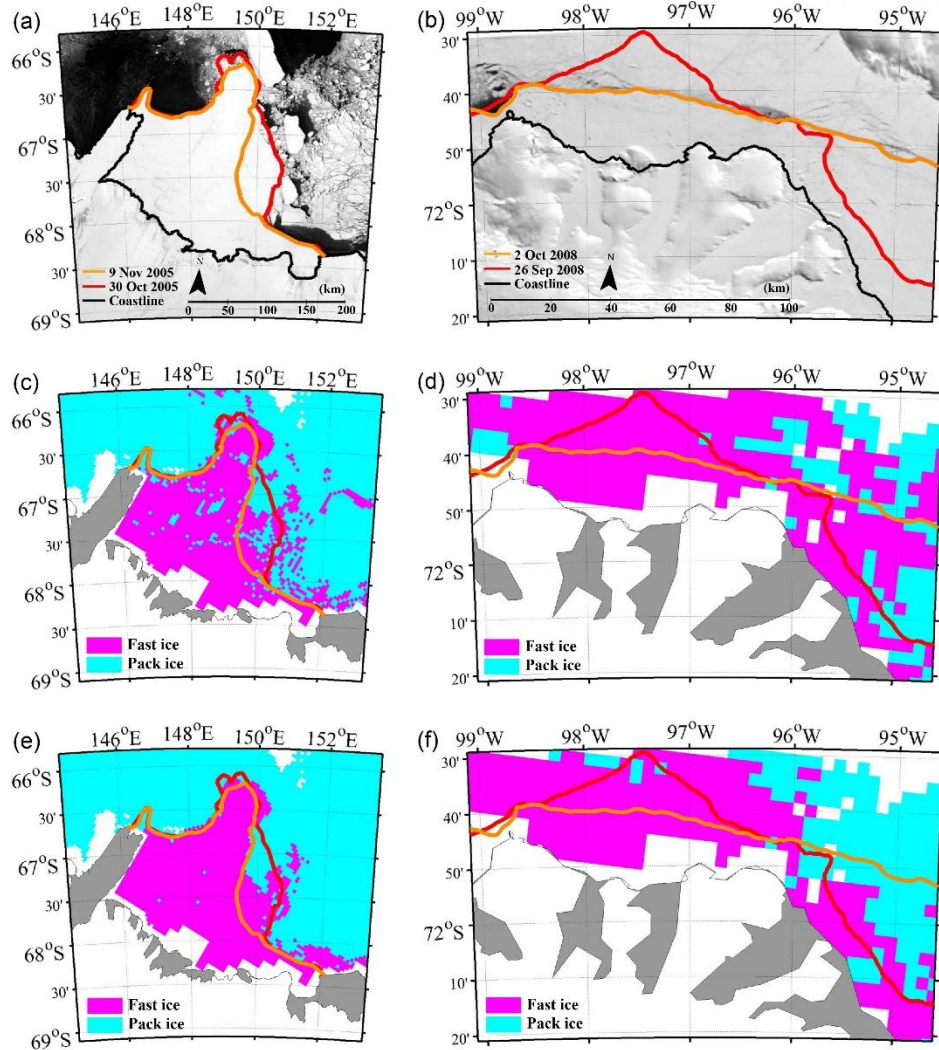


Figure 2. 4. Comparison of fast ice mapping results by model with the 250-m MODIS images during the periods of rapidly changing fast ice around (a) Mertz and (b) Abbot Ice Shelf in the East and West Antarctica, respectively. The lines in (a) and (b) indicate fast ice edges delineated from the MODIS images based on visual interpretation. Decision tree results are shown in (c) and (d), while random forest results are in (e) and (f). MODIS images with the maximum fast ice cover were used as background images in (a) and (b).

### 2.5.3. Spatiotemporal variation of fast ice in the East and West Antarctic

As the RF model produced better fast ice classification results than the DT model, the RF-derived maps were used to examine the spatiotemporal variation of fast ice. Fast ice in the entire Antarctic Ocean was mapped by composite period (i.e., 20 days) from 2003 to 2008. Although MODIS IST was identified as one of the most important variables to detect fast ice, it has a major drawback, which is its limited availability. Due to the lack of MODIS IST data during the Australian winter season, fast ice mapping results could not be obtained for the sixth (101–120 Julian days) to twelfth (221–240 Julian days) composite periods. Figure 2. 5 shows the distribution maps of fast ice produced by the RF model



for two composites in 2003. Hatched areas in Figure 2. 5 represent that IST was not available during the composite period, which resulted in no fast ice classified in the areas. The limited spatial coverage of IST could increase uncertainty of fast ice distribution in the Antarctic. As shown in Figure 2. 6, the spatial discontinuity of IST data was larger in the West Antarctica than in the East throughout the entire composite period. While the availability of IST is higher in the East Antarctica than in the West, some regions in the East Antarctica also had no available IST data for a certain time of period.

The time series of fast ice extent is depicted for the East and West Antarctica between 2003 and 2008 in Figure 2. 7. While the temporal variation of the fast ice areas in the West Antarctica appeared higher than that in the East (with standard deviations of 122,457 km<sup>2</sup> in the West Antarctica and 69,158 km<sup>2</sup> in the East), it should be noted that the limited availability of IST data might increase temporal uncertainty in the fast ice distribution especially around Weddell Sea and Ross Sea in the West Antarctica. Fraser et al. (2012) reported that the fast ice extent maximum was found around September and the minimum around March in the East Antarctica. Our results for the East Antarctica also showed a similar trend (Figure 2. 7). However, such a pattern was not found for the West Antarctica, possibly due to the data void problem caused by MODIS IST data. Unlike the East Antarctica, many data voids occurred along the coast especially in the Weddell Sea and Ross Sea in the West Antarctica, which significantly increased the uncertainty of the fast ice distribution in those regions. No training data from the West Antarctica were used in the classification models, which possibly increased the false alarm or false negatives of the fast ice detection to lead to the increase in the uncertainty of the fast ice distribution. Consequently, the temporal (seasonal and annual) variation of fast ice distribution in the West Antarctica should deserve further research.

Figure 2. 8 shows the distribution of the frequency of fast ice residence using simple counting of the switches (i.e., occurrence and disappearance) and the weighted average approach (Equation (3)). In order to mitigate the data void problem, it was excluded in the frequency calculation when a pixel in a composite had no data. High values of frequency for the simple counting approach indicated that the advance and retreat of fast ice frequently occurred during the study period. While the temporal variation of the fast ice based on the simple counting approach was generally high in the edge of fast ice all over the East Antarctica, it was only high for specific areas such as Weddell and Amundsen Sea in the West Antarctica (Figure 2. 8a). When the weighted average approach was used, high values meant that the fast ice residence time was relatively long, while low values indicated that fast ice only existed for a short period of time (Figure 2. 8b). While the weighted average of the fast ice residence was very low in the West Antarctica, it was relatively high in the East Antarctica, which corresponds to more gradual change of fast ice distribution in the East Antarctic region (Figure 2. 7).

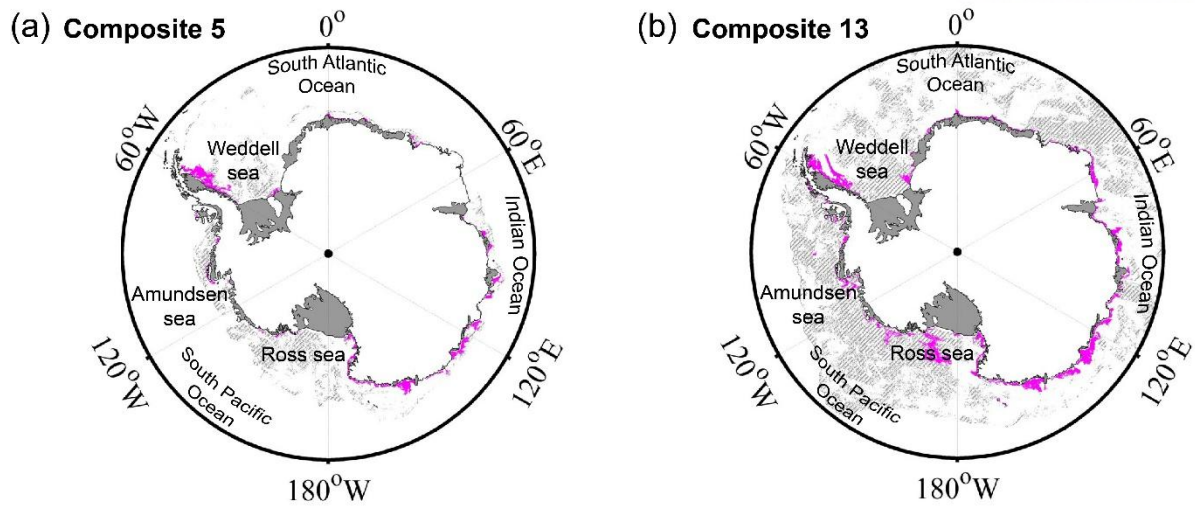


Figure 2. 5. Fast ice maps using random forest in 2003 for (a) composite 5 (81 – 100 Julian days) and (b) composite 13 (241 – 260 Julian days). Magenta areas represent fast ice in the Antarctic, and hatched areas with gray color indicate that MODIS IST was not available for the composite.

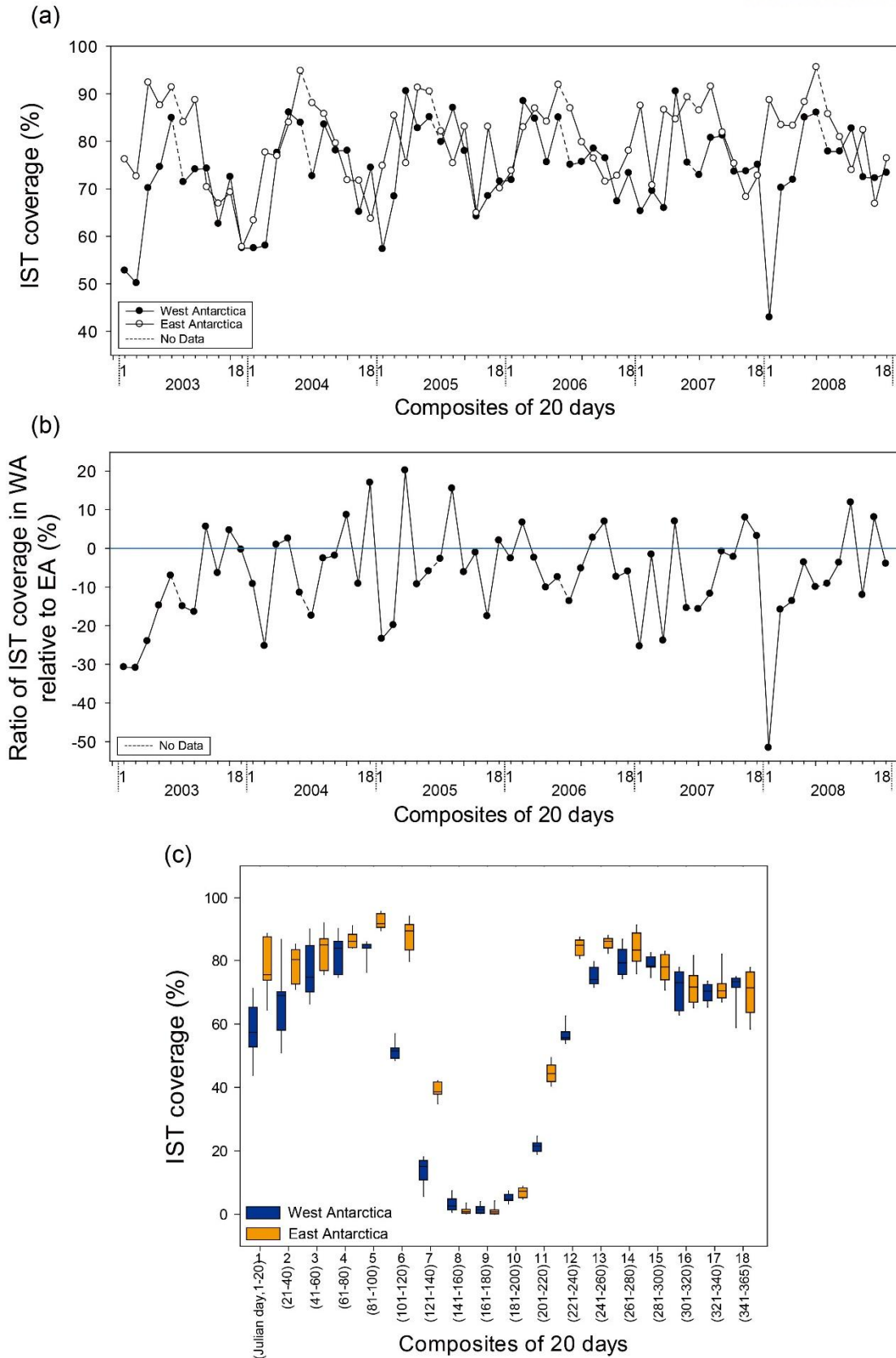


Figure 2. 6. (a) Temporal variation of the availability of MODIS IST data in the East and West Antarctic regions. (b) The ratio of the IST coverage in the West Antarctic (WA) relative to the East Antarctic (EA) in percentage. (c) Box plot of the IST coverage in percentage by composite.

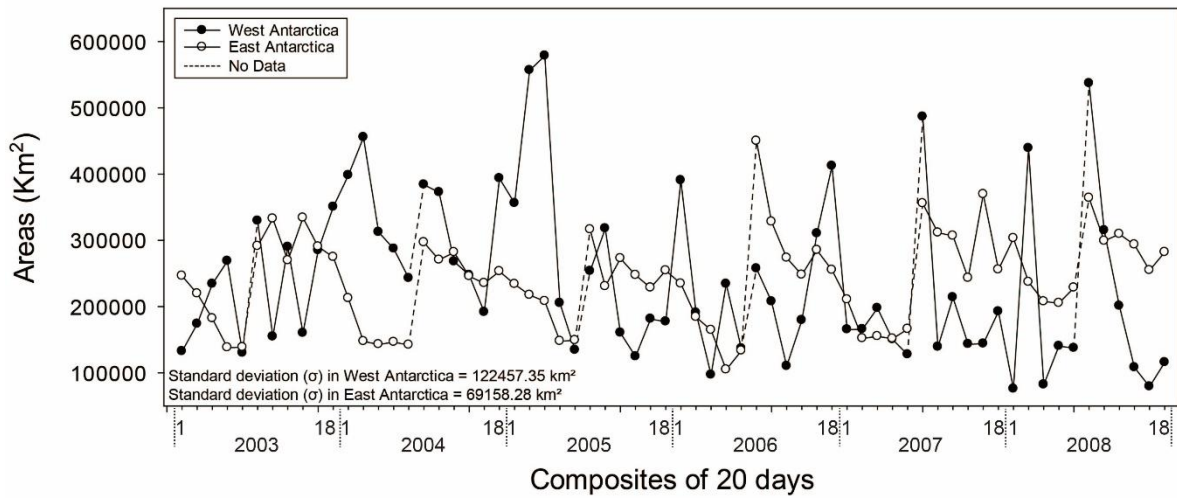


Figure 2. 7. Temporal variation of fast ice areas in the East and West Antarctic. Due to the lack of the input data during the Australian winter season, composites 6 – 12 for each year were not available.

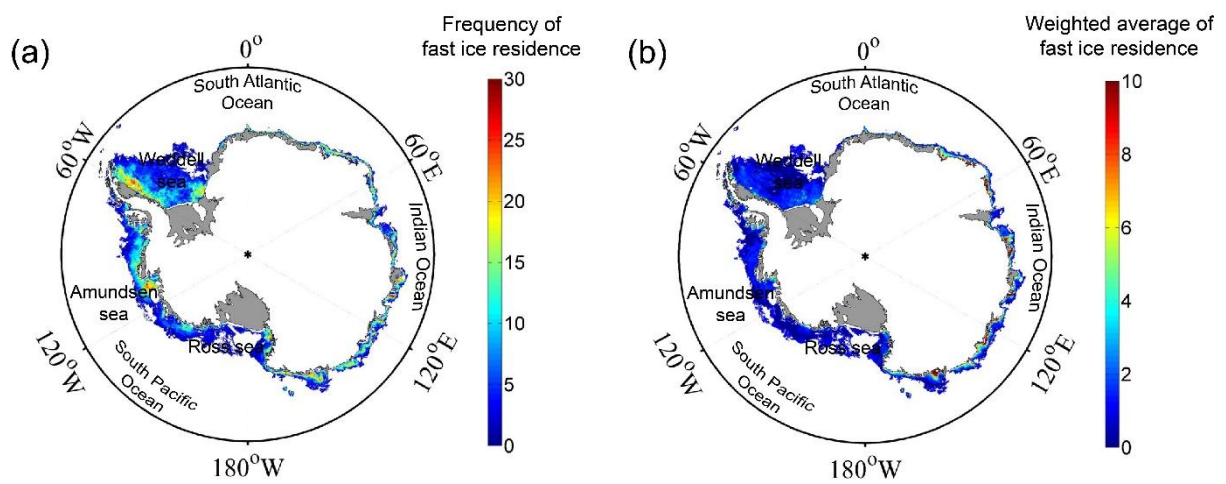


Figure 2. 8. Temporal variation of fast ice in the Antarctic using a) the simple counting approach and b) the weighted average approach.



## 2.6. Conclusions

In this study, fast ice in the East and West Antarctic was mapped using multisensor data and machine learning techniques – DT and RF – during the period from 2003 to 2008. RF produced better performance than DT for fast ice mapping based on the accuracy assessment and visual interpretation of the classification maps in conjunction with 250-m MODIS images. Ice velocity and IST were identified as the most contributing variables to classify fast ice regardless of the approach used. Based on the time series of the fast ice maps produced by RF, the spatiotemporal variations of fast ice were examined over the entire Antarctic. While the temporal pattern of fast ice extent for the East Antarctica agreed with the literature, no clear pattern was found for the West Antarctica due to the data void problem, which resulted in considerable uncertainty of the fast ice distribution. Fast ice residence time was relatively long in the East Antarctica, which indicates gradual changes in advance and retreat of fast ice. However, fast ice residence time was very short in the West Antarctica partially due to the no-data pixels from MODIS IST data.

Since some areas had a high variation of fast ice for a short period of time, compositing of input variables with a period of less than 20 days is necessary to accurately monitor fast ice in the Antarctic. However, since MODIS IST, one of the most contributing variables, is heavily influenced by clouds, the number of no-data pixels inevitably increases when compositing IST with a small number of days (e.g., 10 days). Thus, spatial and temporal interpolation might be necessary to solve the data void problem when using a small number of days for compositing of MODIS IST. Future research includes (1) incorporating additional variables such as CryoSat-2-derived sea ice thickness for fast ice mapping to improve classification accuracy and (2) linking time series of fast ice distribution to climate change indicators to better understand the Antarctic climate system and its relation to other regional climate systems.

## Chapter 3

# Object-based landfast sea ice classification over West Antarctica using synthetic aperture radar of ALOS-1 PALSAR

### 3.1. Abstract

Fast ice is an important feature prevalent around the Antarctic coast, which is associated with on-going climate change and energy interaction with the atmosphere and ocean. Previous studies on detecting fast ice regions have focused on using optical sensor data with a limitation of cloud contamination over the East Antarctic; a relatively less heterogeneous region compared to the West Antarctic. This study proposes a method for detection of the West Antarctic fast ice using ALOS PALSAR data with a short time interval (5-days). The algorithm combines image segmentation, image correlation analysis, and machine learning techniques (i.e., RF, ERT, and LR). It is based on the assumption that a highly correlated region using two consecutive SAR images with a 5 day time interval is stable with little movement over time and is considered to be fast ice regions. The proposed object-based approach was well applied to high-resolution SAR images for deriving spatially homogeneous fast ice regions. The image segmentation results with the optimized parameters show a distinct difference in backscattering between fast ice and non-fast ice objects over time. Correlation and standard deviation of scattering were found to be significantly contributing variables for fast ice detection. The developed model was applied to various fast ice areas in the West Antarctic ocean sectors for validation. The validation results suggest that the proposed algorithm can show stable and superior performance for detecting fast ice regions under various environmental conditions.

### 3.2. Introduction

Much of the original Introduction and literature review of this chapter has been moved to Chapter 1 to avoid repetition.

In this paper, we propose a new method that combines image segmentation, image correlation analysis, and machine learning techniques for detecting fast ice regions over West Antarctica. Specifically, this study develops an algorithm for object-based fast ice detection that adopts object correlation image analysis using bi-temporal L-band SAR images with a short time interval (5 days). Object-based classification has the potential to achieve accurate feature extraction since pixel-based classification might be inappropriate with SAR images of high spatial resolution due to the difficulty of interpretation resulting from speckle noise and high spatial heterogeneity. As fast ice regions are recognized as being spatially continuous with little change, object-based analysis is desirable for the detection of fast ice areas. Based on the segmented SAR composite images, object correlation image analysis was conducted based on the characteristics of motionless and stationary fast ice regions, which result in highly correlated fast ice regions over time. Machine learning techniques including RF, ERT, and LR were applied to the segmented fast ice image pairs to develop fast ice classification models. Model validation was conducted in various fast ice regions in ocean sectors of West Antarctica to demonstrate the applicability of the proposed approach.

### 3.3. Data and Methods

#### 3.3.1. Process description and study area

The whole data processing flow of the proposed approach in this study is illustrated in Figure 3. 1. First of all, SAR images, used as main data, are preprocessed and then composited with a pair of images (section 3.3.2), then image segmentation is performed for the preprocessed composite images (section 3.3.3). For each object of segmented images, input variables for fast ice and non-fast ice regions are extracted including statistical and contextual variables (i.e. object correlation images). To construct fast ice and non-fast ice reference regions, time series of SAR images in a certain time interval are used (section 3.3.4). The constructed datasets are applied to machine learning approaches to develop fast ice classification models (section 3.3.5). Figure 3. 2 shows study areas with SAR images containing fast ice regions over four ocean sectors including Weddell Sea, Bellingshausen Sea, Amundsen Sea, and Ross Sea in West Antarctica. From each ocean sector, training and test data to construct fast ice classification models and separate validation datasets to evaluate the models are extracted.

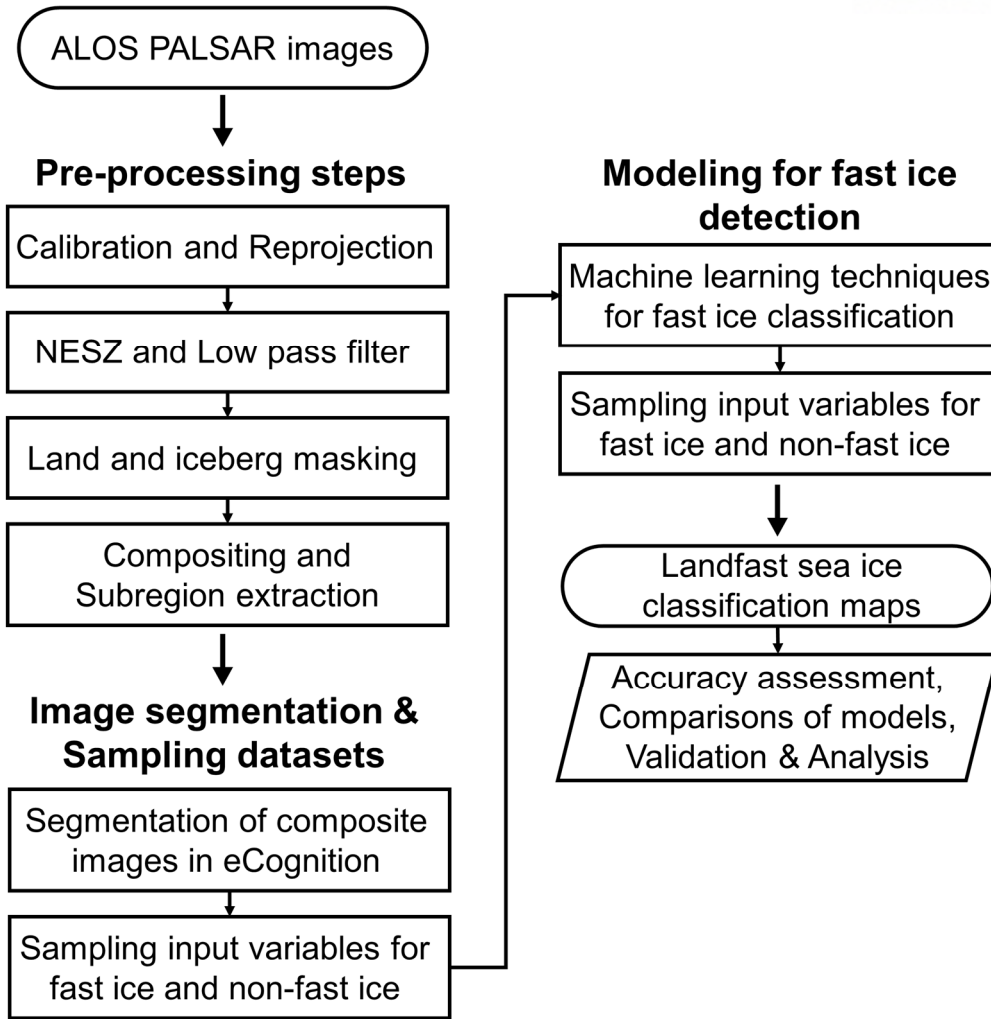


Figure 3. 1. Data process flow chart of the proposed approach in this study.

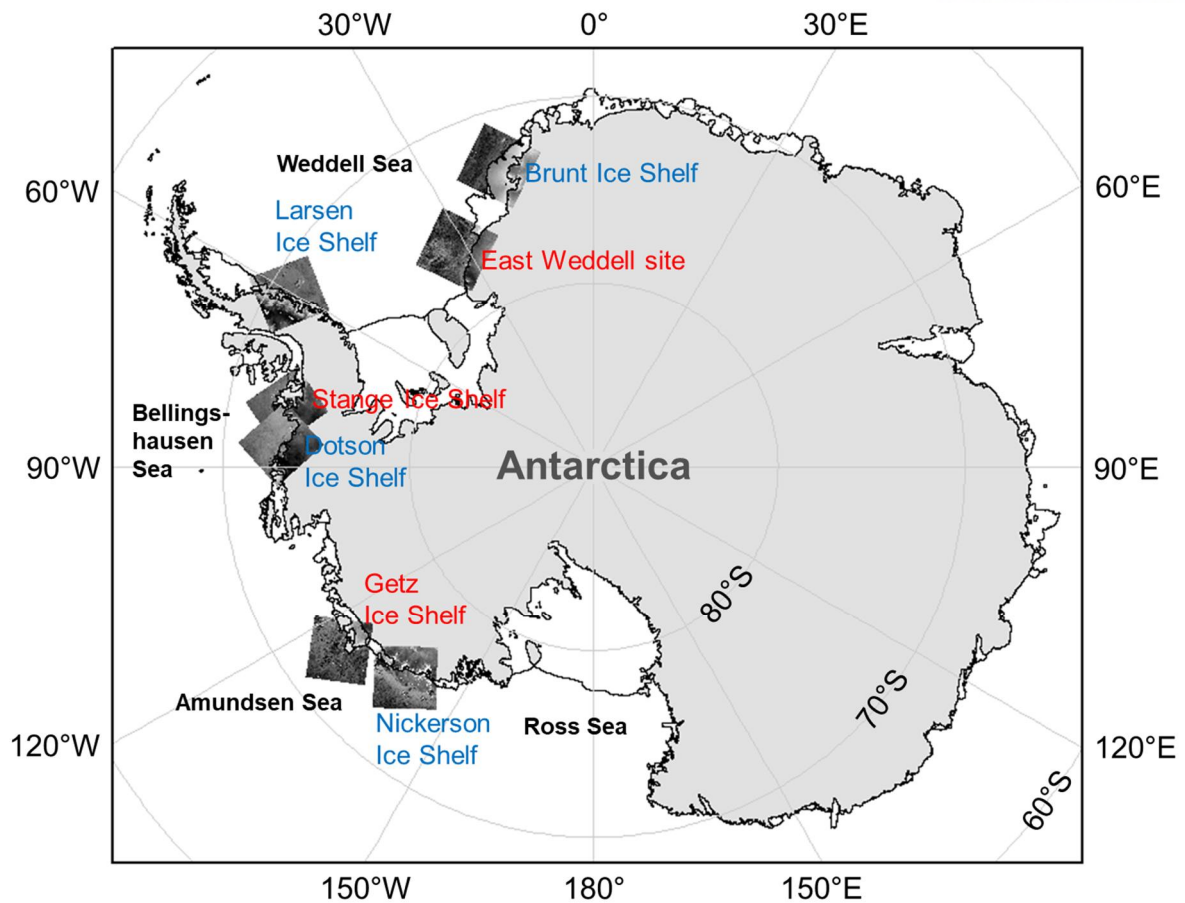


Figure 3. 2. Map of study area including landfast sea ice regions over West Antarctica with ALOS PALSAR images over the Weddell Sea, Bellingshausen Sea, Amundsen Seas, and Ross Sea sectors. Regions (red letters) in Weddell Sea were used for constructing training and test datasets and the other regions (blue letters) for validation.

### 3.3.2. ALOS PALSAR data

Level 1.5 geo-referenced SAR images from ALOS PALSAR were used as main data for the detection of fast ice in this study. PALSAR is an active microwave sensor using L-band frequency. It has a ScanSAR mode that allows us to observe the surface with hundreds of kilometers in width. PALSAR images are distributed free of charge by the ASF to public users. The detailed information of SAR image pairs selected for this study is shown in Table 3. 1 with the names of each site, dates of images, incidence angle, and usage. All the SAR images are wide-swath ScanSAR mode data with a swath width of 350 km at 5 scan operations, HH polarization, descending flight pass direction, and the range and azimuth pixel size of 100 m with a time interval of 5 days. Although ALOS PALSAR orbit has a repetition period of 44 days, pairs of images in a short time interval can be obtained for areas where fast ice areas overlap in polar regions. This approach is intended for use with high temporal resolution images even from polar orbiting satellite sensors with long repetition cycles. The model

developed in this study has the benefit of being able to interpret short-term fast ice deformation events occurring on a time scale of several days.

The ScanSAR mode has a wide range of incidence angles (18-43° for ALOS PALSAR). An incidence angle is defined as the angle between the incoming radar vector and the vector perpendicular to the ground. Therefore, incidence angle correction is needed since backscattering coefficients may change in the same sea ice type as the incidence angle changes (Zakhvatkina et al., 2013; Lang et al., 2016). However, in this study, incidence angle correction was not performed for several reasons. First, accurate reference data on sea ice types should be provided. However, fine resolution (~100 m) reference data were not available in this study, while existing reference data such as the Antarctic ice charts from the U.S. National Ice Center Naval Ice Center (<http://www.natice.noaa.gov/>) have relatively very coarse resolution, which implies that various sea ice types may be mixed in a class patch. In addition, when multiple classes exist in a pixel, incidence angle correction may not work well for all sea ice types, which eventually may not preserve the detailed texture and natural signal variability in radar data. The L-band SAR data used in this study has larger wavelengths than the other bands, so it is relatively less sensitive to small changes in sea ice surface (Dierking and Busche, 2006; Meyer et al., 2011; Dammann et al., 2016). In addition, as object-based input variables are used through image segmentation, the dependence of backscattering on incidence angles can be significantly reduced when compared to pixel-based input variables, which compensates for the uncertainty due to the incidence angle effect. In this study, the capability of the proposed approach to generate high-quality fast ice detection over West Antarctica is demonstrated in a variety of regions and dates, without incidence angle correction and post-processing (more in the discussion section).

Training, test, and validation datasets were extracted from all ocean sectors, the usage of which is explained in section 3.3.2. A total of 7 image pairs were selected over 1) Weddell Sea sector including East Weddell site, Brunt Ice Shelf, and Larsen Ice Shelf, 2) Bellingshausen Sea sector including Stange Ice Shelf and Dotson Ice Shelf, and 3) Amundsen Sea sector including Getz Ice Shelf and Nickerson Ice Shelf. The image data were collected from July to August in 2007 and from October to November in 2010. The selected images were preprocessed in the MapReady software (version 3.1.24) developed by the ASF. First, the amplitude of the reflected backscatter in SAR images was converted into a radiometrically calibrated power image in order to use SAR data in a quantitative manner. The level 1.5 geo-referenced SAR images with backscatter values were calibrated into sigma-0 (nought) in power scale out of radar backscatter coefficients ( $\sigma_0$ ,  $\gamma_0$ ,  $\beta_0$ ), which intends to use the calibrated values that refer to the ground. Then, the values were scaled into decibel (dB) values by applying a logarithmic function ( $10 \cdot \log_{10}(\text{calibrated values})$ ). SAR geometry was transformed into polar stereographic map projection with a bilinear resampling method and a specified pixel size of 100 m. The NESZ was -25 dB, below which pixel values were discarded, and a low pass filter was applied to the preprocessed

images. After all preprocessing steps were conducted, each image in an image pair was masked for the overlaid regions and then composited for image segmentation in the following section 3.3.3. A single image is not sufficient to identify fast ice area because fast ice maintains spatial consistency over a period of time. Therefore, by using two consecutive SAR images with a specific time interval, it is possible to determine fast ice regions as stable or unchanged ice parts over time. By compositing SAR images at a certain time interval, two consecutive SAR images were used for fast ice detection through image segmentation and object-based classification.

Table 3. 1. The information of ALOS PALSAR image sets. All the image pairs have time interval of 5 days.

Sector	Site	Date (for a pair of images)	Incidence angle	Usage
Weddell Sea	East Weddell site	8 Aug. 2007 13 Aug. 2007	34.112° 34.107°	Training and Test
	Brunt Ice Shelf	8 Aug. 2007 13 Aug. 2007	34.078° 34.090°	Validation
	Larsen Ice Shelf	20 Aug. 2007 25 Aug. 2007	34.106° 34.086°	Validation
Bellingshausen Sea	Stange Ice Shelf	7 Oct. 2010 12 Oct. 2010	34.099° 34.101°	Training and Test
	Dotson Ice Shelf	13 Nov. 2010 18 Nov. 2010	34.103 34.103	Validation
Amundsen Sea	Getz Ice Shelf	31 Oct. 2010 5 Nov. 2010	34.091° 34.092°	Training and Test
	Nickerson Ice Shelf	26 Jul. 2007 31 Jul. 2007	34.095° 33.979°	Validation

### 3.3.3. Image segmentation and explanatory variables

Image segmentation was implemented in eCognition software (Version 8.7.2) with the SAR composite images. Image segmentation is suitable for SAR data with high spatial heterogeneity. This is because classification problems caused by local outliers and noise can be mitigated by grouping pixels with similar characteristics. The multiresolution segmentation algorithm in eCognition was used, which is a bottom-up segmentation method that minimizes the heterogeneity of image objects and maximizes homogeneity by producing optimized segmentation results. Segmentation starts with single pixels and repeatedly merges them into larger groups by using certain user-defined criteria for homogeneity (Belgiu and Drăguț, 2014; Witharana and Civco, 2014). The segmentation procedure iterates until each image object finds the best neighbor to merge with based on the homogeneity criteria. The homogeneity criteria are defined for color, smoothness, and compactness. A scale parameter limits the maximum allowable criteria of the homogeneity, influencing the size of resultant objects. In homogeneous images, objects will be larger than those in heterogeneous images. Shape and compactness parameters are used for the relative homogeneity criteria. The shape criterion affects the relationship between shape and



color (color = 1 – shape). It determines the degree of the contribution of spectral values of images for object generation. In addition to the spectral homogeneity-related criterion, the degree of compactness among objects is determined by the compactness parameter. It is calculated as the ratio of the perimeter of an object and its area. The more compact an object is, the smaller its border length is (i.e. pixels in an object are closer to the circle boundary). It is useful for images where compact and non-compact objects are not clearly distinguishable due to weak spectral contrast (Yan et al., 2006). The compactness criterion can enhance the quality of segmentation for strongly textured data such as radar backscattering images with highly fractured objects (Lucieer and Lamarche, 2011). In this study, various combinations of scale, shape, and compactness parameters were tested, and an optimum combination was determined based on visual inspection of resultant objects.

As shown in Table 3. 2, a total of 5 input variables—contextual variables of OCI analysis (i.e., correlation, slope, and intercept) and statistical variables such as mean and STD—were extracted from objects of the segmented composite images. The contextual variables were calculated with pixels within each object of the composite images. The magnitude and direction of changes of spectral pixel values in an object of the composite images are used for the OCI analysis (Im and Jensen, 2005; Im et al., 2008). If there is little or no change between the two dates of images, correlation coefficients of pixel values from two dates are assumed to be high. Otherwise, correlation coefficients are generally low or intermediate when changes significantly or moderately occur. The other information in the OCI analysis are slope and intercept, which can be useful in detecting changes when correlation coefficients are high. The correlation, slope, and intercept images are computed as the following equations (1)-(3), respectively (Im et al., 2008).

$$\frac{N \times B \times \sum_{i=1}^B ZD1D2_i - (\sum_{i=1}^B ZD1_i \times \sum_{i=1}^B ZD2_i)}{\sqrt{(N \times B \times \sum_{i=1}^B ZD1D1_i - (\sum_{i=1}^B ZD1_i)^2) \times (N \times B \times \sum_{i=1}^B ZD2D2_i - (\sum_{i=1}^B ZD2_i)^2)}} \quad (1)$$

$$\frac{N \times B \times \sum_{i=1}^B ZD1D2_i - (\sum_{i=1}^B ZD1_i \times \sum_{i=1}^B ZD2_i)}{N \times B \times \sum_{i=1}^B ZD1D1_i - (\sum_{i=1}^B ZD1_i)^2} \quad (2)$$

$$\frac{\sum_{i=1}^B ZD2_i - Slp \times \sum_{i=1}^B ZD1_i}{N \times B} \quad (3)$$

where N is the image with the number of pixels for each object from the image segmentation, B is the number of input bands, which is 2 (i.e. consecutive images of two dates) in this study, ZD1i and ZD2i are the images from date 1 and 2 for each channel i zonally summed based on the objects, ZD1D1i, ZD1D2i, and ZD2D2i are the images multiplied by each date by itself and date 1 and 2 for each channel i and zonally summed based on the objects, and Slp indicates the slope image obtained by the equation 2.

The mean variable is certainly helpful in distinguishing between sea ice and open water. Open

water typically has a lower backscatter coefficient under calm wind conditions than sea ice due to the rough surface of sea ice (Dammann et al., 2016). As non-fast ice regions contain deformed sea ice as opposed to fast ice regions by experiencing mechanical deformation by winds, ocean current, and typhoons (Dammann et al., 2016), a rougher surface of non-fast ice regions exhibits higher backscattered signals than undeformed fast ice regions. However, in an image pair with a time gap of a few days, backscattering values of both sea ice and open water are mixed in an object of the segmented composite image according to the presence of sea ice in non-fast ice regions. The STD variable can be used to discriminate fast ice from non-fast ice regions. No significant changes in fast ice regions between two dates enable spectral values more relatively intact than in floating pack ice regions. The STD of backscattering values may increase in pack ice regions due to a wide range of pixel value changes between two dates compared to immobile fast ice regions.

Table 3. 2. Input variable information.

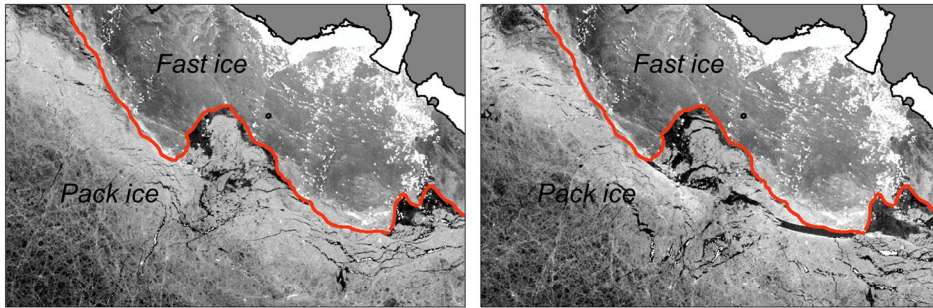
Type	Input Features
Contextual variables	Correlation
	Slope
	Intercept
Statistical variables	Mean of composite imagery including layer 1 (earlier date) and 2 (later date)
	Standard deviation of composite imagery

### 3.3.4. Construction of reference for landfast sea ice and non-landfast sea ice

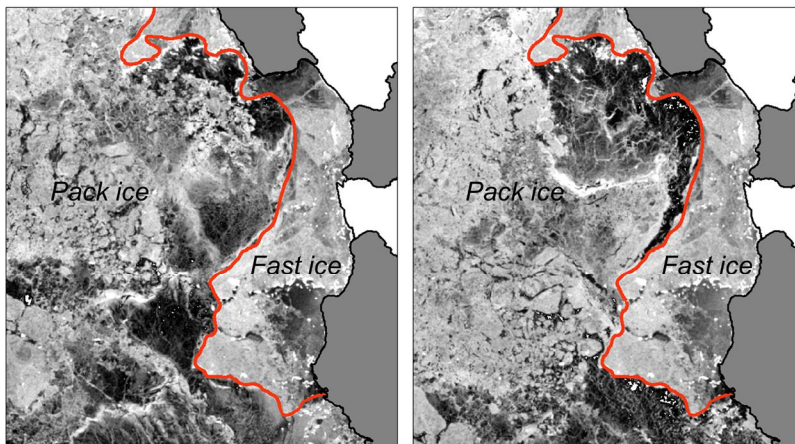
Reference regions for fast ice and non-fast ice were determined based on visual interpretation of the preprocessed SAR composite images in a 5-day time interval. Mahoney et al. (2007) applied a fast ice edge delineation technique with three mosaics of SAR images to define fast ice edges with a time interval of 20 days. Seaward fast ice edges were determined by discriminating fast ice and pack ice (i.e. non-fast ice) regions by analyzing the characteristics of surrounding features and changes in backscattering values measured over time (Figure 3. 3). Fast ice regions are distributed adjacent or attached to ice shelves along coastlines and form with an aid of icebergs acting as anchor points for fast ice formation (Massom et al., 2001; Giles et al., 2008; Fraser et al., 2012). Icebergs were masked out with a certain threshold to backscattering values to separate icebergs and sea ice. The threshold of -11 dB was empirically determined to remove icebergs in this study. Icebergs generally show higher backscatter than the surroundings that are composed of open water and sea ice (Williams et al., 1999; Mazur et al., 2017). In particular, icebergs are visually discriminated within relatively flat fast ice regions, while icebergs may not always show distinct contrast when compared to the surrounding

surface within heavily deformed sea ice (Wesche and Dierking, 2012; Wesche and Dierking, 2015). Although backscattering within fast ice regions varies, fast ice regions show consistent backscattering values over time when compared to pack ice regions. Fast ice edges were delineated along the boundary of the consistent backscatter patterns. To assess the validity of visual interpretation-based reference regions, time series of MODIS optical images with 250m resolution (MOD02QKM product) were used. Previous fast ice studies have used MODIS images to extract fast ice regions as reference data (Massom et al., 2010; Kim et al., 2015). Figure 3. 4 shows that SAR and MODIS images available in a 5-day time interval (31 Oct. 2010 - 5 Nov. 2010) for fast ice regions at the Getz Ice Shelf over Amundsen Sea sector to qualitatively ensure the fast ice regions. Although parts of the images are covered by clouds, fast ice regions are recognizable bounded by a fast ice edge (red line) in the MODIS images. Finally, based on the reference fast and non-fast ice regions extracted from consequent SAR images, input variables were extracted for the use of training (80% randomly selected) and test datasets (20%) to develop fast ice classification models with machine learning methods as explained in the next section 3.3.5.

### Nickerson Ice Shelf of Amundsen Sea



### Getz Ice Shelf of Amundsen Sea



### Dotson Ice Shelf of Bellingshausen Sea

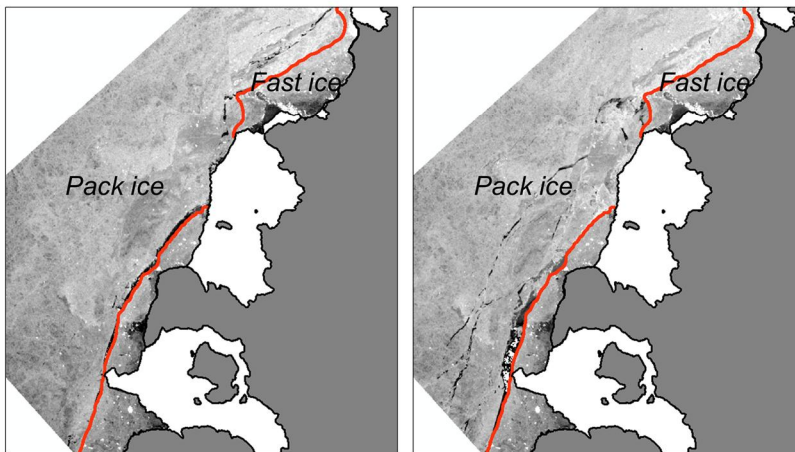


Figure 3. 3. Example of SAR images in a 5-day time gap used to detect fast ice edge for reference over Amundsen Sea and Bellingshausen Sea sectors. The Antarctic continent and ice shelves are shown in dark gray and white, respectively. The text in italic shows fast ice and pack ice (non-fast ice) regions.



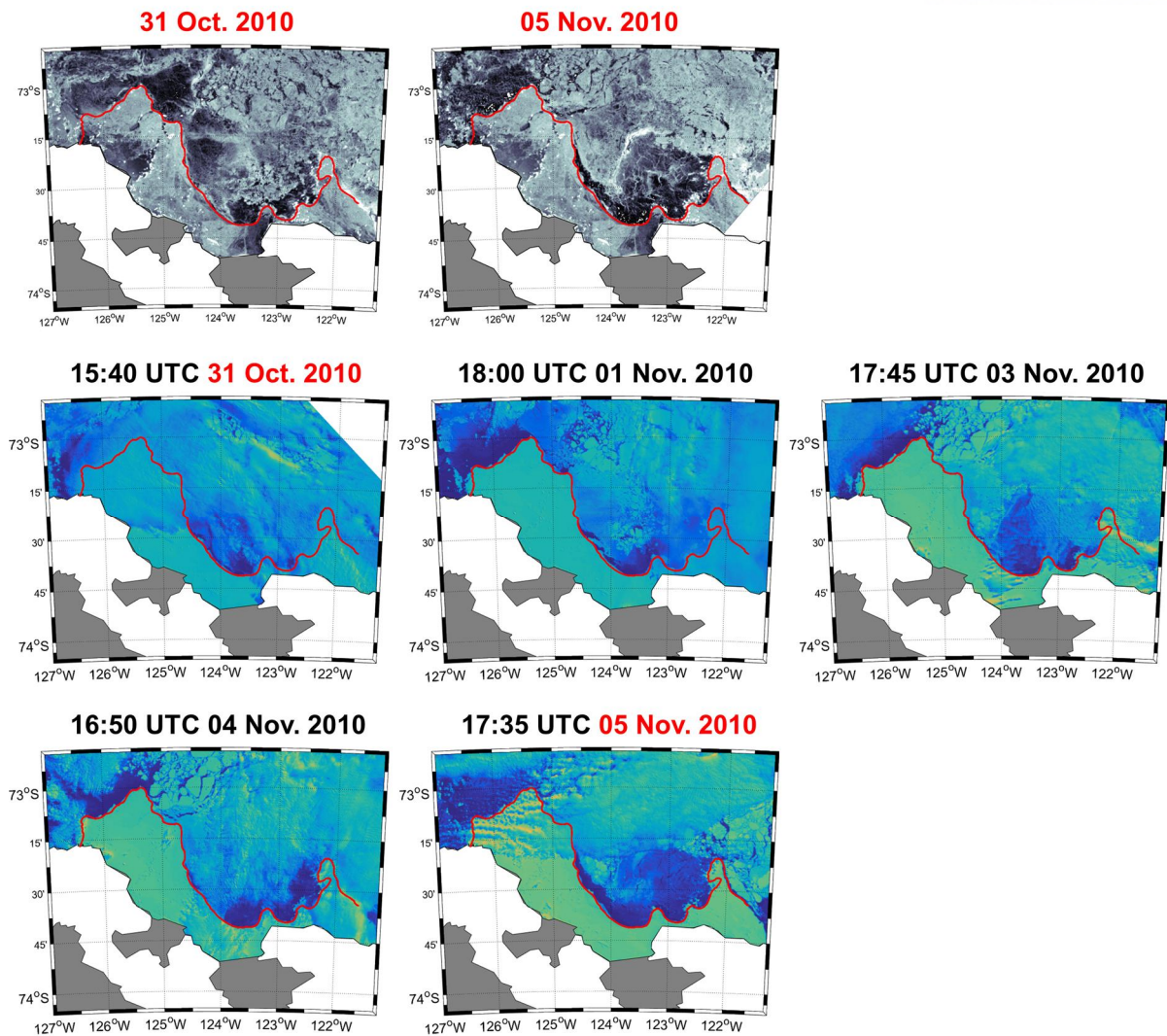


Figure 3. 4. Maps of landfast sea ice region at the Getz Ice Shelf over Amundsen Sea with SAR images of two dates (top row) and MODIS images available between 31 October 2010 and 5 November 2010 (middle and bottom rows).

### 3.3.5. Machine learning algorithm for classification

The original Methods for machine learning techniques of this chapter has been moved to Chapter 1 to avoid repetition.

The machine learning approaches used in this study are RF, ERT, and LR for developing fast ice classification models. Model performance was evaluated based on the test dataset. RF also provides relative variable importance as MDA. MDA means the average increase in the misclassification rate. A higher MDA indicates more important variable in classifying fast and non-fast class. The classification models were applied to other fast ice regions of interest over the Weddell Sea, Bellingshausen Sea, Amundsen Sea, and Ross Sea for model validation.

## 3.4. Results and Discussion

### 3.4.1. Segmentation parameterization

Figure 3. 5 shows segmentation results tested with various combinations of parameters. The optimal parameter combination was determined to be 25, 0.1, and 0.5 for scale, shape, and compactness parameters, respectively, based on fast ice reference regions identified by visual inspection. The larger the value of the scale parameter, the larger the objects produced (Figure 3. 5a). A scale threshold was set that visually identified ice objects which were always larger than the size of the segmented objects to avoid objects mixed with pack and fast ice. A scale threshold of 25 was identified to produce the most appropriate size of segmentation. Using a smaller scale value results in unnecessarily excessive segmentation of images, which is computationally more demanding for the subsequent analyses. The segmentation results with a smaller shape value show a distinctive difference of backscatter coefficients between objects (Figure 3. 5b). The result for various compactness parameter values show that using a larger compactness parameter produces a more compact and smaller size of objects (Figure 3. 5c.). On the other hand, in a smaller compactness criterion, the resultant objects are more elongated and rectangular, and are relatively bigger.

Figure 3. 6 shows input variables calculated based on segmentation results. Fast ice reference regions show high correlation values (bounded by the red solid line). This is because the variations of pixel values in the fast ice regions are relatively low, resulting in high correlation when compared to floating pack ice regions between two dates. It also indicates that the STD variable is able to distinguish fast ice from pack ice, in that lower STD values in fast ice regions appear than non-fast ice. The mean variable image shows a distinct contrast between sea ice and opening zones, such as flaws between pack ice and fast ice and seemingly polynya regions between sea ice and the Antarctic land with relatively low backscatter values. Sea ice is composed of different fractions of ice, brine, and air bubbles depending on its age. Radar backscatter is affected by the salinity, temperature, and density of sea ice, changing the dielectric constant and penetration depth of radar wave (Kwok et al., 1992; Wesche and Dierking, 2015). New and first-year sea ice mainly causes surface scattering showing low backscatter, whereas older and less saline sea ice is more dominated by volume scattering, resulting in increasing backscatter (Zakhvatkina et al., 2013; Wesche and Dierking, 2015; Casey et al., 2016). Compared to fast ice regions, moving pack ice regions have deformed sea ice patches, which can make the surface of pack ice rough and increase radar backscattering as well (Wesche and Dierking, 2012). Open water generally shows lower backscatter values than sea ice regions, but large wind speeds can roughen the surface of open water, increasing the backscattering (Wesche and Dierking, 2015). The backscattering of pack ice segments is high in areas where pack ice is dense but low where pack ice is mixed with open water.

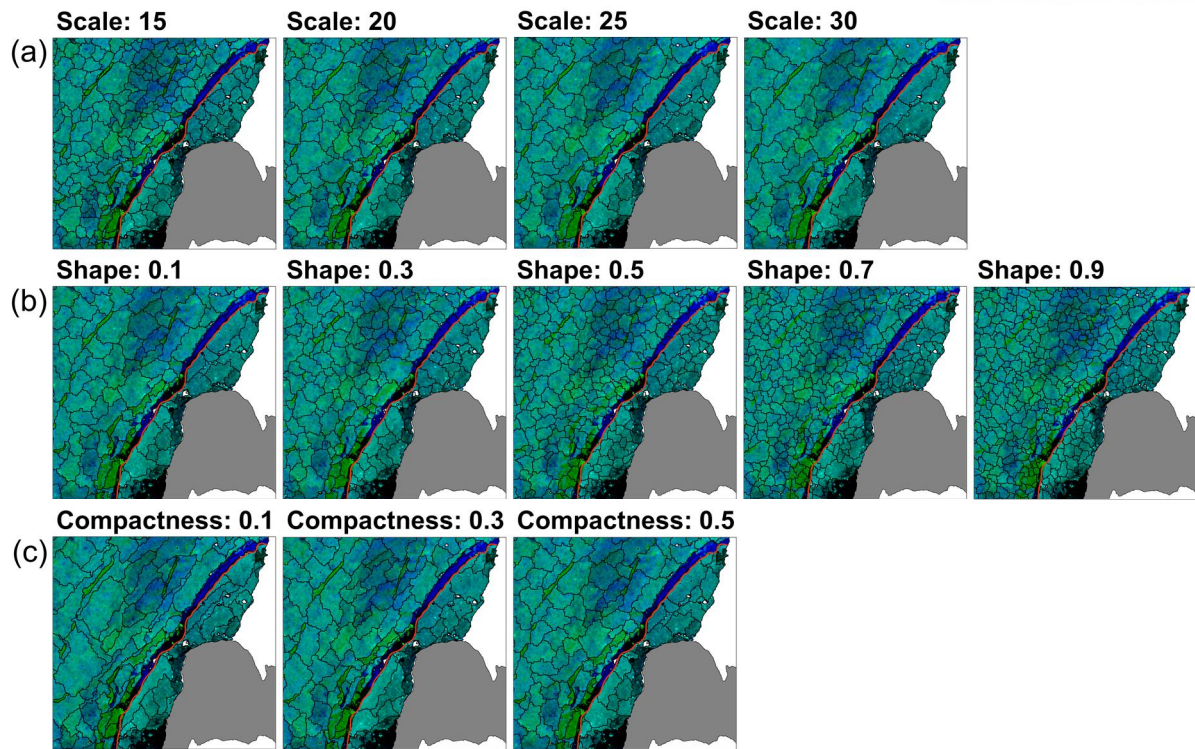


Figure 3. 5. Examples of segmentation results at different (a) scale parameters with fixed thresholds for shape of 0.1 and compactness of 0.5, (b) shape parameters with scale of 25 and compactness of 0.5, and (c) compactness parameters with scale of 25 and shape of 0.1 parameter setting. The red solid line indicates reference fast ice edge. The background is a false color composite image of date 1 (green) and date 2 (blue).



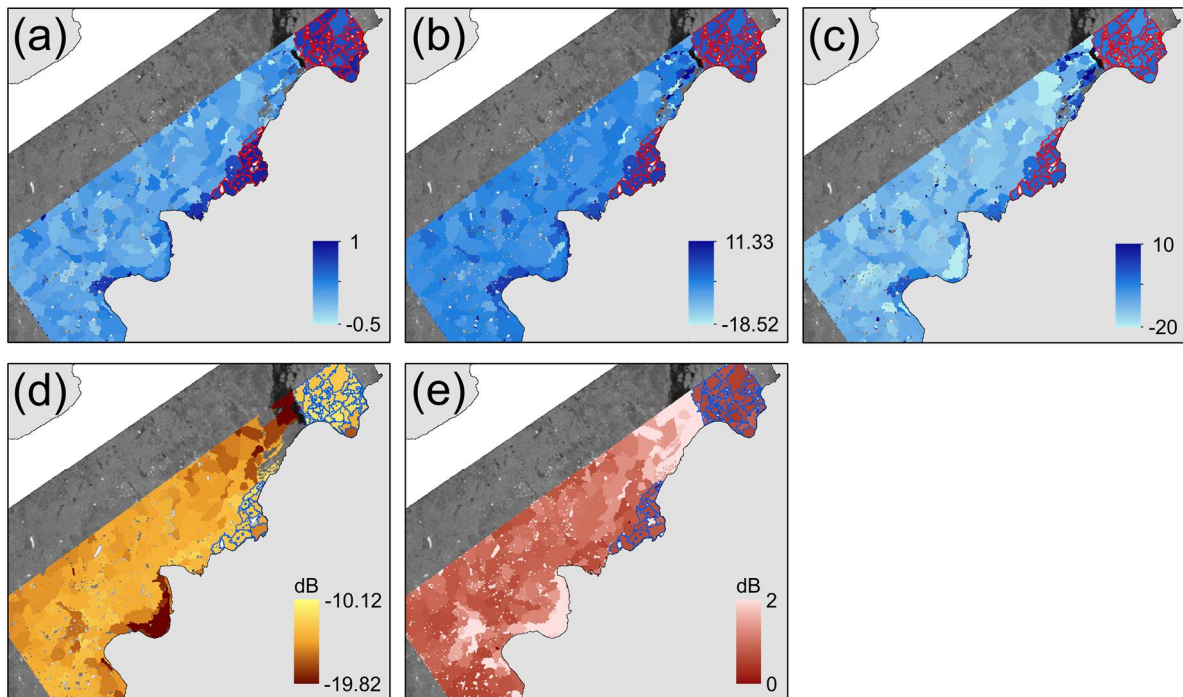


Figure 3. 6. Input variables extracted based on segmentation result including (a) correlation, (b) slope, (c) intercept, (d) mean of backscatter coefficient (in dB) for combined dates 1 and 2, (e) standard deviation of backscatter coefficient for combined dates 1 and 2. Gray area is the Antarctic land, and red and blue solid lines over sea ice zone indicate the reference fast ice edge.

### 3.4.2. Model evaluation and variable importance

Model evaluation results using the test datasets are shown in Table 3. 3-5. All three models produced similar results. The ERT model produced the best performance with an OA of 97.21% and a kappa coefficient of 0.94, while RF and LR models resulted in slightly lower performances with an OA of 96.74% and a kappa of 0.93. The fast ice class shows slightly higher PA than the non-fast ice class in all three models although the sample size of the non-fast ice class was twice that of the fast ice class. Different sample sizes of the two classes including 1:1, 1:2, and 1:3 for fast versus non-fast ice class were tested and 1:2 was identified as the most reasonable to classify fast ice regions with minimum commission and omission errors. Meanwhile, UA was lower for fast ice class than non-fast ice class as some of the non-fast ice samples were misclassified as fast ice class, which means that fast ice regions might have been slightly over-detected. A little over-segmentation might explain such an over-detection of fast ice as relatively homogeneous backscatter over time might have occurred by accident in very small objects even for the ice located off the shore. Contrarily, small non-fast ice objects nearby seaward fast ice edge were misclassified as fast ice due to the stationary backscatter strength of small segments. Fast ice objects located at the edge of seaward fast ice were occasionally misclassified into non-fast ice class due to low correlation between two dates. Generally, the stability of fast ice decreases toward the



edge of fast ice (Dammann et al., 2016). In particular, offshore-ward young and thin fast ice is less stable due to dynamic forcing by pack ice such as ridging and rafting. Sheltered ice which forms in areas such as bays where coastal topography protects fast ice from pack ice interaction is usually stable and was better detected by the three models (Figure 3. 8 and 3.9 in section 3.4.3) (Fraser et al., 2012; Dammann et al., 2016).

Figure 3. 7 shows relative variable importance results identified by RF and LR models with MDA and p-value transformed to the negative logarithmic scale, respectively. Correlation and STD variables were identified as significantly contributing variables to discriminate fast ice from non-fast ice regions in both RF and LR models. Correlation was highly significant since fast ice is an almost motionless feature compared to pack ice in a certain time interval (e.g., 5 days used in this study), which produces high correlation between two dates of imagery in fast ice regions and low correlation in non-fast ice regions. Secondly, the STD variable was considered to be the second significant variable for both models. This was because that backscatter variations in objects between two dates are larger in floating pack ice regions than relatively stationary fast ice regions.

Table 3. 3. Accuracy assessment result of the random forest model for the test dataset.

Reference \ Classified as	Fast ice	Non-fast ice	Sum	User's Accuracy
Fast ice	70	5	75	93.33%
Non-fast ice	2	138	140	98.57%
Sum	72	143	215	
Producer's accuracy	97.22%	96.50%		
Overall accuracy	96.74%			
Kappa coefficient	0.93			

Table 3. 4. Accuracy assessment result of the extremely randomized trees model for the test dataset.

Reference \ Classified as	Fast ice	Non-fast ice	Sum	User's Accuracy
Fast ice	70	4	74	94.59%
Non-fast ice	2	139	141	98.58%
Sum	72	143	215	
Producer's accuracy	97.22%	97.20%		
Overall accuracy	97.21%			
Kappa coefficient	0.94			

Table 3. 5. Accuracy assessment result of the logistic regression model for the test dataset.

Reference \ Classified as	Fast ice	Non-fast ice	Sum	User's Accuracy
Fast ice	70	5	75	93.33%
Non-fast ice	2	138	140	98.57%
Sum	72	143	215	
Producer's accuracy	97.22%	96.50%		
Overall accuracy	96.74%			
Kappa coefficient	0.93			

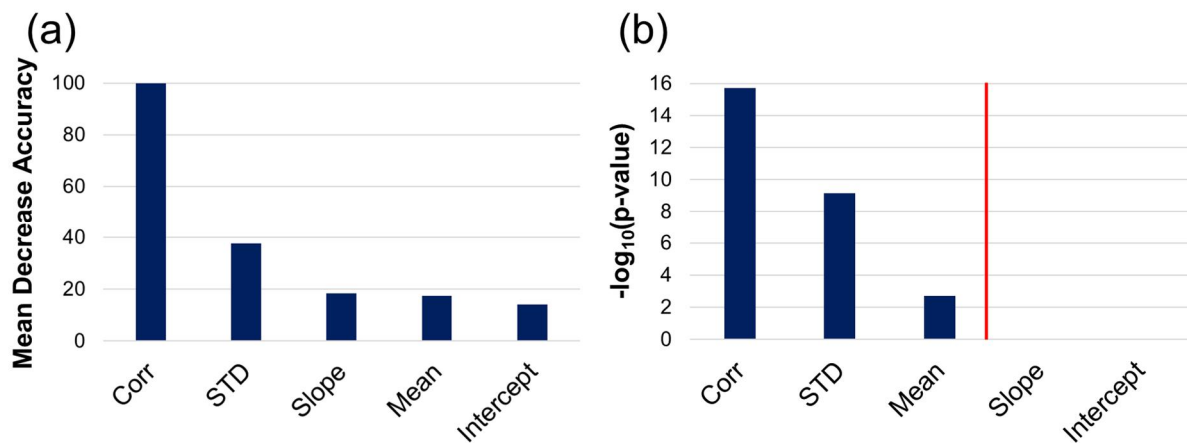


Figure 3. 7. Relative variable importance results indicated by (a) mean decrease accuracy of random forest and (b)  $-\log_{10}(\text{p-value})$  of logistic regression model.

### 3.4.3. Landfast sea ice detection for model validation

Fast ice detection models were tested for various fast ice regions over the other ocean sectors (Figure 3. 8-12). To assess the performance and extendibility of the models, validation sites were selected in different ocean sites with various conditions considering surrounding pack ice drift, wind exposure, atmospheric temperature, and icebergs that affect the development and stability of fast ice. For the qualitative evaluation, fast ice edges were extracted as reference data by visual interpretation of successive ALOS PALSAR ScanSAR images in 5-days intervals (red solid lines). Overall, fast ice regions over the validation sites were well detected by all three models including binary decision tree-based models (RF and ERT) and probabilistic statistical model (LR) without significant misclassifications or missing. The models did not show a significant performance degradation for the validation data, so that the models developed in this study can be well applied to unseen data in the

Western Antarctic. A few pack ice objects were misclassified as fast ice by the ERT and LR models (Figure 3. 8b and Figure 3. 9c). As explained in section 3.4.2, the misclassifications occurred because the small objects have high correlation between two dates of SAR images due to highly compacted pack ice with limited motion in a short time frame. Some objects were not detected as fast ice within fast ice regions (Figure 3. 11). These objects have a low probability of fast ice occurrence in LR model as well. The misclassified fast ice areas show some spatial variation of the surface over time in SAR images. Backscattering changes on the sea ice surface are not always related to the detectable movement of sea ice. The fast ice region of the Nickerson Ice Shelf showed a relatively low backscatter, which means that the ice surface is smooth. As fast ice regions have little or no motion, there is no dynamic phenomenon such as ridging or rafting, resulting in homogeneous surface. However, there are several factors that affect surface roughness associated with environmental changes. Strong wind speeds roughen the sea ice surface, causing changes in surface scattering (Komarov et al., 2017). Rough ice surface due to frost flowers occurring in the relatively flat fast ice regions can increase backscattering as well (Karvonen, 2004). In the fast ice site at the Nickerson Ice Shelf, it was confirmed that the surface of the objects that were misclassified as non-fast ice changed over time.

While differences in incidence angles can cause a backscattering variation, sea ice itself evolves over time, which will result in different backscattering coefficients due to the changing interaction between sea ice and radar (Mahoney et al., 2006). In the SAR images used in this study, incidence angle effect was not visually obvious. Incidence angle effect usually tends to be more clearly identified in open water than in sea ice (Zakhvatkina et al., 2017). We note that there is also no apparent influence of incidence angles in fast ice classification results. As a supplement, it was not identified as a particularly important variable when the incidence angle was added into the set of input variables (not shown). This indicates that the proposed models can detect fast ice without the problem of incidence angle effect, especially when the difference in incidence angles is not significant. The differences in incidence angles identified in this study range from about  $1.5^{\circ}$  to  $3^{\circ}$ , which implies that the proposed models can be used to detect fast ice in other regions with similar incidence angle configurations.

Antarctic sea ice chart data were used to evaluate the reliability of fast ice detection models using object-based SAR data. Sea ice chart data obtained at 15 November 2010 for the fast ice region of the Bellingshausen Sea sector were available. The ice chart superimposed on a model detection result is shown in Figure 3. 12. The visual comparison shows a good agreement but a difference at the top of the scene. In a closer analysis of the two SAR images for the difference, it was clearly confirmed that there are the movements of icebergs trapped in sea ice and the occurrence of openings by leads and rectilinear or wedge-shaped cracks. The reason for the difference may be attributed to the length of the time interval used to define fast ice. Previous studies explain that using a longer time interval over fast ice tends to detect smaller fast ice areas due to a lower likelihood that the ice will remain stationary for the entire

period, whereas using a shorter time interval can confuse temporarily frozen drift ice as fast ice. A relatively long time interval (e.g., 20 days) has been used as a tradeoff, but generally, it is due to data availability constraints by a long revisit time of satellite sensor systems especially for optical sensor and InSAR data. There is no fixed time interval that is appropriate for the delineation of fast ice. The bi-weekly Antarctic sea ice chart defined a slightly wider area as fast ice despite using a longer time interval than this study. Although the two data with different time intervals have different physical definitions, they show very consistent results.

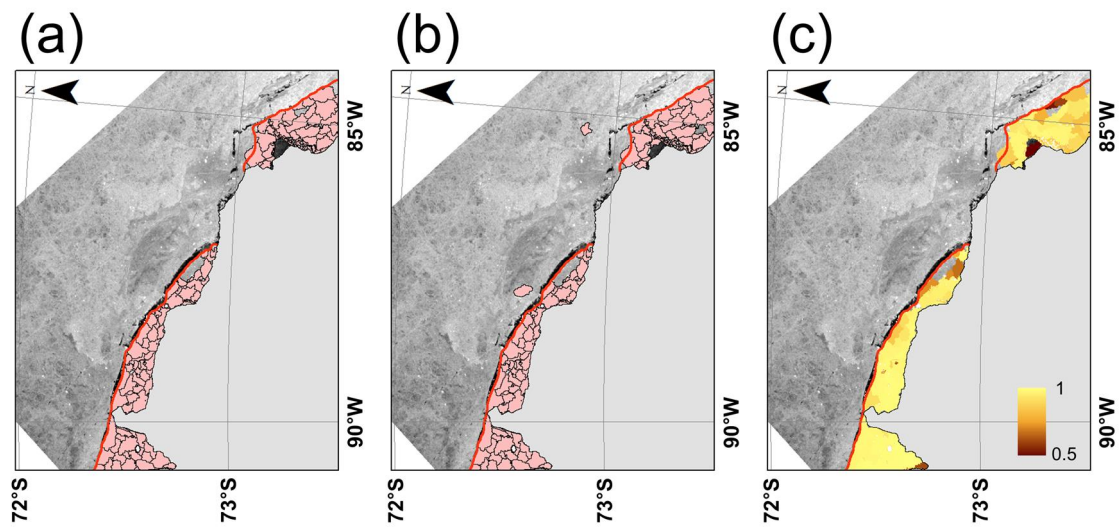


Figure 3. 8. Landfast sea ice detection results at the Bellingshausen Sea region of (a) random forest (RF), (b) extremely randomized trees (ERT), and (c) logistic regression (LR) models. Red solid lines indicate the reference fast ice edge, RF and ERT results are shown in pink color and LR result for the probability of fast ice coverage in yellowish-shatched color, and gray area is Antarctic land.

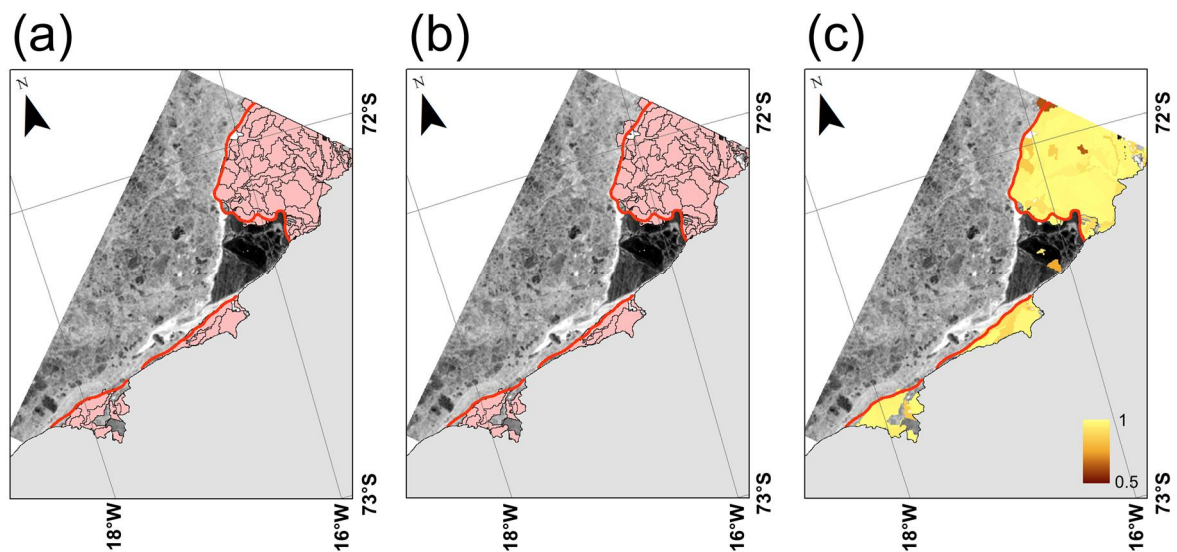


Figure 3. 9. Landfast sea ice detection results at the Brunt ice shelf at the eastern Weddell Sea site of (a)

random forest (RF), (b) extremely randomized trees (ERT), and (c) logistic regression (LR) models. Red solid lines indicate the reference fast ice edge, RF and ERT results are shown in pink color and LR result for the probability of fast ice coverage in yellowish-starched color, and gray area is Antarctic land.

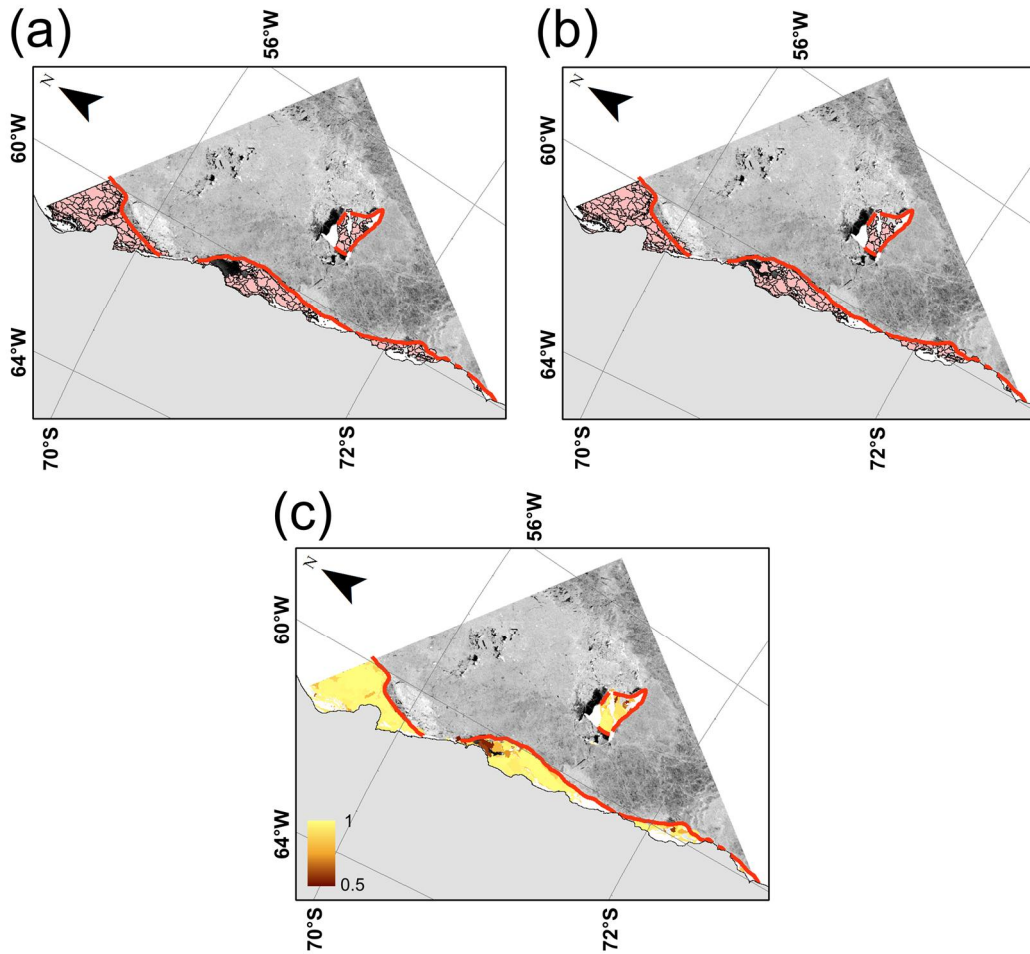


Figure 3. 10. Landfast sea ice detection results at the Larsen ice shelf of the Antarctic Peninsula of (a) random forest (RF), (b) extremely randomized trees (ERT), and (c) logistic regression (LR) models. Red solid lines indicate the reference fast ice edge, RF and ERT results are shown in pink color and LR result for the probability of fast ice coverage in yellowish-starched color, and gray area is Antarctic land.



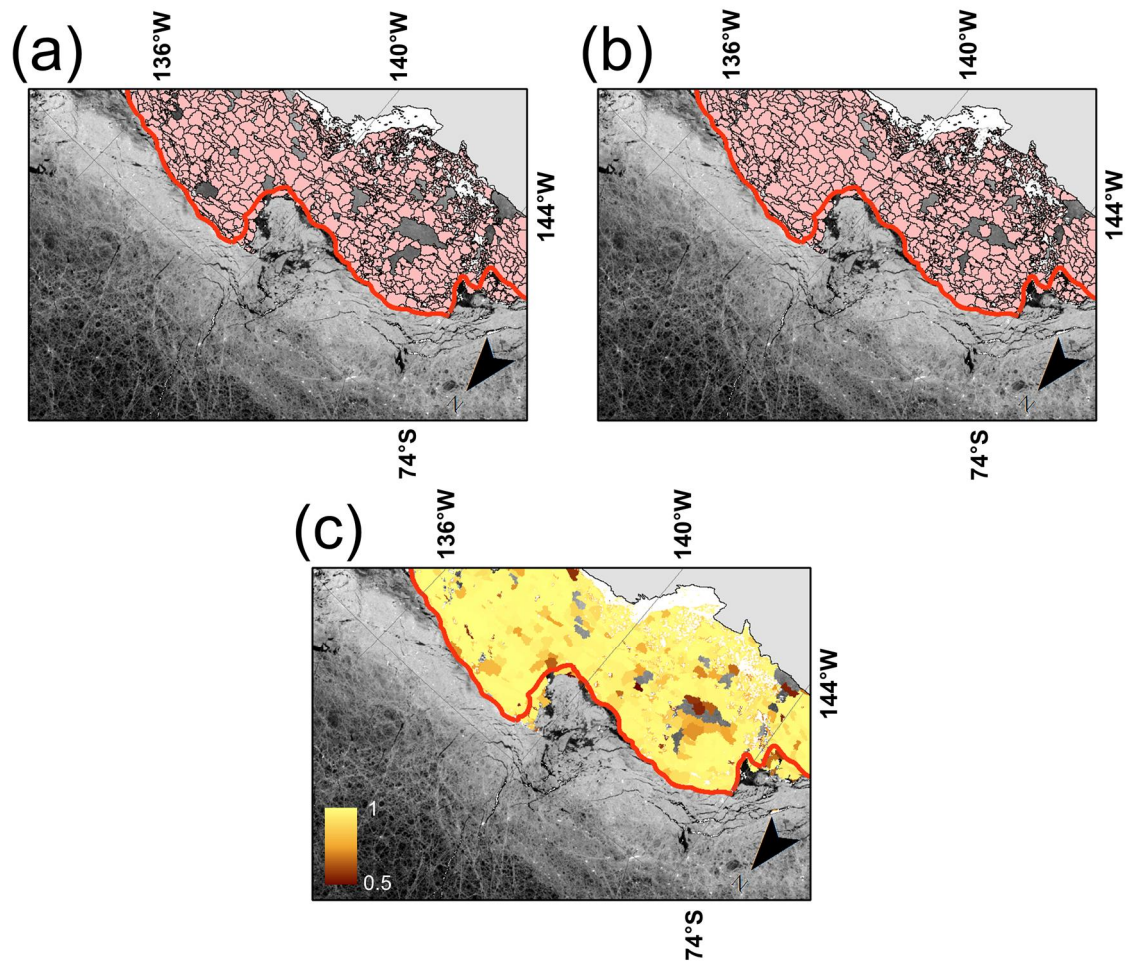


Figure 3. 11. Landfast sea ice detection results at the Nickerson ice shelf in the east of the Ross Sea of (a) random forest (RF), (b) extremely randomized trees (ERT), and (c) logistic regression (LR) models. Red solid lines indicate the reference fast ice edge, RF and ERT results are shown in pink color and LR result for the probability of fast ice coverage in yellowish-starched color, and gray area is Antarctic land.

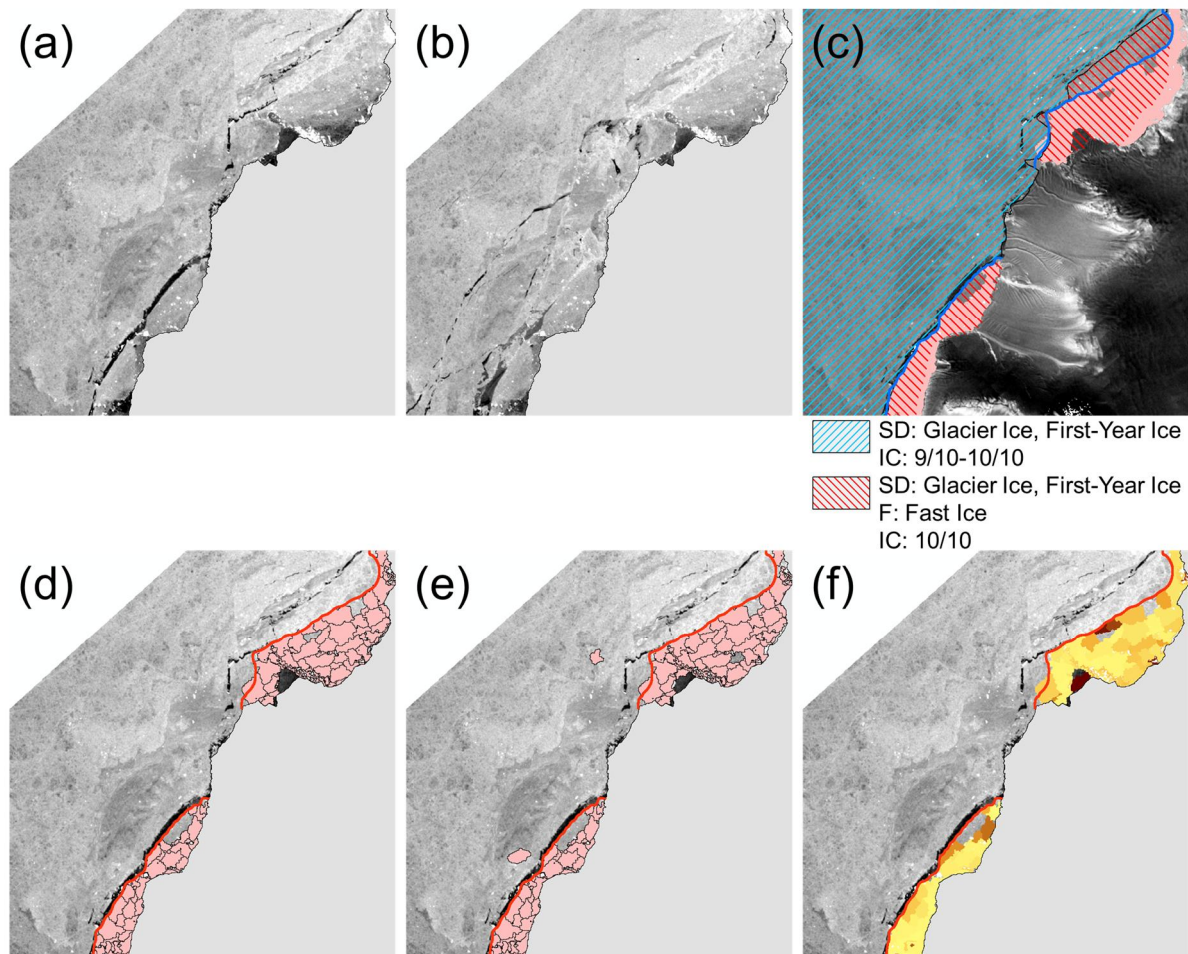


Figure 3. 12. Qualitative analysis results. (a) Backscatter image of L-band HH-pol ALOS PALSAR for date 1; (b) backscatter for date 2; (c) comparison between the Antarctic Ice Chart and RF result (pink area). The light blue and red hatched areas are from the Antarctic Ice Chart. SD, F, IC are abbreviations for ice chart codes meaning Stage of Development, Form of ice, and sea Ice Concentration, respectively. The blue solid line is fast ice edge as a reference. (d-f) Results of machine learning models (RF, ERT, LR, respectively) with fast ice edge as a reference (red solid line).



### 3.5. Conclusions

This study showed that bi-temporal L-band ALOS PALSAR data with a short time interval (i.e., 5 days) is capable of detecting Antarctic fast ice. This study suggested a novel approach combining image segmentation, image correlation analysis, and machine learning techniques to detect fast ice regions. As fast ice is a spatially homogeneous sea ice area, the proposed object-based approach is more effective than pixel-based ones when using SAR images with high spatial resolution. Fast ice regions have little motion over time, so it is possible to distinguish fast ice regions that are highly correlated between the two consecutive satellite images compared to non-fast ice regions. In addition, the fast ice detection method using SAR data provides an opportunity to study in more detail the rapidly changing interaction between fast ice and non-fast ice regions in a short time period, which was not possible in previous studies.

The model performance results show that all three models produced high accuracy. Marginally misclassified or undetected fast ice cases occurred in unstable areas, which are generally affected by the surrounding environment at the edge of fast ice. Correlation and STD of backscattering were identified as the most important and contributing variables for detecting fast ice. This coincides with the physical characteristics of fast ice regions with little motion over time and spatial homogeneity. The validation results for several unseen data for the West Antarctic ocean sectors showed that the proposed approach did not show significant performance degradation. The results obtained from various reference data confirm the robustness and reliability of the proposed algorithm particularly using ALOS PALSAR images. We expect this algorithm to show a wider fast ice application for different regions.

Unlike most previous studies which focused on the East Antarctic, this study focuses on fast ice regions in the West Antarctic coast, which implies that the research findings from this study can be used as a basis of future fast ice research in the West Antarctic. We have also extracted fast ice regions in a short time interval (i.e. 5 days) using spatially overlapped regions of SAR images (considering small differences in incidence angles) regardless of repeat cycles. Fast ice detection conducted in earlier studies was limited to a longer time interval (e.g. 20 days).

However, this study is limited to the L-band ALOS PALSAR data and temporally in winter and spring in two years (i.e., 2007 and 2010), not covering all seasons. Thus, it is not possible to generalize the proposed model directly using other SAR images due to the different characteristics of other bands to sea ice or different seasons. Nonetheless, in principle, the proposed approach is applicable to other fast ice sites but might require a new calibration process using SAR data. In future research, RADARSAT-2 and PALSAR-2 will be able to produce fast ice data by using full polarimetric data, which provides valuable information on different scattering mechanisms depending on sea ice properties.

## Chapter 4

### Distribution and variability of landfast sea ice along the Amundsen Sea of West Antarctica

#### 4.1. Abstract

Fast ice, which is distributed extensively along the Antarctic coastline, interacts with the atmosphere and the oceans. It is closely related to the surrounding Polynya regions and ice shelves. Although long-term analysis of time series fast ice in East Antarctica has been conducted, the West Antarctic fast ice was not well investigated in previous research. This study used MODIS and AMSR-E images to obtain near decade-long time series of fast ice in the Amundsen Sea of West Antarctica at intervals of 15 days from July 2002 to September 2011. The generated fast ice maps well corresponded to SAR images from ALOS PALSAR data that were used as reference. The distribution and morphology of fast ice were examined with the corresponding bathymetry map and icebergs distribution from a SAR imagery. Fast ice distribution showed regional differences depending on the shelves in terms of the velocity of calving flux and bathymetry. Time series trends of fast ice extent were analyzed with their extent anomaly by showing anomalous fast ice breakup events.

## 4.2. Introduction

Much of the original Introduction and literature review of this chapter has been moved to Chapter 1 to avoid repetition.

Studies on long-term, large-scale fast ice have been largely concentrated in the East Antarctic (Fraser et al., 2012; Miles et al., 2017; Aoki, 2017), and studies focused on the distribution and variations of West Antarctic fast ice are rarely conducted (Nihashi et al., 2015). Fraser et al. (2012) analyzed time series of fast ice extent only for East Antarctica. By analyzing 20-day cloud-free images using MODIS images of time series, they extract long-term East Antarctic fast ice area and analyze variability of fast ice along the East Antarctic coastline. Nihashi et al. (2015) investigated the relationship between Antarctic coastal polynyas and fast ice using passive microwave data and reanalysis data including winds and air temperatures. They used three months of AMSR-E data to extract monthly fast ice regions. Then, the frequency of fast ice cover during the whole study period was analyzed with the distribution of polynyas. Additionally, as the Antarctic fast ice and ice shelves are closely related, previous studies have conducted research on relationship between each other. Massom et al. (2010) studied the relationship between Mertz Glacier Tongue in East Antarctica and perennial fast ice adhered to the eastern edge of the tongue. Miles et al. (2017) analyzed the correlation between glacier calving events and breakup timing of fast ice using various satellite data such as MODIS and SAR images. Aoki et al. (2017) extracted the time series East Antarctic fast ice edges and compared it with tropical Pacific sea surface temperatures. They analyzed the breakups of fast ice and calving front changes. However, there has been no study on the regional distribution variability of long-term time series of the West Antarctic fast ice.

The aim of this study is to conduct a detailed analysis of long-term fast ice extent around West Antarctic coast, specifically the Amundsen Sea, using MODIS IST and AMSR-E brightness temperature data and additional variables derived from the data with a machine learning technique in a short time interval. The distribution and variability of fast ice was analyzed with atmospheric and oceanic data from ERA-Interim reanalysis data. This study will improve our understanding of fast ice distribution and variations over West Antarctica and give more insights for the response of fast ice to climate changes.

### 4.3. Study area

This study was conducted focusing on the western side of Amundsen Sea in West Antarctica (Figure 4.1). This area is where fast ice is formed along the shoreline in West Antarctica (Nihashi et al., 2015). During the study period, the ice shelves along the Amundsen and Bellingshausen Sea are experiencing rapid thinning (Pritchard, 2012). The relatively thick Land and Getz ice shelves thinned between 2003 and 2008, whereas the thinner Nickerson and Sulzberger ice shelves had relatively no significant thinning. The ice shelf of the West Antarctic Sea experienced a decrease in the overall basal mass balance. In the Land Ice Shelf, the rate of calving flux was higher than that of basal melt, but the Sulzberger Ice Shelf showed basal melt rather than glacier calving (Depoorter et al., 2013). Therefore, the study area is suitable for analyzing the distribution and variability of fast ice regions due to the different types of ice shelves in terms of geographical characteristics.

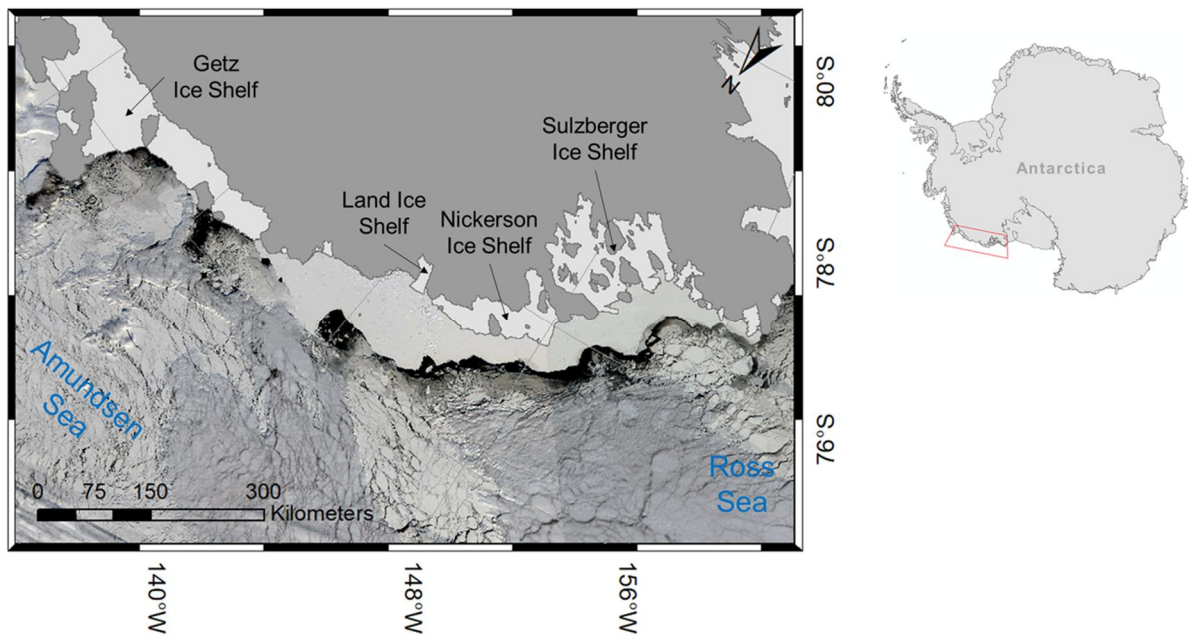


Figure 4. 1. Process flow diagram.

### 4.4. Data and Methods

#### 4.4.1. Reference data for landfast and non-landfast sea ice

Fast ice and non-fast ice are the targets to be classified. For the construction of reference data, fast ice and non-fast ice regions were extracted using MODIS reflectance and AMSR-E brightness temperature images. MODIS reflectance images are usually used during polar summer seasons (i.e.

from mid-September to early April). AMSR-E brightness temperature images are used in the absence of sunlight during polar night (i.e. from mid-April to early September). The images were examined in 5-day time intervals to discriminate fast ice regions motionless for 5 days from non-fast ice regions. Reflectance and brightness temperatures are consistent for fast ice regions over a period, while non-fast ice regions show spatial changes in values of reflectance and brightness temperatures. The imagery were taken from MODIS (Terra and Aqua) corrected reflectance and AMSR-E sea ice brightness temperature (horizontally and vertically polarized at 89 GHz) of the NASA Worldview (<https://worldview.earthdata.nasa.gov/>). It is a useful web-based tool to easily identify and record the locations of fast and non-fast ice regions.

#### 4.4.2. Generation of landfast sea ice maps

The original Methods for machine learning techniques of this chapter has been moved to Chapter 1 to avoid repetition.

Fast ice detection models were developed using RF models with TB from AMSR-E channels, MODIS IST data, and additional variables derived from AMSR-E and MODIS data (Figure 4.2). TB images were downsampled into 4 km spatial resolution of MODIS IST data, which means that the final spatial resolution maps are generated at 4 km grid resolution. Table 4.1 shows a total of 14 input features that were used to develop fast ice detection models. Based on the characteristics of fast ice, which fast ice are motionless during a certain period of time, additional correlation variables in 5-day intervals called NCI were added in addition to the simple channel brightness temperatures used in the study of Chapter 2. MODIS IST data were used as one of main input data for the detection of fast ice. The daily MODIS Terra and Aqua IST products including MOD29E1D and MYD29E1D were used for 2002 to 2011, which are gridded to 4 km spatial resolution Lambert Azimuthal Equal-Area projection. Because sea ice is colder than open water, it is relatively easy to discriminate fast ice from the ocean, and there is a temperature difference between fast ice and pack ice that partly contains open water. However, due to the presence of clouds and polar night in the Antarctic winter, the data were not available during the period approximately from mid-April to early September.

Brightness temperatures from the frequencies of AMSR-E were used as another main input data to detect fast ice. The emissivity of ice is considerably higher than that of water (Shokr and Shinha, 2015). Sea ice is radiometrically warmer by emitting more energy in the microwave band. This is why passive microwave data were used to distinguish sea ice from open water. The horizontal and vertical polarization daily data of 6.925, 10.65, 18.7, 23.8, 36.5, and 89.0 GHz channels between 2002 and 2011 were used. All channels except for 89.0 GHz with 6 km spatial resolution have 12 km spatial resolution and were downgraded into 4 km resolution of MODIS IST using bilinear interpolation method (i.e. the

output value is a weighted average of pixels in the nearest 2-by-2 neighborhood).

Two separate algorithms were designed to detect fast ice; Algorithm 1, in which AMSR-E and MODIS data are both used together, and Algorithm 2, which AMSR-E is used only. To build training data for machine learning input, samples were extracted for two classes (i.e. fast ice and non-fastice). Reflectance and temperature images from MODIS of Aqua and Terra available in the Worldview website were utilized to identify reference fast ice regions for sample extraction. The final fast ice detections were post-processed by detecting fast ice regions which are contiguous with the coast. After that, fast ice detections in 5-day intervals in a month were collected, and fast ice with high frequency was determined as the final fast ice region.

Table 4.2 shows the number of samples constructed for fast ice and non-fast ice according to each season and algorithm. As fast ice regions are relatively smaller than non-fast ice regions that include floating pack ice and open ocean, samples for non-fast ice class were collected averagely 2.5 times more than for fast ice class to cover a wide spectrum of the values of input variables for non-fast ice class. Total datasets were used to construct fast ice detection model. The OOB data of RF were used for the evaluation of model performance to find the best model that minimized the error for the OOB data. As validation data, ALOS PALSAR SAR images were used to quantitatively evaluate fast ice maps. SAR data is well suited for accuracy assessment because of its much higher spatial resolution. First year ice with a smooth surface shows a relatively low backscatter, while icebergs, ice shelves, multiyear ice, and ridged and deformed first year ice shows high backscattering. Depending on the surface roughness, backscatter of fast ice may look similar to open water with large surface waves due to wind. Therefore, it is difficult to distinguish fast ice from a single SAR image (Mahoney, 2004), so a time-series SAR images can be used to identify stable areas over time. We examined the two time-series SAR images with specific date intervals and considered the areas where the backscatter was kept constant over time. Based on these characteristics, we delineate the edge of the fast ice and use it as a reference. The accuracy of the fast ice reference data was compared with fast ice detection results. The accuracy matrices include the PA, the UA, the OA, and the kappa coefficient.



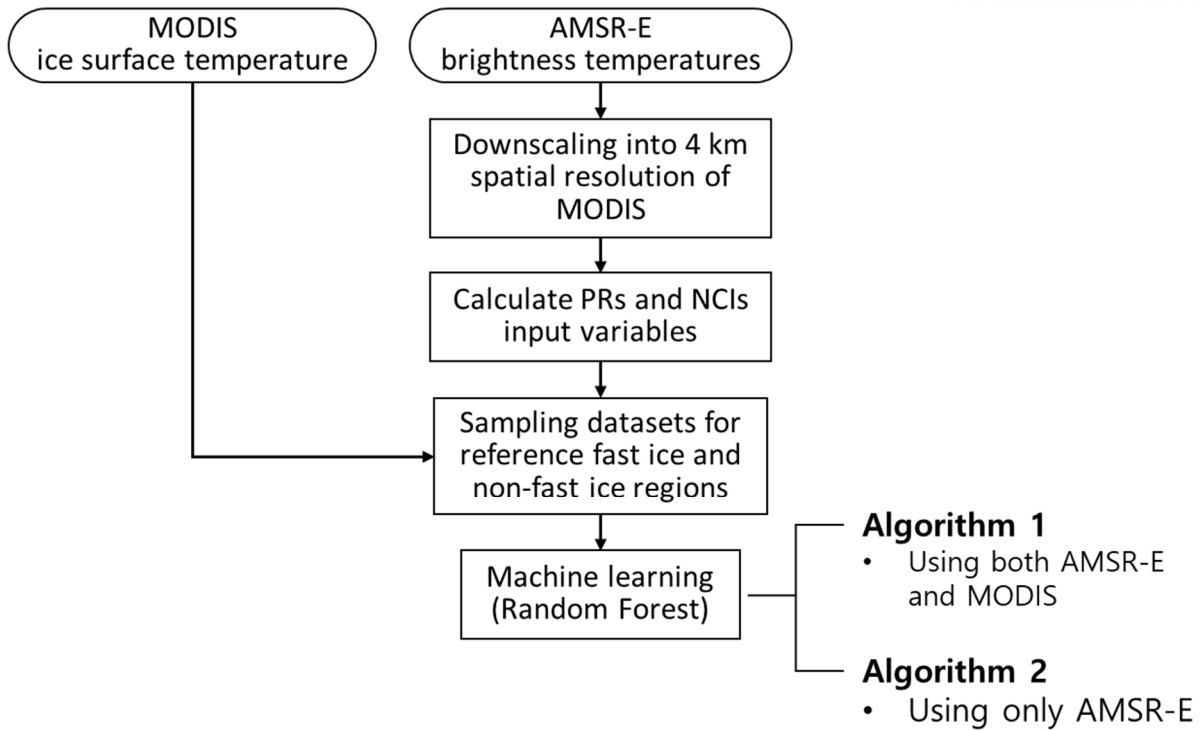


Figure 4. 2. Process flow diagram.

Table 4. 1. Input variables used in this study to detect fast ice.

Input Type		Variables
MODIS IST		IST <sub>max</sub>
AMSR-E brightness temperatures		TB89h*, TB89v
Polarization ratios	Polarization Ratio (PR)	PR(18)
	Spectral Gradient Ratio (GR)	GR(36V18V), GR(23V18V)
	Difference between GRs (dGR)	dGR = GR(89H18H) – GR(89V18V)
	Simple ratios	18V/18H, 23V/23H, 36V/36H, 89V/89H
Neighborhood Correlation Images		Correlation, Slope, Intercept for 89H, 89V

\*horizontal or vertical polarization of a frequency (GHz)

Table 4. 2. Number of samples for fast ice and non-fast ice class by season and algorithm.

	Algorithm 1		Algorithm 2	
	Fast ice	Non-fast ice	Fast ice	Non-fast ice
Spring	3626	9350	5973	17141
Summer	8306	21926	12030	27769
Autumn	2405	4662	4454	9498
Winter	953	1798	3546	11831

Table 4. 3. Information of ALOS PALSAR SAR images used for model validation during study period from July 2002 to September 2011.

Location	Day1	Day2	Date difference
Land Ice Shelf	26 Jul. 2007	5 Aug. 2007	15
	5 Aug. 2007	15 Aug. 2007	10
	15 Oct. 2010	27 Oct. 2010	12
	30 Nov. 2010	14 Dec. 2010	14
	5 Jan. 2011	17 Jan. 2011	12
Sulzberger Ice Shelf	5 Aug. 2007	20 Aug. 2007	15
	10 May 2008	21 May 2008	11
	21 Oct. 2010	4 Nov. 2010	13

## 4.5. Results and Discussion

### 4.5.1. Performance of landfast sea ice mapping model

Figure 4.3-4 show the relative variable importance of fast ice mapping model for algorithm 1 and 2, respectively. The top 5 most important variables were identified as ISTmax, GR3618, GR2318, r89, and TB89v in algorithm 1 to discriminate fast ice from non-fast ice class, and GR2318, GR3618, r89, r36, and TB89v in algorithm 2. In algorithm 1, the IST variable was the most contributing feature in all seasons. This is because the IST images at 4-km spatial resolution have the ability to more clearly distinguish between fast ice and non-fast ice areas, as compared to 12-km resolution for brightness temperatures and other derived variables. GR3618, GR2318, r89, and TB89v variables ranked higher among input features for both algorithms in most seasons. Overall, the ratios of TBs were used more importantly over the 89-GHz TB, because polarization and gradient ratios are less sensitive to variations in physical ice temperatures (Cavalieri et al., 1984; Comiso et al., 2003). Polarization ratios of TBs have been widely adopted to classify open water and sea ice types (Tamura et al., 2008; Comiso et al., 2008). Corr89v calculated with TB89v was also often included in important variables. Although the temporal correlation of TBs has not been used as a primary input data other than complementary uses in previous studies (Fraser et al., 2010), this study suggests that temporal correlation properties of TBs are potentially useful for distinguishing fast ice and non-fast ice regions. Optimal input variables would be varied according to extraction of datasets, it is worthy to note that Kwok et al. (1998) used temporal correlation of TBs for tracking of sea ice motion and reported that a temporal correlation of TBs as a useful feature in detecting temporally correlated sea ice. Figure 4.5 shows the OA for OOB data of RF model according to season and algorithm. The algorithms have satisfactory performances for each season. Meanwhile, algorithm 1 produced higher accuracies than algorithm 2, meaning that IST variable with high spatial resolution was obviously more effective to discriminate between classes as explained in variable importance.

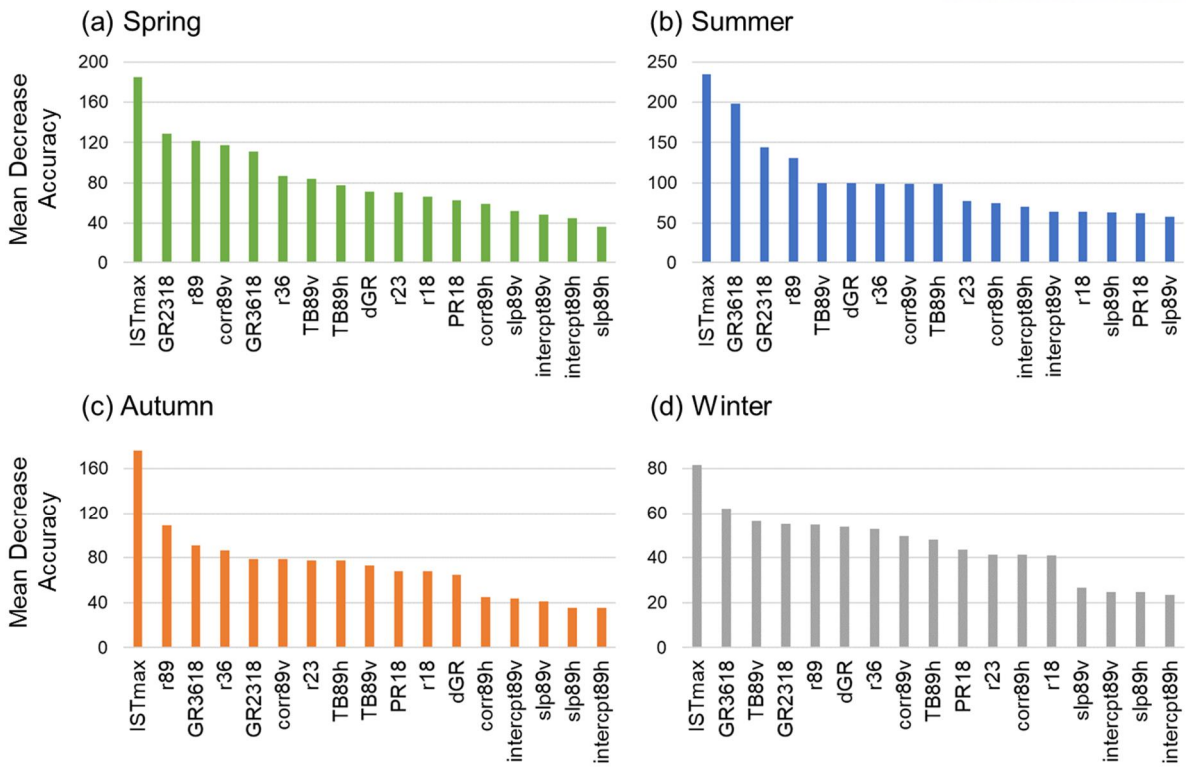


Figure 4. 3. Relative importance of variables for landfast sea ice mapping model for algorithm 1.

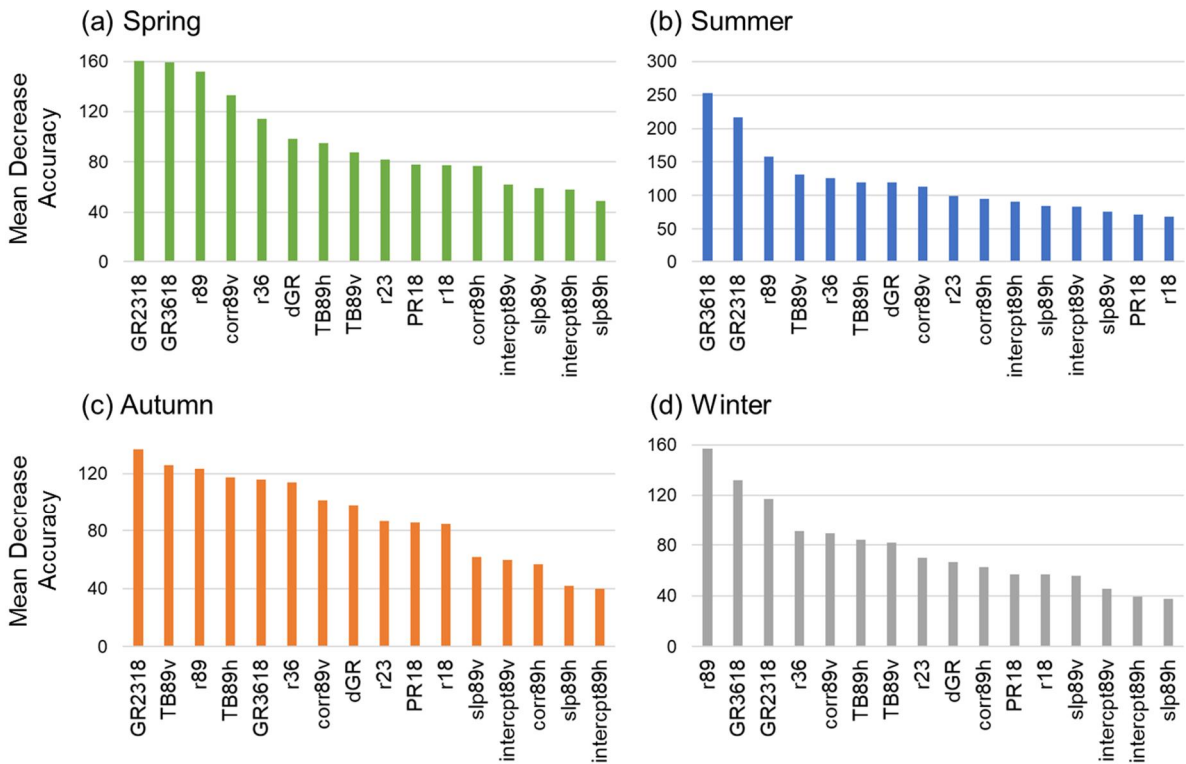


Figure 4. 4. Relative importance of variables for landfast sea ice mapping model for algorithm 2.

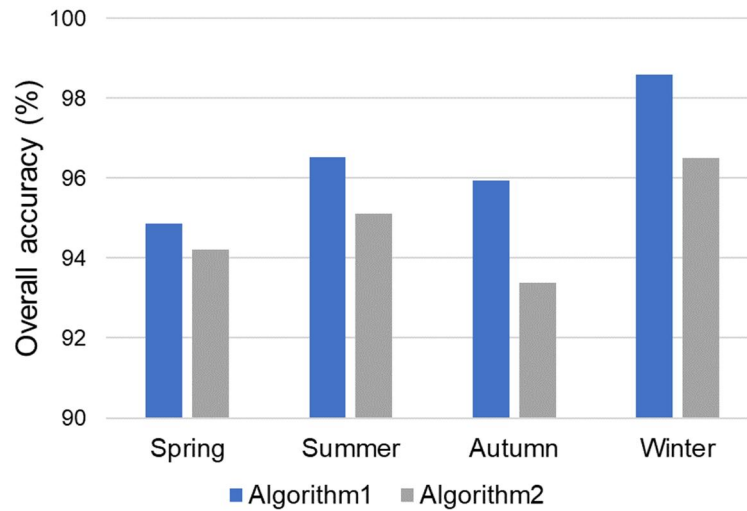


Figure 4. 5. Overall accuracy for out-of-bag error of random forest model by season and algorithm.

#### 4.5.2. Comparison of fast ice maps with SAR images

The generated fast ice maps were compared with SAR images acquired from ALOS PALSAR data. All accuracy measures show a significantly good performance for both fast ice and non-fast ice classes as shown in Table 4.4. For fast ice regions that are falsely detected as non-fast ice, the errors were mainly caused by the early stages of fast ice formation consisting of nilas or young ice. Thin ice including new ice and nilas have low backscatter due to its smooth surface (Wakabayashi et al., 2004). The corresponding SAR images of ALOS PALSAR show relatively low backscatter over the fast ice region. However, when examining the corresponding 89-GHz vertically polarized AMSR-E TB images, the thin fast ice regions represent high TBs. Fast ice regions tend to have low TBs than thin ice as fast ice is generally covered with thick snow, hence leading to the surface condition of fast ice closer to that of ice sheet (Nihashi et al., 2015). Moreover, sea ice is newly formed in polynya areas during wintertime, which tend to be high brightness temperatures. Therefore, TB-based models of this study will cause misclassification for fast ice in the early stages of formation, TBs of which are similar to new ice in polynya area. Figure 4.6 shows fast ice maps with bitemporal SAR images for comparison. Fast ice regions detected by RF model are in close agreement with the fast ice reference regions delineated by SAR images. In the two SAR images of a certain period interval, the fast ice area shows a consistent backscatter over time. It can be seen in the SAR images that fast ice regions form along icebergs spread out especially over the Land Ice Shelf region. On the other hand, non-fast ice regions have high spatiotemporal variability of backscatter.

Table 4. 4. Accuracy assessment results of landfast sea ice maps based on SAR images.

		Original		Sum	UA
		Fast ice	Non-fast ice		
Results	Fast ice	357,247	5,122	362,369	98.59%
	Non-fast ice	21,321	470,740	492,061	95.67%
Sum		378,568	475,862	854,430	
PA		94.37%	98.92%		
OA				96.91%	
Kappa				0.94	

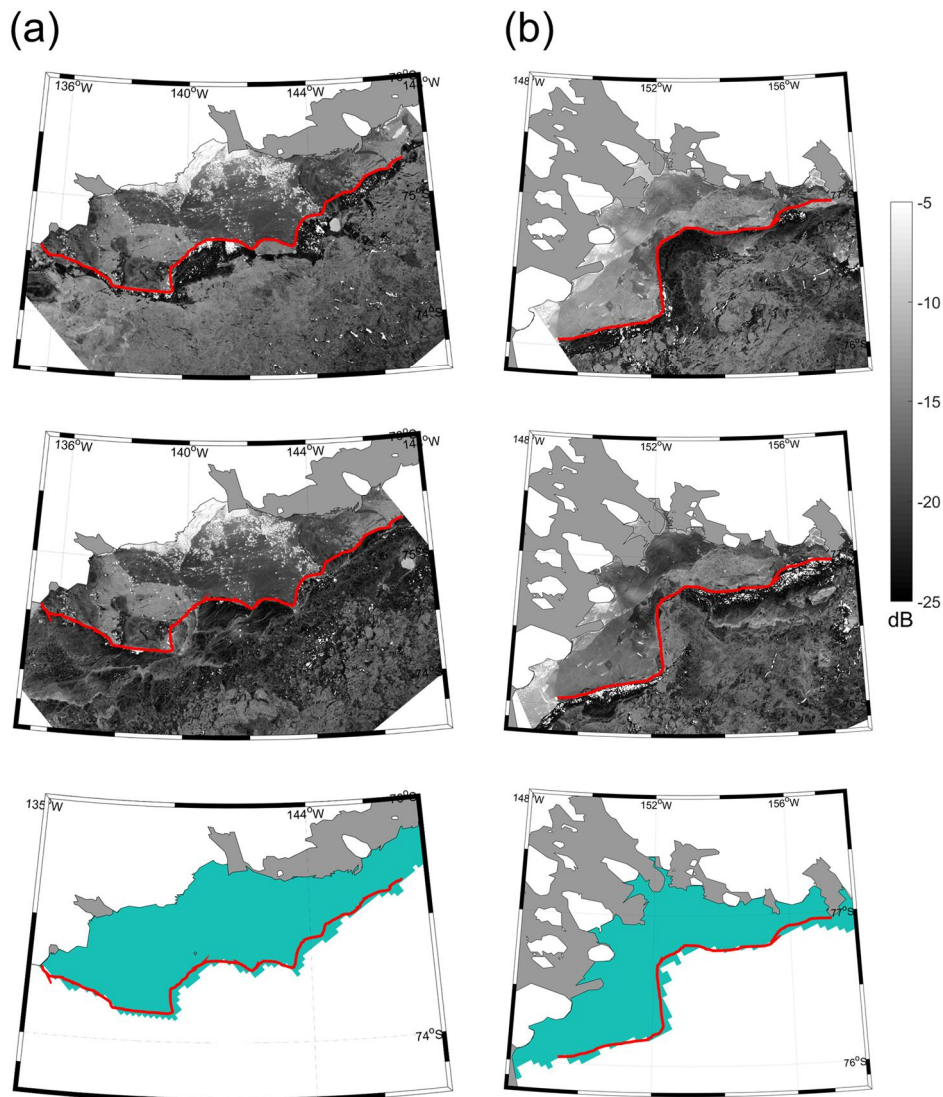


Figure 4. 6. Examples of ALOS PALSAR images and corresponding fast ice maps for (a) Land Ice Shelf fast ice site on 31 October 2010 and (b) Sulzberger Ice Shelf fast ice site on 15 May 2008. SAR images for Land Ice Shelf site were acquired on 15 October 2010 and 27 October 2010, and for Sulzberger Ice Shelf site on 10 May 2008 and 21 May 2008. Fast ice maps of the date closest to each date were used. The red solid lines indicate reference fast ice edges delineated based on the SAR images. Light blue area in the bottom figures are the fast ice region detected by random forest model.



### 4.5.3. Spatial distribution of fast ice

Three types of spatial distribution maps for fast ice cover changes during the entire study period were generated (Figure 4.7). Fast ice is mainly distributed along the coastline from the Land Ice Shelf to the Sulzberger Ice Shelf. The spatial distribution of fast ice is closely related to the distribution of bathymetry and grounded icebergs (Mahoney et al., 2007; Fraser et al., 2012). Figure 4.8 presents the corresponding bathymetry and SAR images showing the clusters of icebergs calved from the Land Ice Shelf. As seen in the SAR image, the Land Ice Shelf region is observed to be relatively shallow in depth. The groups of small icebergs are calved from the ice shelves play important anchor points in forming extensive fast ice (Massom et al., 2010; Fraser et al., 2012). The large number of assemblages of small grounded icebergs that are detached from the ice shelf can be grounded by relative shallow bathymetry. Therefore, the grounded icebergs would be the driving force that makes fast ice extensively formed in the Land Ice Shelf site and even extend far into the ocean. As the bathymetry over the Sulzberger Ice Shelf regions is relatively low, fast ice continuously exists. However, fast ice is not distributed meridionally because it may be due to the small number of elements that facilitate anchor points as there are relatively low calving events as identified in the SAR image (not shown).

Figure 4.7a exhibits the average coverage distribution of fast ice over the entire study period, by counting the number of times when fast ice is present during the entire study period. The higher the percentage, the more days fast ice appears on average. The map of fast ice spatial distribution for the number of switches between fast ice and non-fast ice is shown in Figure 4.7b. It was obtained by counting the switches between fast ice and non-fast ice throughout the study period. The higher values indicate a large variability between fast ice and non-fast ice, and vice versa. The areas with 80 % in Figure 4.7a mean that fast ice exists more than average, and correspond to the regions with small values of the number of switches as shown in Figure 4.7b. In Figure 4.7a, the lower percentage is seen as going to the edge, while the corresponding regions have lower switches in Figure 4.7b as the stability of offshore-ward fast ice decreases at the edge due to advection of pack ice and ocean waves, and the fluctuation in fast ice cover is larger rather than inland-ward fast ice (Dammann et al., 2016). Farther offshore, the switch values are low and similarly low in the duration of fast ice with less than 40 % in Figure 4.7a. In other words, the edge of fast ice has a high ratio of non-fast ice cover producing low switch values. Furthermore, fast ice areas between 60 and 80% of fast ice occurrence include both low and high switch values. As seen in the eastern part of the Land Ice Shelf area, regions with low switch values mean that even if the rate of fast ice occurrence during the entire study period is the same, it may be maintained for longer with fast ice or non-fast ice cover. Accordingly, Figure 4.7c shows the spatial distribution of the average fast ice duration by applying different weights depending to fast ice durations. In this map, the smaller the value, the less frequently the switch between fast ice and non-fast ice,

meaning that it lasts longer as fast ice region. In Figure 4.7c, fast ice zone of the Sulzberger Ice Shelf last longer than the Land Ice Shelf.

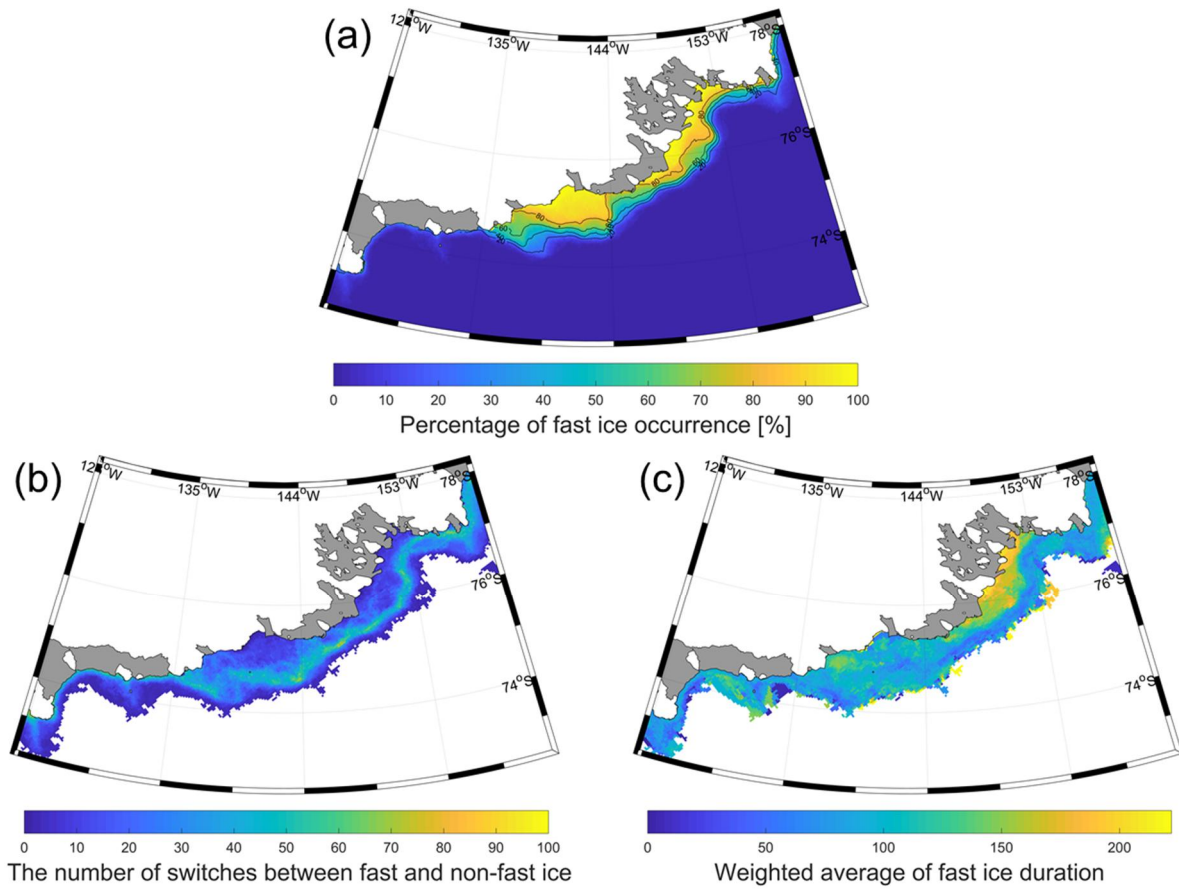


Figure 4. 7. Total frequency of fast ice residence for the period of from July 2002 to August 2011.

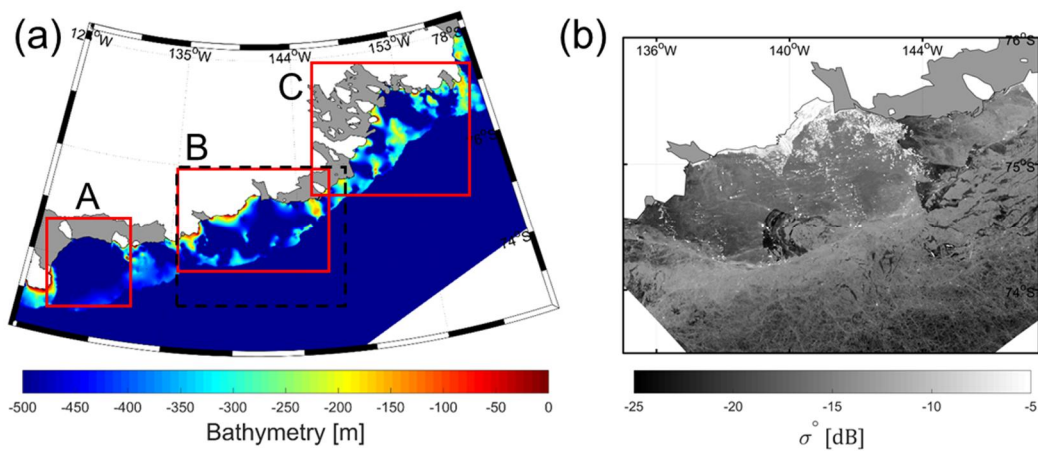


Figure 4. 8. Supplementary data (a) bathymetry from the IBCSO Version 1.0 and (b) ALOS PALSAR SAR image acquired on 05 August 2007 for the dashed box in (a).

#### 4.5.4. Fast ice time series and anomalous fast ice breakup events

The near decade-long mean annual cycle of fast ice is shown in Figure 4. 9 from July 2002 to September 2011. The fast ice minimum is in April-May. The West Antarctic fast ice shows a relatively later minimum compared to the East Antarctic fast ice, which usually has a minimum in the early mid-March (Fraser et al., 2012). Subsequently, fast ice rapidly grows at the beginning of June and the maximum appears in August-September. The maximal extent of fast ice usually lasts from mid-June to mid-September. Fast ice gradually decreases from mid-September. East Antarctica fast ice grows earlier, showing a maximal extent until October, followed by a rapid retreat. Therefore, the growth time for the West Antarctic fast ice to begin to grow is slower than that of the East Antarctica, and the time to maintain the maximal extent is shorter. In addition, fast ice breakup typically starts earlier than East Antarctic fast ice. This is because the dynamically formed fast ice is more distributed in West Antarctica than in East Antarctica, resulting in physically weaker fast ice causing episodic breakups (Fraser et al., 2012).

As shown in Figure 4. 10-11, time series fast ice extent exhibits apparently regional difference for fast ice trend and interannual variability. The Land Ice Shelf fast ice extent shows a not significant negative trend from 2002 to 2011. However, the trend should be further examined whether it is part of a much longer-term trend with additional decades of time series data. While the East Antarctica has a regular interannual variability for fast ice extent (Fraser et al., 2012), the West Antarctic fast ice in this study shows a large variability, especially for the Land Ice Shelf fast ice regions. Meanwhile, the Sulzberger Ice Shelf showed relatively strong negative trend for fast ice extent. This seems to be due to the variability which becomes stronger more rapidly after 2008 is largely attributable to the negative trend.

Anomalous breakup events are observed in the Land Ice Shelf fast ice both between 2004 and 2005 and in 2011. However, additional analysis is needed to determine whether this variability is due to macroscale volatility or due to large-scale atmospheric and oceanic effects or local sea ice dynamics that weaken the Antarctic sea ice. However, we confirmed that the anomalous fast ice collapse between 2004 and 2005 occurred in the Land Ice Shelf. It was reported that the Land Ice Shelf experienced relatively fast calving flux rather than basal melt (Rignot et al., 2011; Depporter et al., 2013). Therefore, as the ice shelf advances towards the far open ocean, it pushes fast ice further into the open water, making fast ice more unstable and eventually leading to breakups (Miles et al., 2017). As shown in MODIS images of Figure 4. 12, the Land Ice Shelf breakup starts on the western side of fast ice, and finally glacier calving and iceberg dispersal are seen with the entire fast ice collapses. Therefore, fast ice should be monitored over a long period of time as it can affect the stability of the ice shelf.

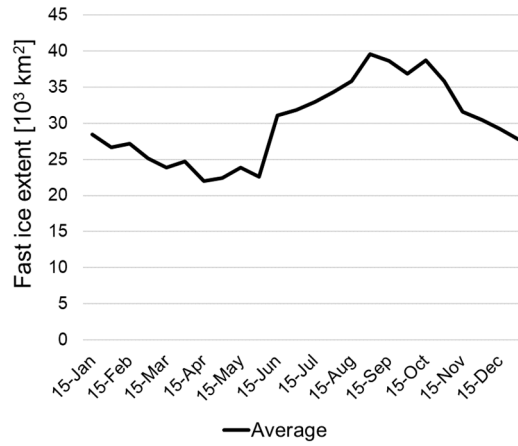


Figure 4. 9. Mean annual cycle of fast ice extent for the entire study area.

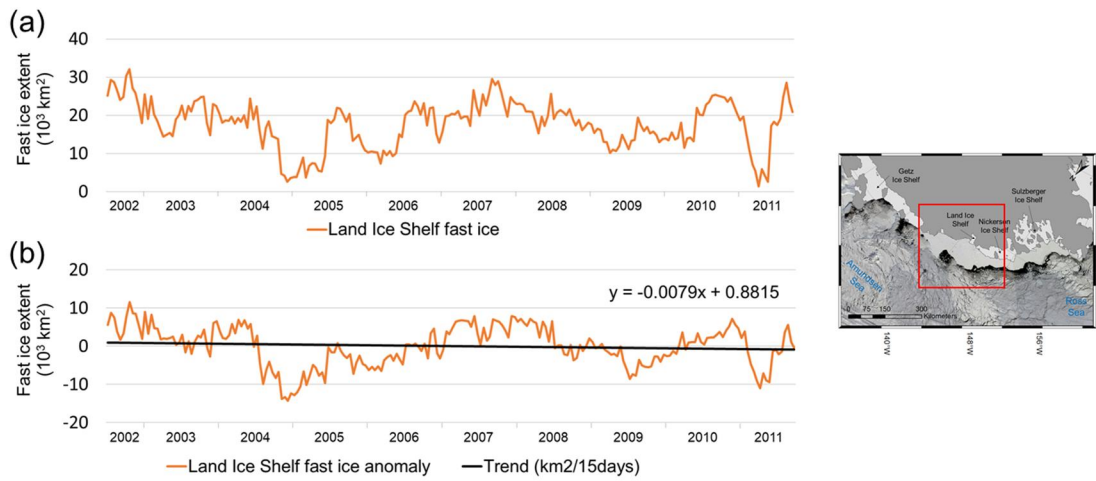


Figure 4. 10. Fast ice time series for the Land Ice Shelf site including (a) fast ice extent and (b) its anomaly with a linear trend as a solid line.

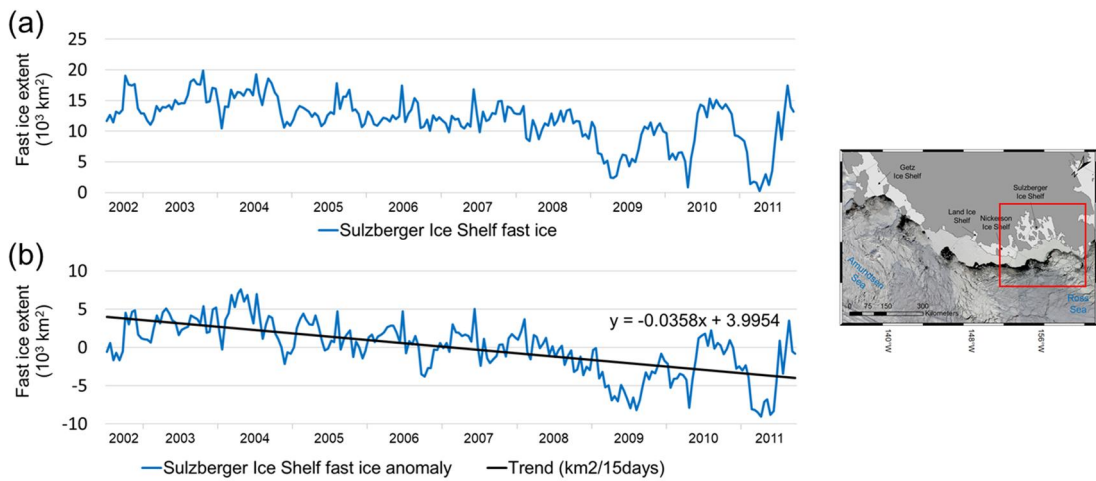


Figure 4. 11. Fast ice time series for the Sulzberger Ice Shelf site including (a) fast ice extent and (b) its anomaly with a linear trend as a solid line.

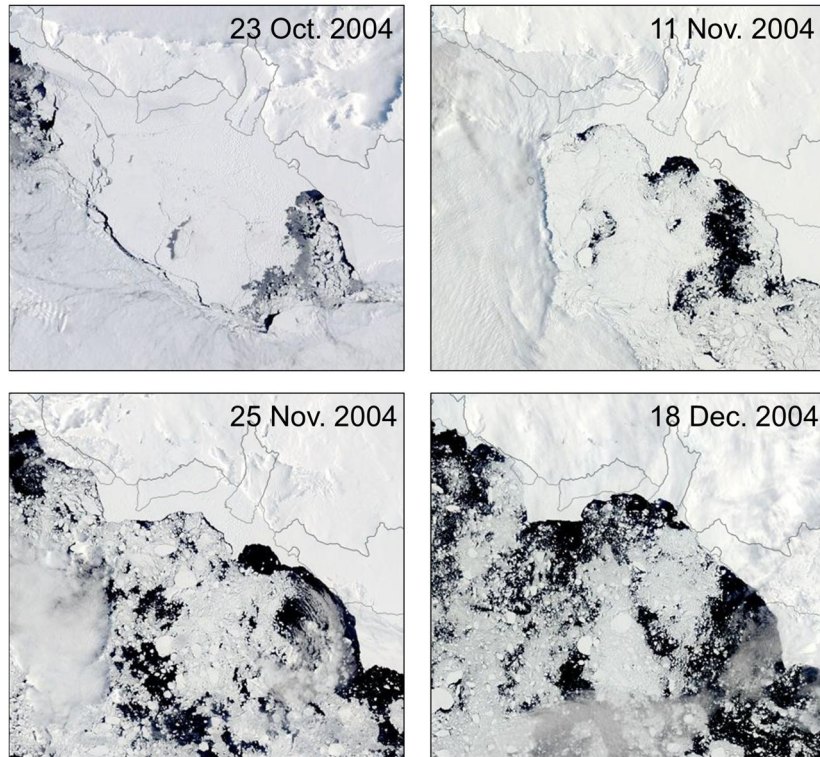


Figure 4. 12. MODIS images that show fast ice breakup event occurred in the Land Ice Shelf.



## 4.6. Conclusions and Future Work

We generated nearly decade-long fast ice in the Amundsen Sea of West Antarctica from July 2002 to September 2011. Spatiotemporal variability of fast ice extent was investigated particularly focusing on the Land and Sulzberger Ice shelf in the Amundsen Sea. Based on AMSR-E and MODIS IST data, machine learning and neighborhood correlation images methods were used to detect fast ice in 15-days intervals. Spatiotemporal patterns of fast ice have shown regional differences due to fast ice residency patterns, seasonality, and yearly trend. An apparent decline in fast ice extent was observed over near-decadal study period. Ice shelf with high calving flux has large effects on fast ice breakups. Fast ice breakup can trigger iceberg calving events as well. Therefore, fast ice variability can be used as prediction of calving events. Although it was a case study, the anomalous breakup of fast ice was observed. However, it is necessary to analyze various cases for a longer period to generalize the influence of the environment by region. This study is a detailed analysis of fast ice in the West Antarctic Ocean. However, it is needed to further analyze the factors influencing the formation of West Antarctic fast ice based on various differences between East Antarctic and West Antarctic such as fast-flowing ice shelves. Therefore, we can understand the complex characteristics of the distribution of the Antarctic fast ice by revealing the mechanism of West Antarctic fast ice differentiated from the East Antarctic fast ice. This suggests that the projection of fast ice distribution according to climate changes is very useful information for the surrounding environments such as the stability of ice shelf and polynya formation.



## Chapter 5

### Overall conclusions and Future research

It is expected that this dissertation provides Antarctic scientific community with an effective and reliable method to detect fast ice in a high spatiotemporal resolution and a comprehensive and detailed analysis of fast ice distribution and variability in a long period of time to extend our knowledge of fast ice over the West Antarctic in a global warming climate. Research part 1 was a research to map fast ice in the entire Antarctic by combining MODIS and AMSR-E data and machine learning techniques. The study achieved an automated fast ice classification compared to manual classification of fast ice in previous research. However, as some areas in West Antarctica show a high variation of fast ice for a short period of time, the composite period of 20-days is needed to be lowered to accurately analyze fast-changing fast ice. Due to the data void problem caused by cloud cover using optical sensor data and no reference data over the West Antarctic, it was also a problem for the West Antarctic fast ice. The research part 2 more focused on the West Antarctic fast ice. The research combined image segmentation, object correlation image method, and machine learning techniques by using pairs of SAR images with a short time gap. As SAR can penetrate clouds and detect fast ice, this study overcomes the cloud contamination problem that previous research has due to optical sensor. Since accurate fast ice regions that persist for a certain period of time are indistinguishable in a single SAR image, SAR composite images containing two dates of images in 5-days time intervals were used for image segmentation, which is well suited to SAR data with high spatial heterogeneity. Based on the segmented SAR composite images, object correlation image method was applied, which result in persisting fast ice regions with high correlation values. Fast ice classification with a short time interval was achieved, which is more appropriate for the analysis of fast-changing fast ice regions. However, SAR images have narrow swath width and spatial limitation with long repeat cycle, which make it difficult to analyze long-term fast ice changes. The final research part 3 used MODIS data selectively with AMSR-E data by overcoming cloud contamination problem. A detailed investigation of long-term fast ice extent in West Antarctica focusing on the Amundsen Sea was analyzed with the effects of atmospheric and oceanic forcing.

Several studies of fast ice remain for future work. Firstly, in this thesis, fast ice was obtained from 2002 to 2011. Since AMSR2 data are available, it is possible to apply fast ice detection algorithm in the following years to obtain longer-term fast ice. Decades of fast ice data will be used for long-term analysis with large-scale climate models and indices such as the Southern Annular Mode (SAM), the Southern Oscillation Index (SOI), the El Nino-Southern Oscillation (ENSO). The estimation of fast ice thickness and volume can be suggested as future work. As the volume of fast ice can comprise up to about 40% of total sea ice, it is needed to analyze the thickness of fast ice as fast ice extent changes. In addition, the greatest difference of East and West Antarctica is the change of ice shelf. It is needed to

analyze the fast ice of West Antarctica differentiated from East Antarctica such as an analysis for how fast-melting ice shelves in the West Antarctic Sea affect the formation of fast ice.

## References

1. Aoki, S. (2017). Breakup of land-fast sea ice in Lützow-Holm Bay, East Antarctica, and its teleconnection to tropical Pacific sea surface temperatures. *Geophysical Research Letters*, *44*(7), 3219-3227.
2. Barrett, B., Nitze, I., Green, S., & Cawkwell, F. (2014). Assessment of multi-temporal, multi-sensor radar and ancillary spatial data for grasslands monitoring in Ireland using machine learning approaches. *Remote sensing of Environment*, *152*, 109-124.
3. Barry, R., Moritz, R. E., & Rogers, J. (1979). The fast ice regimes of the Beaufort and Chukchi Sea coasts, Alaska. *Cold Regions Science and Technology*, *1*(2), 129-152.
4. Belgiu, M., & Drăguț, L. (2014). Comparing supervised and unsupervised multiresolution segmentation approaches for extracting buildings from very high resolution imagery. *ISPRS Journal of Photogrammetry and Remote Sensing*, *96*, 67-75.
5. Bintanja, R., Van Oldenborgh, G., Drijfhout, S., Wouters, B., & Katsman, C. (2013). Important role for ocean warming and increased ice-shelf melt in Antarctic sea-ice expansion. *Nature Geoscience*, *6*(5), 376-379.
6. Breiman, L. (2001). Decision tree forest. *Machine Learning*, *45*, 5-32.
7. Casey, J. A., Howell, S. E., Tivy, A., & Haas, C. (2016). Separability of sea ice types from wide swath C-and L-band synthetic aperture radar imagery acquired during the melt season. *Remote sensing of Environment*, *174*, 314-328.
8. Cavalieri, D., Crawford, J., Drinkwater, M., Eppler, D., Farmer, L., Jentz, R., & Wackerman, C. (1991). Aircraft active and passive microwave validation of sea ice concentration from the Defense Meteorological Satellite Program Special Sensor Microwave Imager. *Journal of Geophysical Research: Oceans*, *96*(C12), 21989-22008.
9. Cavalieri, D., & Parkinson, C. (2008). Antarctic sea ice variability and trends, 1979–2006. *Journal of Geophysical Research: Oceans*, *113*(C7).
10. Cavalieri, D., Parkinson, C., & Vinnikov, K. Y. (2003). 30-Year satellite record reveals contrasting Arctic and Antarctic decadal sea ice variability. *Geophysical Research Letters*, *30*(18).
11. Cavalieri, D. J., Gloersen, P., & Campbell, W. J. (1984). Determination of sea ice parameters with the Nimbus 7 SMMR. *Journal of Geophysical Research: Atmospheres*, *89*(D4), 5355-5369.
12. Chaney, N. W., Herman, J. D., Ek, M. B., & Wood, E. F. (2016). Deriving global parameter estimates for the Noah land surface model using FLUXNET and machine learning. *Journal of Geophysical Research: Atmospheres*, *121*(22).
13. Cavalieri, D. J., T. Markus, and J. C. Comiso. 2014. AMSR-E/Aqua Daily L3 12.5 km Brightness Temperature, Sea Ice Concentration, & Snow Depth Polar Grids, Version 3. [2003-2008]. Boulder, Colorado USA. NASA National Snow and Ice Data Center Distributed Active Archive Center. doi: [https://doi.org/10.5067/AMSR-E/AE\\_SI12.003](https://doi.org/10.5067/AMSR-E/AE_SI12.003). [07-10-2018].

14. Comiso, J. C., Cavalieri, D. J., & Markus, T. (2003). Sea ice concentration, ice temperature, and snow depth using AMSR-E data. *IEEE Transactions on Geoscience and Remote Sensing*, 41(2), 243-252.
15. Comiso, J. C., Cavalieri, D. J., Parkinson, C. L., & Gloersen, P. (1997). Passive microwave algorithms for sea ice concentration: A comparison of two techniques. *Remote sensing of Environment*, 60(3), 357-384.
16. Comiso, J. C., Gersten, R. A., Stock, L. V., Turner, J., Perez, G. J., & Cho, K. (2017). Positive trend in the Antarctic sea ice cover and associated changes in surface temperature. *Journal of Climate*, 30(6), 2251-2267.
17. Comiso, J. C., & Parkinson, C. L. (2008). Arctic sea ice parameters from AMSR-E data using two techniques and comparisons with sea ice from SSM/I. *Journal of Geophysical Research: Oceans*, 113(C2).
18. Comiso, J. C., & Steffen, K. (2001). Studies of Antarctic sea ice concentrations from satellite data and their applications. *Journal of Geophysical Research: Oceans*, 106(C12), 31361-31385.
19. Dammann, D. O., Eicken, H., Meyer, F. J., & Mahoney, A. R. (2016). Assessing small-scale deformation and stability of landfast sea ice on seasonal timescales through L-band SAR interferometry and inverse modeling. *Remote sensing of Environment*, 187, 492-504.
20. Depoorter, M. A., Bamber, J., Griggs, J., Lenaerts, J., Ligtenberg, S., Van den Broeke, M., & Moholdt, G. (2013). Calving fluxes and basal melt rates of Antarctic ice shelves. *Nature*, 502(7469), 89.
21. Dierking, W., & Busche, T. (2006). Sea ice monitoring by L-band SAR: An assessment based on literature and comparisons of JERS-1 and ERS-1 imagery. *IEEE Transactions on Geoscience and Remote Sensing*, 44(4), 957-970.
22. Fedotov, V., Cherepanov, N., & Tyshko, K. (1998). Some features of the growth, structure and metamorphism of East Antarctic landfast sea ice. *Antarctic sea ice: physical processes, interactions and variability*, 343-354.
23. Fraser, A. D. (2011). *East Antarctic landfast sea-ice distribution and variability*. University of Tasmania.
24. Fraser, A. D., Massom, R. A., & Michael, K. J. (2009). A method for compositing polar MODIS satellite images to remove cloud cover for landfast sea-ice detection. *IEEE Transactions on Geoscience and Remote Sensing*, 47(9), 3272-3282.
25. Fraser, A. D., Massom, R. A., & Michael, K. J. (2010). Generation of high-resolution East Antarctic landfast sea-ice maps from cloud-free MODIS satellite composite imagery. *Remote sensing of Environment*, 114(12), 2888-2896.
26. Fraser, A. D., Massom, R. A., Michael, K. J., Galton-Fenzi, B. K., & Lieser, J. L. (2012). East Antarctic landfast sea ice distribution and variability, 2000–08. *Journal of Climate*, 25(4), 1137-1156.
27. Fuiman, L., Davis, R., & Williams, T. (2002). Behavior of midwater fishes under the Antarctic ice: observations by a predator. *Marine Biology*, 140(4), 815-822.

28. Geurts, P., Ernst, D., & Wehenkel, L. (2006). Extremely randomized trees. *Machine Learning*, 63(1), 3-42.
29. Ghimire, B., Rogan, J., Galiano, V. R., Panday, P., & Neeti, N. (2012). An evaluation of bagging, boosting, and random forests for land-cover classification in Cape Cod, Massachusetts, USA. *GIScience & remote sensing*, 49(5), 623-643.
30. Giles, A., Massom, R., Heil, P., & Hyland, G. (2011). Semi-automated feature-tracking of East Antarctic sea ice from Envisat ASAR imagery. *Remote sensing of Environment*, 115(9), 2267-2276.
31. Giles, A. B., Massom, R. A., & Lytle, V. I. (2008). Fast-ice distribution in East Antarctica during 1997 and 1999 determined using RADARSAT data. *Journal of Geophysical Research: Oceans*, 113(C2).
32. Hall, D., Key, J., Casey, K., Riggs, G., & Cavalieri, D. (2004). Sea ice surface temperature product from MODIS, IEEE T. Geosci. Remote, 42, 1076–1087.
33. Hall, D., Salomonson, V., & Riggs, G. (2006). MODIS/Aqua Sea Ice Extent and IST Daily L3 Global 4km EASE-Grid Day. *Version*, 5, 2003-2008.
34. Hall, D. K., Riggs, G. A., Salomonson, V. V., Barton, J., Casey, K., Chien, J., . . . Tait, A. (2001). Algorithm theoretical basis document (ATBD) for the MODIS snow and sea ice-mapping algorithms. *Nasa Gsfc*, 45.
35. Heil, P. (2006). Atmospheric conditions and fast ice at Davis, East Antarctica: A case study. *Journal of Geophysical Research: Oceans*, 111(C5).
36. Heil, P., & Allison, I. (1999). The pattern and variability of Antarctic sea-ice drift in the Indian Ocean and western Pacific sectors. *Journal of Geophysical Research: Oceans*, 104(C7), 15789-15802.
37. Heil, P., Allison, I., & Lytle, V. I. (1996). Seasonal and interannual variations of the oceanic heat flux under a landfast Antarctic sea ice cover. *Journal of Geophysical Research: Oceans*, 101(C11), 25741-25752.
38. Heil, P., Gerland, S., & Granskog, M. (2011). An Antarctic monitoring initiative for fast ice and comparison with the Arctic. *The Cryosphere Discussions*, 5(5), 2437-2463.
39. Holland, P. R., & Kwok, R. (2012). Wind-driven trends in Antarctic sea-ice drift. *Nature Geoscience*, 5(12), 872.
40. Im, J., Jensen, J., & Tullis, J. (2008). Object-based change detection using correlation image analysis and image segmentation. *International Journal of Remote Sensing*, 29(2), 399-423.
41. Im, J., & Jensen, J. R. (2005). A change detection model based on neighborhood correlation image analysis and decision tree classification. *Remote sensing of Environment*, 99(3), 326-340.
42. Jang, E., Im, J., Park, G.-H., & Park, Y.-G. (2017). Estimation of Fugacity of Carbon Dioxide in the East Sea Using In Situ Measurements and Geostationary Ocean Color Imager Satellite Data. *Remote Sensing*, 9(8), 821.
43. Jensen, J. R. 2005. *Introductory Digital Image Processing: A Remote Sensing Perspective*. 3rd ed. Upper Saddle River, NJ: Prentice-Hall.

44. Karvonen, J. A. (2004). Baltic sea ice SAR segmentation and classification using modified pulse-coupled neural networks. *IEEE Transactions on Geoscience and Remote Sensing*, 42(7), 1566-1574.
45. Kern, S., Ozsoy-Çiçek, B., & Worby, A. P. (2016). Antarctic sea-ice thickness retrieval from ICESat: Inter-comparison of different approaches. *Remote Sensing*, 8(7), 538.
46. Kim, M., Im, J., Han, H., Kim, J., Lee, S., Shin, M., & Kim, H.-C. (2015). Landfast sea ice monitoring using multisensor fusion in the Antarctic. *GIScience & remote sensing*, 52(2), 239-256.
47. Kim, M., Im, J., Park, H., Park, S., Lee, M.-I., & Ahn, M.-H. (2017). Detection of Tropical Overshooting Cloud Tops Using Himawari-8 Imagery. *Remote Sensing*, 9(7), 685.
48. Kim, Y. H., Im, J., Ha, H. K., Choi, J.-K., & Ha, S. (2014). Machine learning approaches to coastal water quality monitoring using GOCI satellite data. *GIScience & remote sensing*, 51(2), 158-174.
49. Komarov, A. S., Landy, J. C., Komarov, S. A., & Barber, D. G. (2017). Evaluating Scattering Contributions to C-Band Radar Backscatter From Snow-Covered First-Year Sea Ice at the Winter-Spring Transition Through Measurement and Modeling. *IEEE Transactions on Geoscience and Remote Sensing*.
50. Kurtz, N., & Markus, T. (2012). Satellite observations of Antarctic sea ice thickness and volume. *Journal of Geophysical Research: Oceans*, 117(C8).
51. Kwok, R., Rignot, E., Holt, B., & Onstott, R. (1992). Identification of sea ice types in spaceborne synthetic aperture radar data. *Journal of Geophysical Research: Oceans*, 97(C2), 2391-2402.
52. Kwok, R., Schweiger, A., Rothrock, D., Pang, S., & Kottmeier, C. (1998). Sea ice motion from satellite passive microwave imagery assessed with ERS SAR and buoy motions. *Journal of Geophysical Research: Oceans*, 103(C4), 8191-8214.
53. Lang, W., Zhang, P., Wu, J., Shen, Y., & Yang, X. (2016). Incidence angle correction of SAR sea ice data based on locally linear mapping. *IEEE Transactions on Geoscience and Remote Sensing*, 54(6), 3188-3199.
54. Lawson, E., Smith, D., Sofge, D., Elmore, P., & Petry, F. (2017). Decision forests for machine learning classification of large, noisy seafloor feature sets. *Computers & Geosciences*, 99, 116-124.
55. Lei, R., Li, Z., Cheng, B., Zhang, Z., & Heil, P. (2010). Annual cycle of landfast sea ice in Prydz Bay, east Antarctica. *Journal of Geophysical Research: Oceans*, 115(C2).
56. Li, M., Im, J., & Beier, C. (2013). Machine learning approaches for forest classification and change analysis using multi-temporal Landsat TM images over Huntington Wildlife Forest. *GIScience & remote sensing*, 50(4), 361-384.
57. Liaw, A., & Wiener, M. (2002). Classification and regression by randomForest. *R news*, 2(3), 18-22.
58. Liu, H., Guo, H., & Zhang, L. (2015). SVM-based sea ice classification using textural features and concentration from RADARSAT-2 Dual-Pol ScanSAR data. *IEEE Journal of Selected Topics in Applied Earth Observations and Remote Sensing*, 8(4), 1601-1613.



59. Long, J. A., Lawrence, R. L., Greenwood, M. C., Marshall, L., & Miller, P. R. (2013). Object-oriented crop classification using multitemporal ETM+ SLC-off imagery and random forest. *GIScience & remote sensing*, 50(4), 418-436.
60. Lucieer, V., & Lamarche, G. (2011). Unsupervised fuzzy classification and object-based image analysis of multibeam data to map deep water substrates, Cook Strait, New Zealand. *Continental Shelf Research*, 31(11), 1236-1247.
61. Normile, D. (2015). Antarctic researchers ponder challenges posed by increasing sea ice, <http://www.sciencemag.org/news/2015/05/antarctic-researchers-ponder-challenges-posed-increasing-sea-ice>.
62. Mahoney, A., Eicken, H., Gaylord, A. G., & Shapiro, L. (2007). Alaska landfast sea ice: Links with bathymetry and atmospheric circulation. *Journal of Geophysical Research: Oceans*, 112(C2).
63. Mahoney, A., Eicken, H., Graves, A., Shapiro, L., & Cotter, P. (2004). *Landfast sea ice extent and variability in the Alaskan Arctic derived from SAR imagery*. Paper presented at the Geoscience and Remote Sensing Symposium, 2004. IGARSS'04. Proceedings. 2004 IEEE International.
64. Mahoney, A., Eicken, H., & Shapiro, L. (2007). How fast is landfast sea ice? A study of the attachment and detachment of nearshore ice at Barrow, Alaska. *Cold Regions Science and Technology*, 47(3), 233-255.
65. Mahoney, A., Eicken, H., Shapiro, L., & Graves, A. (2006). *Defining and locating the seaward landfast ice edge in northern Alaska*. Paper presented at the 18th International Conference on Port and Ocean Engineering under Arctic Conditions (POAC'05), Potsdam, NY.
66. Markus, T., & Cavalieri, D. J. (2000). An enhancement of the NASA Team sea ice algorithm. *IEEE Transactions on Geoscience and Remote Sensing*, 38(3), 1387-1398.
67. Marsland, S., & Wolff, J. O. (2001). On the sensitivity of Southern Ocean sea ice to the surface freshwater flux: a model study. *Journal of Geophysical Research: Oceans*, 106(C2), 2723-2741.
68. Maslanik, J. (1992). Effects of weather on the retrieval of sea ice concentration and ice type from passive microwave data. *International Journal of Remote Sensing*, 13(1), 37-54.
69. Maslanik, J., & Key, J. (1993). Comparison and integration of ice-pack temperatures derived from AVHRR and passive microwave imagery. *Annals of Glaciology*, 17, 372-378.
70. Massom, R., Hill, K., Lytle, V., Worby, A., Paget, M., & Allison, I. (2001). Effects of regional fast-ice and iceberg distributions on the behaviour of the Mertz Glacier polynya, East Antarctica. *Annals of Glaciology*, 33(1), 391-398.
71. Massom, R. A., Giles, A. B., Fricker, H. A., Warner, R. C., Legrésy, B., Hyland, G., . . . Fraser, A. D. (2010). Examining the interaction between multi-year landfast sea ice and the Mertz Glacier Tongue, East Antarctica: Another factor in ice sheet stability? *Journal of Geophysical Research: Oceans*, 115(C12).
72. Massom, R. A., Hill, K., Barbraud, C., Adams, N., Ancel, A., Emmerson, L., & Pook, M. J. (2009). Fast ice distribution in Adélie Land, East Antarctica: interannual variability and implications for emperor penguins *Aptenodytes forsteri*. *Marine Ecology Progress Series*, 374, 243-257.
73. Maxwell, A., Strager, M., Warner, T., Zegre, N., & Yuill, C. (2014). Comparison of NAIP

- orthophotography and RapidEye satellite imagery for mapping of mining and mine reclamation. *GIScience & remote sensing*, 51(3), 301-320.
74. Mazur, A., Wåhlin, A., & Krężel, A. (2017). An object-based SAR image iceberg detection algorithm applied to the Amundsen Sea. *Remote sensing of Environment*, 189, 67-83.
  75. Meyer, F. J., Mahoney, A. R., Eicken, H., Denny, C. L., Druckenmiller, H. C., & Hendricks, S. (2011). Mapping arctic landfast ice extent using L-band synthetic aperture radar interferometry. *Remote sensing of Environment*, 115(12), 3029-3043.
  76. Miles, B. W., Stokes, C. R., & Jamieson, S. S. (2017). Simultaneous disintegration of outlet glaciers in Porpoise Bay (Wilkes Land), East Antarctica, driven by sea ice break-up. *The Cryosphere*, 11, 427-442.
  77. Murphy, E. J., Clarke, A., Symon, C., & Priddle, J. (1995). Temporal variation in Antarctic sea-ice: analysis of a long term fast-ice record from the South Orkney Islands. *Deep Sea Research Part I: Oceanographic Research Papers*, 42(7), 1045-1062.
  78. Nihashi, S., & Ohshima, K. I. (2015). Circumpolar mapping of Antarctic coastal polynyas and landfast sea ice: relationship and variability. *Journal of Climate*, 28(9), 3650-3670.
  79. Nyarko, B. K., Diekkrüger, B., Van De Giesen, N. C., & Vlek, P. L. (2015). Floodplain wetland mapping in the White Volta River Basin of Ghana. *GIScience & remote sensing*, 52(3), 374-395.
  80. Ohshima, K. I., Fukamachi, Y., Williams, G. D., Nihashi, S., Roquet, F., Kitade, Y., . . . Field, I. (2013). Antarctic Bottom Water production by intense sea-ice formation in the Cape Darnley polynya. *Nature Geoscience*, 6(3), 235.
  81. Parkinson, C., & Cavalieri, D. (2012). Antarctic sea ice variability and trends, 1979-2010. *The Cryosphere*, 6(4), 871.
  82. Parkinson, C. L., & DiGirolamo, N. E. (2016). New visualizations highlight new information on the contrasting Arctic and Antarctic sea-ice trends since the late 1970s. *Remote sensing of Environment*, 183, 198-204.
  83. Price, D., Rack, W., Haas, C., Langhorne, P. J., & Marsh, O. (2013). Sea ice freeboard in McMurdo Sound, Antarctica, derived by surface-validated ICESat laser altimeter data. *Journal of Geophysical Research: Oceans*, 118(7), 3634-3650.
  84. Pritchard, H., Ligtenberg, S., Fricker, H., Vaughan, D., Van den Broeke, M., & Padman, L. (2012). Antarctic ice-sheet loss driven by basal melting of ice shelves. *Nature*, 484(7395), 502.
  85. Quinlan, R. 2013. "See5.0: An Informal Tutorial." Accessed May 26, 2014. <http://www.rulequest.com>
  86. Ressel, R., Frost, A., & Lehner, S. (2015). A neural network-based classification for sea ice types on X-band SAR images. *IEEE Journal of Selected Topics in Applied Earth Observations and Remote Sensing*, 8(7), 3672-3680.
  87. Rhee, J., & Im, J. (2017). Meteorological drought forecasting for ungauged areas based on machine learning: Using long-range climate forecast and remote sensing data. *Agricultural and Forest Meteorology*, 237, 105-122.

88. Rhee, J., Park, S., & Lu, Z. (2014). Relationship between land cover patterns and surface temperature in urban areas. *GIScience & remote sensing*, 51(5), 521-536.
89. Rignot, E., Velicogna, I., van den Broeke, M. R., Monaghan, A., & Lenaerts, J. T. (2011). Acceleration of the contribution of the Greenland and Antarctic ice sheets to sea level rise. *Geophysical Research Letters*, 38(5).
90. Scott, R. C., Lubin, D., Vogelmann, A. M., & Kato, S. (2017). West Antarctic Ice Sheet cloud cover and surface radiation budget from NASA A-train satellites. *Journal of Climate*, 30(16), 6151-6170.
91. Shokr, M., & Sinha, N. (2015). *Sea ice: physics and remote sensing*: John Wiley & Sons.
92. Simmonds, I. (2015). Comparing and contrasting the behaviour of Arctic and Antarctic sea ice over the 35 year period 1979–2013. *Annals of Glaciology*, 56(69), 18-28.
93. Spinhirne, J. D., Palm, S. P., Hart, W. D., Hlavka, D. L., & Welton, E. J. (2005). Cloud and aerosol measurements from GLAS: Overview and initial results. *Geophysical Research Letters*, 32(22).
94. Spreen, G., Kaleschke, L., & Heygster, G. (2008). Sea ice remote sensing using AMSR-E 89-GHz channels. *Journal of Geophysical Research: Oceans*, 113(C2).
95. Stuecker, M. F., Bitz, C. M., & Armour, K. C. (2017). Conditions leading to the unprecedented low Antarctic sea ice extent during the 2016 austral spring season. *Geophysical Research Letters*, 44(17), 9008-9019.
96. Suen, J. Y., Fang, M. T., & Lubin, P. M. (2014). Global distribution of water vapor and cloud cover—sites for high-performance THz applications. *IEEE Transactions on Terahertz Science and Technology*, 4(1), 86-100.
97. Tamura, T., Ohshima, K. I., Markus, T., Cavalieri, D. J., Nihashi, S., & Hirasawa, N. (2007). Estimation of thin ice thickness and detection of fast ice from SSM/I data in the Antarctic Ocean. *Journal of Atmospheric and Oceanic Technology*, 24(10), 1757-1772.
98. Tamura, T., Ohshima, K. I., & Nihashi, S. (2008). Mapping of sea ice production for Antarctic coastal polynyas. *Geophysical Research Letters*, 35(7).
99. Tang, S., Qin, D., Ren, J., Kang, J., & Li, Z. (2007). Structure, salinity and isotopic composition of multi-year landfast sea ice in Nella Fjord, Antarctica. *Cold Regions Science and Technology*, 49(2), 170-177.
100. Tschudi, M., C. Fowler, J. Maslanik, J. S. Stewart, and W. Meier. 2016. Polar Pathfinder Daily 25 km EASE-Grid Sea Ice Motion Vectors, Version 3. [2003-2008]. Boulder, Colorado USA. NASA National Snow and Ice Data Center Distributed Active Archive Center. doi: <https://doi.org/10.5067/O57VAIT2AYYY>. [07-10-2018].
101. Turner, J., Phillips, T., Marshall, G. J., Hosking, J. S., Pope, J. O., Bracegirdle, T. J., & Deb, P. (2017). Unprecedented springtime retreat of Antarctic sea ice in 2016. *Geophysical Research Letters*, 44(13), 6868-6875.
102. Ushio, S. (2006). Factors affecting fast-ice break-up frequency in Lützow-Holm Bay, Antarctica. *Annals of Glaciology*, 44(1), 177-182.
103. Vinas, M. (2017). Sea Ice Extent Sinks to Record Lows at Both Poles,

<https://www.nasa.gov/feature/goddard/2017/sea-ice-extent-sinks-to-record-lows-at-both-poles>.

104. Wakabayashi, H., Matsuoka, T., Nakamura, K., & Nishio, F. (2004). Polarimetric characteristics of sea ice in the Sea of Okhotsk observed by airborne L-band SAR. *IEEE Transactions on Geoscience and Remote Sensing*, 42(11), 2412-2425.
105. Wang, L., Scott, K. A., Xu, L., & Clausi, D. A. (2016). Sea ice concentration estimation during melt from dual-pol SAR scenes using deep convolutional neural networks: A case study. *IEEE Transactions on Geoscience and Remote Sensing*, 54(8), 4524-4533.
106. Wesche, C., & Dierking, W. (2012). Iceberg signatures and detection in SAR images in two test regions of the Weddell Sea, Antarctica. *Journal of Glaciology*, 58(208), 325-339.
107. Wesche, C., & Dierking, W. (2015). Near-coastal circum-Antarctic iceberg size distributions determined from Synthetic Aperture Radar images. *Remote sensing of Environment*, 156, 561-569.
108. Williams, R., Rees, W., & Young, N. (1999). A technique for the identification and analysis of icebergs in synthetic aperture radar images of Antarctica. *International Journal of Remote Sensing*, 20(15-16), 3183-3199.
109. Witharana, C., & Civco, D. L. (2014). Optimizing multi-resolution segmentation scale using empirical methods: Exploring the sensitivity of the supervised discrepancy measure Euclidean distance 2 (ED2). *ISPRS Journal of Photogrammetry and Remote Sensing*, 87, 108-121.
110. WMO, 2014. World Meteorological Organization Sea Ice Nomenclature, Volume 1 terminology. WMO Report No. 259 ([http://www.aari.ru/gdsidb/xml/wmo\\_259.php](http://www.aari.ru/gdsidb/xml/wmo_259.php)).
111. Worby, A. P., Geiger, C. A., Paget, M. J., Van Woert, M. L., Ackley, S. F., & DeLiberty, T. L. (2008). Thickness distribution of Antarctic sea ice. *Journal of Geophysical Research: Oceans*, 113(C5).
112. Xie, H., Tekeli, A. E., Ackley, S. F., Yi, D., & Zwally, H. J. (2013). Sea ice thickness estimations from ICESat Altimetry over the Bellingshausen and Amundsen Seas, 2003–2009. *Journal of Geophysical Research: Oceans*, 118(5), 2438-2453.
113. Yan, G., Mas, J. F., Maathuis, B., Xiangmin, Z., & Van Dijk, P. (2006). Comparison of pixel-based and object-oriented image classification approaches—a case study in a coal fire area, Wuda, Inner Mongolia, China. *International Journal of Remote Sensing*, 27(18), 4039-4055.
114. Yang, Y., Zhijun, L., Leppäranta, M., Cheng, B., Shi, L., & Lei, R. (2016). Modelling the thickness of landfast sea ice in Prydz Bay, East Antarctica. *Antarctic Science*, 28(1), 59-70.
115. Yuan, X. (2004). ENSO-related impacts on Antarctic sea ice: a synthesis of phenomenon and mechanisms. *Antarctic Science*, 16(4), 415-425.
116. Zakhvatkina, N., Korosov, A., Muckenhuber, S., Sandven, S., & Babiker, M. (2017). Operational algorithm for ice–water classification on dual-polarized RADARSAT-2 images. *The Cryosphere*, 11(1), 33-46.
117. Zakhvatkina, N. Y., Alexandrov, V. Y., Johannessen, O. M., Sandven, S., & Frolov, I. Y. (2013). Classification of sea ice types in ENVISAT synthetic aperture radar images. *IEEE Transactions on Geoscience and Remote Sensing*, 51(5), 2587-2600.
118. Zwally, H. J., Comiso, J. C., Parkinson, C. L., Campbell, W. J., & Carsey, F. D. (1983). *Antarctic*

*sea ice, 1973-1976: Satellite passive-microwave observations*. Retrieved from

119. Zwally, H. J., Comiso, J. C., Parkinson, C. L., Cavalieri, D. J., & Gloersen, P. (2002). Variability of Antarctic sea ice 1979–1998. *Journal of Geophysical Research: Oceans*, 107(C5).
120. 한향선, 김연춘, 진효림, & 이훈열. (2015). InSAR 긴밀도 영상을 이용한 남극 장보고기지 인근 정착해빙의 연간 변화 분석. *Korean Journal of Remote Sensing*, 31(6), 501-512.

## Acknowledgements

먼저 제 롤모델이자 지도 교수님이신 임정호 교수님께 가장 큰 감사를 드립니다. 제 박사 과정 전반에 걸쳐 교수님의 지지와 격려가 없었다면 박사를 이렇게 성공적으로 마칠 수 없었을 것입니다. 항상 긍정적인 마인드로 말씀해주시고 늘 연구와 연구 외적인 부분도 놓치지 않으시는 교수님을 보며 따로 말씀해주시지 않아도 자연적으로 동기부여가 되고 배움이 되는 것 같습니다. 연구적인 면에서 올바른 연구자의 자세를 보여주시고 새로운 길을 개척하시는 모습을 보면서 졸업하고 독립적인 박사로서 홀로서기 할 때 어떤 자세를 가지고 가야할 지 느끼고 항상 발전하는 연구자가 되어야 되겠다는 생각을 합니다. 정말 감사합니다.

그리고 저의 박사 디펜스 커미티로 수락해주신 이명인 교수님, 조정화 교수님, 그리고 극지연구소에 김현철 박사님과 한향선 박사님께 진심으로 감사드립니다. 교수님들과 박사님들의 실질적인 많은 조언들과 제안들이 연구 뿐만 아니라 연구자가 갖추어야 할 여러가지 면에 대해서 많은 도움이 되었습니다.

현 남자친구이자 든든한 동료인 이상균에게 두번째로 큰 감사를 드립니다. 힘든 대학원 생활에서 연구적인 면으로나 생활적인 면에서 힘들 때마다 버팀목이 되 줘서 큰 힘이 되었습니다.

우리 연구실에 (들어온 순서대로..) 선영이, 은나, 정희, 민소, 수민언니, 성문이, 철희, 서희, 주현이, 대현이, 영준이, 동진이, 유진이, 보경이, 연수에게도 너무 고맙다는 말을 해주고 싶습니다. 열심히 하는 친구들에게 오히려 제가 더 많이 배우기도 했고 또 밝고 사랑 가득해서 편하고 재미있는 연구실 생활을 할 수 있었습니다. 그리고 박박사님(박혜미 박사님)께도 정말 감사드립니다. 언니같이 항상 좋은 말씀해주시고 2시쯤 마시는 즐거운 커피 타임이 너무 행복했습니다. 연구실 좋은 사람들을 만나서 행운인 것 같습니다.

그리고 특별히 박사과정 마지막에 어쩌다 우리 연구실과 인연이 닿은 정혜(교수님)는 친구지만 참 귀감이 되는 친구고 먼저 대학원 생활을 했고 그리고 사회생활을 시작하면서 많은 조언과 힘이 되어줘서 특별히 고맙습니다.

다른 모든 내 친구들에게 다들 멀리 떨어져 있지만 카톡방은 마치 옆에 있는 듯 늘 시끄럽고 새로운 안부와 즐거운 이야기는 힘든 대학원 생활에 큰 즐거움 중 하나였습니다. 모두 고맙고 항상 보고 싶습니다.

그리고 마지막으로 우리 가족 아빠, 엄마, 혜진이, 학민이에게 아주 깊은 감사를 표합니다. 학교가 울산이었기에 가까운 곳에서 많은 도움을 받았고 가족은 자체로 말이 필요 없는 저의 큰 힘이었습니다. 감사합니다.